AN ABSTRACT OF THE THESIS OF

CLIVE EDGAR DORMAN (Name) for the DOCTOR OF PHILOSOPHY (Degree)

in OCEANOGRAPHY (Major) presented on January 11, 1974 (Date)

Title: ANALYSIS OF METEOROLOGICAL AND OCEANOGRAPHIC DATA FROM OCEAN STATION VESSEL N (30N 140W)

Abstract approved: Redacted for Privacy

Clayton A. Paulson

The thesis examines the principal air-sea properties at Ocean Station Vessel N (30N 140W). In a descriptive section, meteorological and oceanographic data for N are analyzed over 20 years (1951-1970) and 7 years (1964-1970), respectively. A rainfall estimate is constructed for the 20 year period. The yearly average rainfall is 22 centimeters, far less than current estimates. Daily and seasonal variations are presented. Heat budgets of the surface show that the two decades are distinctly different. Anomalies of the 20 years of all meteorological variables are calculated. The pressure anomaly appears to be loosely correlated with anomalous large scale events in the equatorial dry zone. Time series cross-sections are shown of the mixed layer depth, bottle temperature and salinity. The near surface density appears to be largely controlled by temperature.

Surface wind speed, air pressure, sea temperature, air temperature and dew point spectra for a 10-year period (1961-1970) are shown in a spectral section. Spectra are computed separately for the 4 seasons. Rotary spectra for the wind are also calculated.

In a discussion of mixed layer dynamics, theoretical calculations indicate that salinity is not a significant factor in the Eastern subtropics.

In a final section, Denman's mixed layer model is applied to two cases of data from N. It is found that Denman's model describes the local mixed layer changes in the one case where advective effects could be resolved. It is suggested that mixed layer extinction lengths for sunlight are shorter than previously believed--about 5 meters. Denman's mixed layer model appears applicable to local changes in the Eastern subtropics.

Analysis of Meteorological and Oceanographic Data from Ocean Station Vessel N (30N 140W)

by

Clive Edgar Dorman

A THESIS

submitted to

Oregon State University

in partial fulfillment of
the requirements for the
degree of

Doctor of Philosophy

June 1974

APPROVED:

Redacted for Privacy

Assistant Professor of Oceanography

in charge of major

Redacted for Privacy

Dean of School of Oceanography

Redacted for Privacy

Dean of Graduate School

Date thesis is presented January 11, 1974

Typed by Clover Redfern for Clive Edgar Dorman

ACKNOWLEDGMENT

I am most grateful to Dr. Clayton A. Paulson, my major Professor, for his guidance and support in carrying out my thesis work. Without his time and interest, I would not have been able to complete the endeavor.

Dr. William Quinn was very helpful in starting out the grant under which I was supported. I valued his suggestions as well. I appreciated, too, discussions with Dr. William Elliott.

The oceanographic data used herein came from the National Oceanographic Data Center. The meteorological data came from the National Climatic Center. This work was supported by the Atmospheric Sciences Section of the National Science Foundation under Grants GA-1571 and GA-27205. In addition, my studies were further made possible by financial support from the Veterans Administrations Educational Assistance.

TABLE OF CONTENTS

LIST OF TABLES

LIST OF FIGURES

ANALYSIS OF METEOROLOGICAL AND OCEANOGRAPHIC DATA FROM OCEAN STATION VESSEL N (30N 140W)

1. INTRODUCTION

It has been generally accepted that air-sea interactions have extensive effects on the earth's atmosphere and ocean. The most cited example of the importance of air-sea interaction and the large scale effects of the ocean on the atmosphere and the applied problem of weather forecasting. Papers such as Bryan (1969), Manabe (1969) and Namias (1963, 1969) point out some of the influences of the ocean on the atmosphere on large scales.

Many details of the air-sea relationships remain incomplete. It is the purpose of this thesis to examine some of the characteristics of the atmosphere and the upper ocean at Ocean Station Vessel N in the subtropical northeastern Pacific (30N 140W). In this way, the thesis will contribute further information about air-sea relationships that are not as yet defined. But first, a few details will be discussed to put this study in perspective.

1.1 Time Scales

Ideas on air-sea relationships can best be regarded in light of approximate time scales. There are several such scales. The first, the microscale, is from about one second to a few minutes.

Significant variations occur during this time scale in fluxes of heat, moisture, and momentum. It is also the time scale of wave motions in the sea. This scale is typical of turbulence.

The mesoscale extends from a few minutes to a few hours. Within this scale, significant variations occur in the smaller features of weather such as cumulus development, thundershowers, and radiative fluxes.

Events that occur from a few hours to a week are on the synoptic scale. On the synoptic scale, there are significant variations in the curl of the wind stress. This scale includes typical weather features such as storms, fronts and high pressure areas.

The final scale, the seasonal scale, is greater than a week in length. This scale is reflected in most atmospheric and oceanic variables.

1.2 Radiative Fluxes

On all scales, the principal exchange mechanisms near the sea surface are radiative and turbulent. The largest radiative flux into the sea is via shorter wave lengths from the sun ranging between .35 and 3 microns. As well as being selectively filtered by the atmosphere, a large portion of the solar radiation arrives at the surface by indirect paths which include scattering by the air and reflection off clouds. Variations of solar radiation are primarily due to season,

latitude, air mass, cloud cover, and suspended matter in the air. Solar radiation itself is not usually measured, so it must be calculated by empirical formulas, some of which are reviewed by Kraus (1972). Most of these empirical formulas use the solar radiation outside the atmosphere per horizontal area per day, which is reduced by the air mass of the atmosphere through which it travels, and corrected by the amount of cloud cover. Minimum time averages of the order of a month are necessary to obtain a statistically stable estimate of the solar radiation at the earth's surface by empirical formulas. Still, the results of the various empirical formulas can be quite different.

Although some solar radiation is reflected from the surface of the sea, and less is scattered upward out of the sea, most passes downward. This light is absorbed roughly in an exponential manner according to Beer's Law: $e^{-\gamma z}$ where γ is the total extinction coefficient and z is depth. This relationship is rather good if there is a deep, well mixed layer at the surface.

The other major form of radiation across the air-sea interface is back radiation. Actually, it is the infrared radiation associated with wavelengths from about 3 to 40 microns. Nearly all infrared radiation from the sea comes from the top millimeter and is within a few percent of σT_s^4, where σ is the Stephen-Boltzman constant and T_s is the temperature of the thin surface layer. The lower atmosphere radiates and absorbs long wave energy less effectively

than the sea. However, the lowest 20 meters of the moist maritime air will absorb and radiate most of the long wave radiation within a few percent of σT_a^4 (T_a is some average temperature of the lowest 20 meters of air) except for the 8 to 13 microns region which the atmosphere is transparent. The sea surface and the lower atmosphere radiate to each other and the net loss of the system is that which escapes beyond the lowest air layer. However, clouds radiate infrared radiation downward proportional to σT_c^4 (if the cloud is opaque) and so reduce the net loss of the air-sea interface system. There is also a small amount of downward infrared radiation from the atmosphere above 20 meters. The net loss of infrared radiation from the sea surface/lower atmosphere is the back radiation and is usually calculated from various empirical formulas. Some of these formulas are reviewed in Kraus (1972). Empirical back radiation formulas usually depend upon σT_a^4 and are reduced by the total cloud cover. The forms of different back radiation formulas are remarkably different and some are of questionable theoretical basis.

1.3 Turbulent Fluxes

In addition to the radiative fluxes, there are significant turbulent fluxes near the air-sea interface. These include momentum, latent heat,and sensible heat. Turbulent fluxes can be measured in four ways: eddy-correlation, profile, dissipation,and bulk aerodynamic

methods. These methods are discussed by Deacon and Webb (1962) and Deacon (1959).

The eddy-correlation method relates the flux of a quantity to the covariance of the same quantity and the vertical velocity. The eddy-correlation flux is given by

$$F_s = \overline{(\rho' w')s'} \sim \rho \overline{w's'}$$

where s' is a fluctuating quantity, w' is the vertical velocity, ρ is the density of air, and F_s is the flux of the quantity in units of s per unit area per unit time. The prime represents the instantaneous fluctuation of a quantity. Time scales of fluxes range from minutes to fractions of a second. Practical measurements by the eddy-correlation technique require sensitive and delicate instruments under supervision of specialists. Due to the difficulty in making eddy-correlation measurements, this type of measurement is usually limited to one site for a few hours or days.

Another technique of determining the flux is the profile method. This method is based upon the vertical gradient. The flux is given by

$$F_s = \rho k_s \frac{\partial \bar{s}}{\partial z}$$

$\partial \bar{s}/\partial z$, is an average vertical gradient, and k_s is an eddy transfer coefficient that must be determined by some empirical means.

Measurements by the profile technique require at least two measurements in the vertical and in practice usually several are taken. Relatively sensitive measurements over the sea are required since vertical gradients there are weak. The empirical eddy-transfer coefficient can be based upon complicated stability formulas requiring accurate measurements of at least the vertical temperature gradient, wind speed, and humidity. The profile method also requires careful measurement by sensitive and complicated instruments operated by specialists. Like the eddy-correlation measurements, the vertical profile type measurements are usually limited to one site for a few hours or days.

A newer method of measuring the surface momentum flux is the dissipation technique suggested by Deacon (1959). This technique is based in one of its forms upon the balance between the mechanical production of turbulent energy and dissipation in the atmospheric boundary layer. That is,

$$-\overline{u'w'}\,\frac{\partial \bar{u}}{\partial z} = \epsilon$$

where ϵ is the viscous dissipation and all other energy sources and sinks are considered negligible.

The concept of local isotropy as suggested by Kolmogroff is used. Local isotropy is postulated to occur in a region of the wind

velocity and scalar spectra at higher frequencies where there are no energy sources or sinks, only energy transfer from lower to higher wave numbers. Using these concepts, the downwind spectra are given by:

$$\Phi_{uu}(K) = A\epsilon^{2/3}K^{-5/3}$$

where $K = \frac{2\pi f}{\overline{u}}$, f is frequency and A is a constant. If we assume a log wind profile, then

$$\epsilon = u_*^3/kz$$

where $u_* = (\overline{u'w'})^{1/2}$ is the friction velocity and k is von Karman s constant. As a result, the surface stress $\tau = (-\rho\overline{u'w'})$ is given by

$$\tau = \rho A(2\pi K)^{2/3}(\frac{z}{\overline{u}})^{2/3}\Phi_{uu}(f)f^{5/3}$$

The dissipation technique requires accurate measurement of the wind spectrum for periods from minutes to fractions of a second. As with the eddy-correlation technique and the profile method, practical measurements of the flux by the dissipation technique are performed by elaborate instrumentation and are usually limited to one site for a few hours or days.

There is one final method of measuring the surface fluxes.

This is the bulk aerodynamic method which is really a specialized case of the vertical gradient method. The bulk aerodynamic flux formula is

$$F = \rho c_s (s_s - s_a) u_a$$

where u_a is the wind speed, subscript s refers to the value of the quantity at the sea surface, the subscript a refers to the value at a convenient height (usually 10 meters). In this case, c_s is an empirical dimensionless constant. The drag coefficient is actually a significant function of the air stability and possibly a slight function of wind speed. The usual method in calculating the flux is to assume neutral stability and then the fluxes are calculated from routine meteorological observations. Stability corrections may be applied according to a method devised by Deardorff (1968). The flux equations are

Momentum $\tau = \rho C_m u_a^2$

Sensible heat $H = R c_p C_h (\theta_s - \theta_a) u_a$

Moisture $W = \rho C_e (q_s - q_a) u_a$

Latent heat $E = LW$

where q is the specific humidity, c_p is the heat capacity of air, L is the heat of evaporation, θ is the potential temperature, and

C_m, C_h, C_e are the drag coefficients.

This bulk aerodynamic method has wide practical applicability as it only requires the standard meteorological observations that are routinely made by the government weather agencies and ships at sea. This means that no special meteorological equipment is necessary and long time series (sometimes covering years or decades) are possible.

Four methods of determining the surface turbulent fluxes have been briefly reviewed. The eddy-correlation, vertical gradient, and dissipation techniques are usually limited to microscale events in a single place due to the difficulty of making measurements. In order to determine mesoscale and synoptic scale fluxes, investigators are usually forced to use bulk aerodynamic methods.

1.4 The Oceanic Mixed Layer

The oceanic mixed layer deserves attention as a special medium which separates the atmosphere and the deeper ocean. The oceanic mixed layer is defined as the near surface water in which properties are approximately uniform. All fluxes of momentum and heat, except for a part of the solar radiation, must first be absorbed by the mixed layer before being transferred vertically. The main way in which water properties are transferred within the mixed layer is through advection and entrainment as pointed out by Turner and Kraus (1967). One exception is the solar radiation which penetrates

passively into and sometimes below the mixed layer.

The role of the mixed layer is important because the surface fluxes are modified by the mixed layer properties. Since the mixed layer is nearly uniform on some horizontal scales of the order of tens of km and vertical scales of the order of meters, it has a large heat capacity and tends to act as a buffer on variations of air-sea fluxes of heat. However, complicated feedback mechanisms can occur which modify the surface fluxes and the ultimate exchange between the deep ocean and the atmosphere. An example is upwelling of deep water to the surface caused by the passage of an intense cyclonic storm. It is for these reasons that the dynamics and thermodynamics of the mixed layer need to be understood in order to grasp the complete scope of air-sea interactions in a local area. As an aid, models of the mixed layer are studied to develop a theoretical understanding of the mixed layer.

1.5 Mixed Layer Models

The first model of wind driven currents in the surface layer was developed by Ekman (1903) who assumed homogeneous water and constant eddy viscosity. Later, Munk and Anderson (1948) postulated a wind driven current similar to Ekman's in the upper layer. However they assumed the eddy viscosity and conductivity a function of the gradients of stability and shear. The Munk and Anderson model was

restricted to the case of a net heat flux gain through the surface. Applied to actual oceanic data, this model's predictions for mixed layer depth were too shallow.

Sometimes the ocean can be considered as two layered with the uppermost layer the relatively thin mixed layer. In a model like this, Freeman (1954) pointed out that the time changes of the mixed layer depth are proportional to the curl of the wind stress. This assumes that accelerations, heat fluxes, and currents near and below the bottom of the mixed layer are sufficiently small.

Modeling of the mixed layer processes was further advanced by Kitaigorodsky (1961). In a dimensional argument, he developed an equation for the mixed layer depth which recognized the role of wind, generated turbulence, which increases the mixed layer depth, and net heat flux gains through the surface, which tends to decrease the mixed layer depth. However, this formula applies only for the case of heat flux gain of the mixed layer.

Ball (1960) looked at the effect of thermally created turbulence in an atmospheric convection layer working against buoyancy forces and raising an inversion height. This model was analogous to that of Kraus and Rooth (1961) who developed a steady state model based solely on the balance of heat in the oceanic mixed layer. Kraus and Rooth showed that there was a balance in the vertical between the tendency of the layer thickness to increase and the entrainment of

the cold water below.

The understanding of oceanic mixed layer dynamics was greatly advanced in two companion papers of Turner and Kraus (1967) and Kraus and Turner (1967). The first paper included a laboratory tank experiment in which a two layered fluid was stirred at the top simultaneous to the addition of lighter fluid at the top. The basic concept in these papers is that the kinetic energy due to wind stirring or density overturning (due to heat loss at the surface) is converted to turbulent energy and then to potential energy. There is a balance between penetrative convection and stability forces. In addition, Kraus and Turner found that properties below the mixed layer are unaffected until the mixed layer descends and entrains the lower layers.

Another laboratory experiment on turbulent mixing was performed by Kato and Phillips (1965). They applied a surface stress to an initially quiet fluid with a uniform density gradient. They found that the entrainment velocity is proportional to the cube of the friction velocity and inversely proportional to the depth of the mixed layer and the density gradient. They confirmed that the rate of increase of potential energy of a stratified fluid is proportional to the rate of kinetic energy dissipation per unit area in a turbulent layer.

A detailed model of air-sea interaction has been developed by Pandolfo (1969). His model is based upon eddy-exchange coefficients

that connect the lower layers of the atmosphere to the upper layers of the ocean. Eight equations were developed involving two components of velocity, temperature, humidity and salinity. Variations of this model have been applied to some ocean data resulting in general agreement between the model and the data. These variations are examined in Pandolfo (1971) and Pandolfo and Jacobs (1971).

On a shorter time scale, Foster (1971) looked at the dirunal mixed layer. He solved the hydrodynamic and thermodynamic equations for the upper layers of the ocean by expanding the variables in a Fourier series and by making use of the mean field approximation. Foster used eddy-coefficients and assumed a large Prandtl Number. He also supposed that the solar heating exactly balanced the surface cooling over a complete diurnal cycle. As might be expected, Foster found that the mixed depth increased during the day and decreased at night. Further, Foster learned that increasing the eddy-coefficient increased the size of the predicted vertical convection cells.

Denman (1972) developed a time-dependent mixed layer model based on a balance between kinetic energy and potential energy. This model was developed for all cases of heat flux and momentum flux as well as for the sub-mixed layer temperature gradients. This model was applied to data taken at Ocean Station P. Agreements between the model and data were very good with mixed layer changes occurring in

time period of about a day.

Instead of an energy balance as in Denman's model, Pollard, Rines and Thompson (1973) constructed a model of the mixed layer based upon momentum. A stability criterion is used for closure. One distinctive feature of this model is that the mixed layer moves as a slab under wind stress. Secondly, the model requires that the initial current distribution must be known. A major result of this model is that inertial deepening stops at a maximum one-half a pendulum day after a step increase in the wind stress.

The most complete model of the mixed layer depth has been suggested by Niiler (1973). It is complete in that it covers time scale from much less than the inertial period to longer time periods. This model is based upon conservation of heat, momentum and energy. Consequently, this model is predominantly dominated by inertial deepening of the mixed layer for time periods less than one-half a pendulum day. On time scales greater than a pendulum day, the deepening is dominated by a balance between wind energy and buoyancy flux. This model is qualitatively a combination of the Pollard, Rhines, and Thompson inertial model and Denman's energy model.

We have reviewed here some of the theories behind mixed layer models. These ideas, along with the others presented earlier, are the basis for air-sea interaction studies. We shall use them to

examine a particular case of air-sea interaction at Ocean Station N.

1.6 Purpose of This Thesis

The purpose of this thesis is to examine the principle air-sea properties at the subtropical Ocean Station N. The second section will be descriptive and include climatological details about atmospheric and oceanic variables. The third section examines the meteorological spectra taken at Ocean Station N over periods of 3 hours to 10 years. The fourth section is about mixed layer dynamics. Finally, the last section discusses the application of Denman's mixed layer model to data at Ocean Station N.

2. DESCRIPTIVE

2.1 Introduction

The best available data for investigating the long-term characteristics of the relation between atmospheric and oceanic structure far removed from land appear to be observations made by ocean weather ships. It is the purpose of this chapter to describe the results of analyses of 20 years of oceanographic and meteorological observations from Ocean Station N (hereafter referred to as N) located at 30N 140W in the eastern subtropical Pacific. The time series are related to climatic events. Seasonal and diurnal variations are analyzed, the heat budget is computed, and the evolution of the structure of the oceanic mixed layer is described.

2.2 Observations

The climate and weather at N can best be described as moderate. Although there are seasonal variations, the temperature range is only a few degrees C and the maximum wind speed for a month infrequently exceeds 30 knots. The lower atmosphere is typically capped by an inversion with base between 900 and 850 mb. Stratoform clouds below the inversion, which are most of the total cloud cover, can yield light rain or drizzle. There is a high degree of cloudiness all year. Thunderstorms are very infrequent and the total yearly precipitation

is about 23 cm.

The North Pacific subtropical high maintains the inversion at Ocean Station N except possibly during frontal passages. Frontal passages occur most frequently during the winter. Storm centers associated with the fronts usually pass to the north but occasionally pass close to N, particularly in winter. Tropical storms are rare. Disturbances are infrequent during the summer.

N lies in the center of the East North-Pacific Central Water type (Sverdrup, 1942). The depth of the mixed layer is about 10 m during the summer, decreasing to 150 m in later winter (Bathen, 1972). Temperature decreases with depth. Salinity is a maximum at the surface and decreases with depth to 500 m, then slowly increases with depth. There may also be a small local minimum of salinity at 200 m except during the summer (Husby, 1969).

N lies on the perimeters of current gyres. According to the Climatological and Oceanographic Atlas for Mariners (1961), there is a seasonal variation in surface currents. During winter N is at the eastern extremity of a large anticyclonic current gyre with a current at N to the south or southwest of 0.1 to 0.3 knots. During winter, N is at the southwest edge of a smaller anticyclonic gyre centered at about 40 N 140W, with currents at N to the southwest at 0.1 to 0.3 knots. The current pattern during transition between summer and winter is not certain. Drogue measurements in September reported

by Husby (1969) indicated a westward current of 0.3 knots. Large wire angles have been occasionally noted during hydrographic casts at N, suggesting occasional strong currents.

The meteorological data analyzed in this study were observed at N from 1951 to 1970. The average position of N in 1951 was 33N 135W. In 1952 and 1953 N was at 32.5N 135W. For the first 10 weeks of 1954 the average position of N was 31N 140W. During the remainder of the period 1954 to 1970, the average position was at 30 N 140W.

Meteorological observations were taken every 3 hours beginning at 00 GMT each day. They included wind speed, wind direction, pressure, water temperature, dew point, air temperature, lower cloud cover, total cloud cover, and present weather. Water temperature was not observed during 1952 and the first half of 1953. Dew point was observed 4 to 6 times a day from 1953 to mid 1963. Less than 2% of all remaining observations (all variables) were missed.

A description of the meteorological and oceanographic instrumentation, location of instruments, and methods of observation is given in various U.S. government manuals, some of which are available from the Superintendent of Documents, U.S. Government Printing Office (personal communication, Marine Sciences Branch, U.S. Coast Guard, Pacific Area, San Francisco). Wind speed and direction were measured by a propeller anemometer-wind vane combination located at a height of about 25 m above mean sea level. Water temperature

was measured by use of a bucket and Hg thermometer. Air temperature and dew point were measured with a sling psychrometer on the bridge at a height of about 10 m above mean sea level.

The oceanic data (apart from the water temperature observations) considered here are from the 7-year period, 1964 to 1970. All of the observations at N during this period of time are used, both bathythermograph (BT) and hydrocast observations (salinity samples and temperature from reversing thermometers). In addition, BT and hydrocast data from other ships were used if taken within 4 degrees of 30 N 140W and between 1964 and 1970. These additional observations are only a few percent of the total. The frequency of BT and hydrocast observations was highly variable, especially the hydrocasts which were sporadic during 1964-1966, but which were at least as often as one every 3 days during 1970. The number of BT's per year ranged from 675 in 1970 to a high of 1800 in 1964.

2.3 Seasonal Variability

The seasonal variation of meteorological variables and bucket water temperature is shown in Figures 2.1 and 2.2. Each point is obtained by averaging observations over each day of the year and each particular day over the 20-year period. The resulting time series is smoothed by a 7-day running mean.

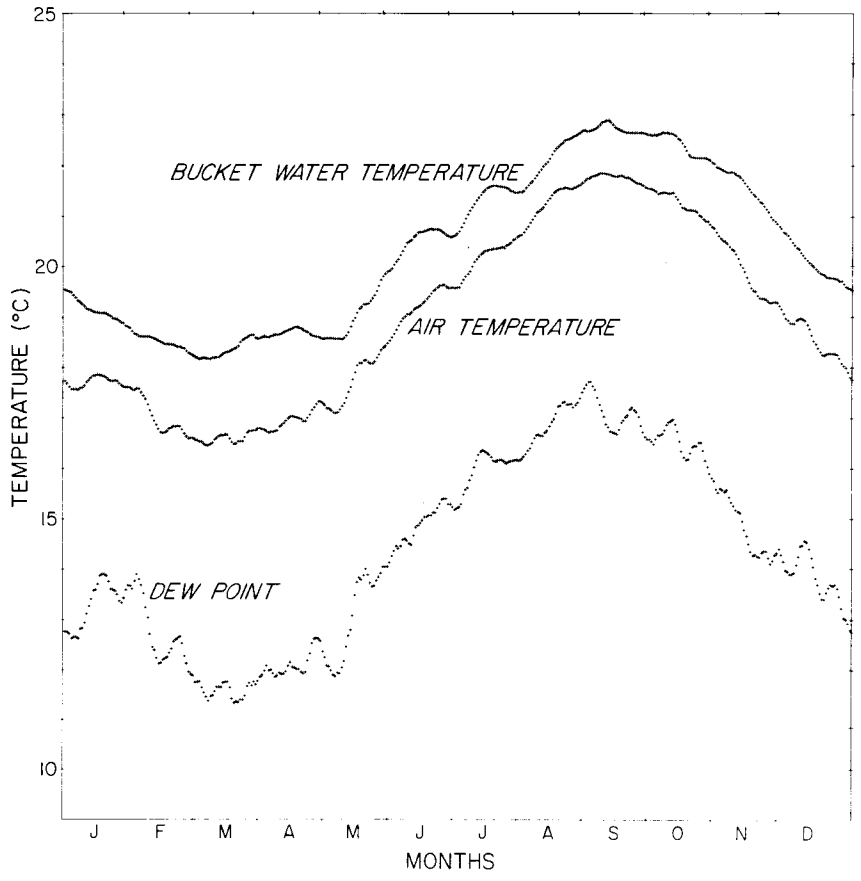

Figure 2. 1. Seasonal variations of bucket water temperature, air temperature and dew point temperature. Each point is a daily average of observations from 1951-1970 smoothed by a 7-day running average.

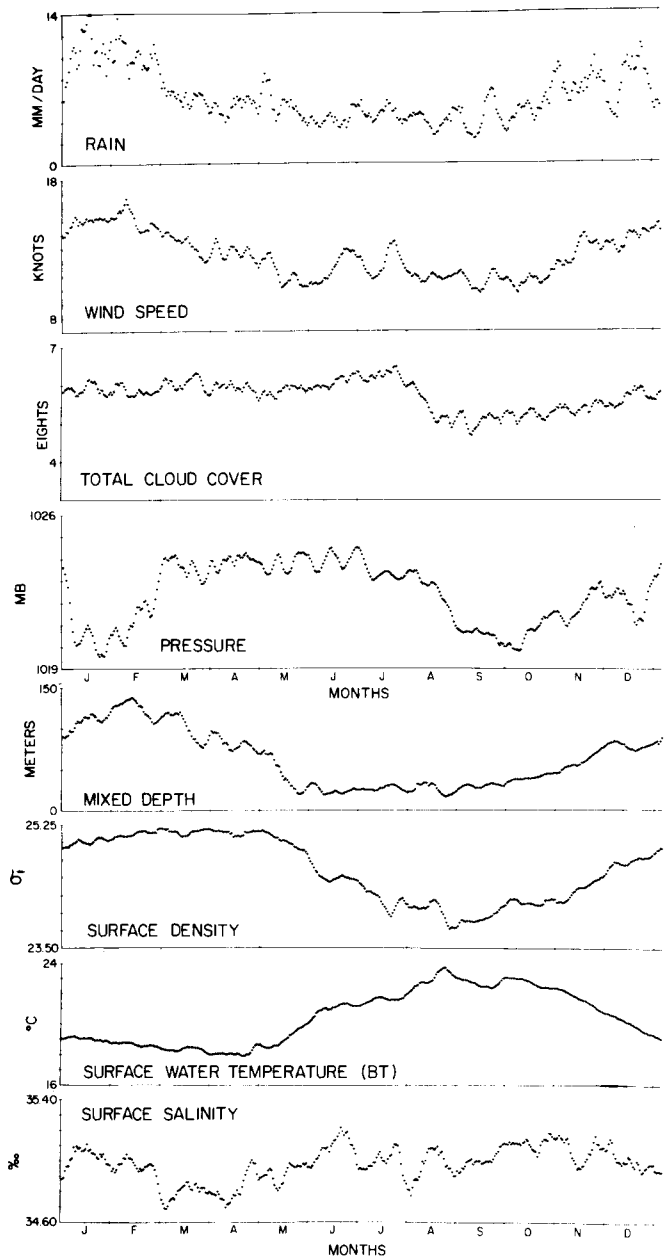

Figure 2.2. Seasonal variation of mixed layer depth, surface density, surface water temperature (BT), surface salinity, rain, wind speed, total cloud cover and pressure. Each point is a daily average of observations from 1951-1970 smoothed by a 7-day running average.

Bucket water temperature, air temperature and dew point are highly correlated showing a minimum in March and a maximum in September (Figure 2.1). The sea-air temperature difference is positive throughout the year, but larger in winter than in summer.

The rainfall estimate in Figure 2.2 is constructed from the present weather part of the synoptic observations by use of a method suggested by Tucker (1961). The rainfall is a maximum in winter and has a broad minimum in summer. An unexpected result is that the yearly total is only 225 mm, less than half that suggested for the vicinity of N by Jacobs (1951) and Budyko (1956). Elliott and Reed (1973) have expanded the use of Tucker's technique for rainfall estimates to other stations in the Pacific, showing estimates which are also much lower than previous estimates.

The seasonal variation of wind speed is similar to that for rainfall with a maximum in winter and a minimum in summer. Some of the small-scale fluctuations of wind speed and rainfall are also positively correlated, indicating, as one might expect, that anomalously high winds are associated with high rainfall. The average wind speed at any time of the year varies between 9 and 17 knots.

Cloud cover shows little seasonal variation except for a decrease of about 1/8 in August, then a gradual increase to a nearly constant value from January through July of about 6/8. On the average, about 1/8 of the total cloud cover is middle and high cloud.

Pressure exhibits a double minimum, one in late January and another in October. The pressure has a broad maximum from March to July. The minimum in January-February coincides with maximum wind speeds while the decrease in August coincides with the decrease in cloud cover. The broad maximum is associated with summer intensification and northward displacement of the North Pacific High. The mechanisms causing the secondary maximum of pressure in November and December are obscure.

The seasonal variation of the oceanic surface variables is shown in the lower 4 curves of Figure 2.2 for the period 1964 to 1970. The depth of the mixed layer, denoted by "mixed depth", is defined as the depth at which a BT temperature is 0.2 degrees C less than the surface temperature from the same BT. The surface water temperature variation is similar to the bucket water temperature as ought to be the case. The dissimilarities are likely due to the different number of years averaged. Surface density (σ_ϵ) is a near mirror image of surface temperature, indicating that salinity is of minor importance in determining density. Salinity shows very little seasonal variation. However, individual years do show minima in February or March and maxima in late summer.

A time-depth cross section showing mean seasonal temperature structure is given in Figure 2.3. The temperatures are from BT's averaged over the period 1964-1970 and smoothed by a 2-week running

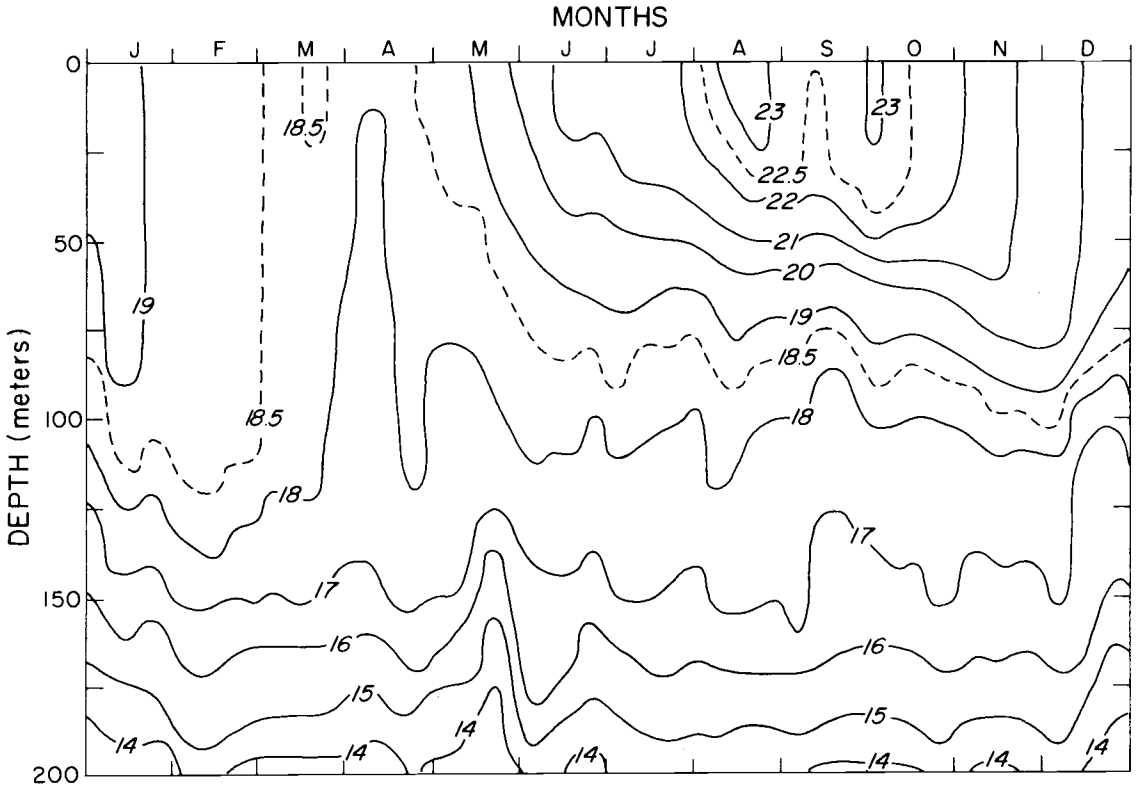

Figure 2.3. Seasonal cross section of temperature (deg C) from hydrocasts at depths given in meters for 1964-1970.

mean. The outstanding feature is the development of a warm, shallow, nearly isothermal layer in the early summer which increases in temperature during the summer and then cools and deepens in the fall and winter, reaching a depth of about 125 m in late winter. The small scale structure is statistically insignificant. The seasonal temperature structure at N is similar to that in the central North Pacific (Tully and Giovando, 1963) but the amplitude of the seasonal temperature variation is less, 5 degrees C compared to 11 degrees C in the North Pacific, and the maximal and minimal surface temperature at N are about a month later than in the central North Pacific. The evolution of the mixed layer is similar except for a delay of about a month at N for the beginning of the deepening of the mixed layer. The average maximal depth of the mixed layer which occurs in late winter is about 120 m for both locations.

A time-depth section of salinity is shown in Figure 2.4. There is little evidence of any seasonal variation, even at the surface where one might expect variations due to variations in evaporation. The seasonal density structure (not shown) is very similar to temperature. Salinity plays an insignificant role in determining seasonal fluctuations of density at N.

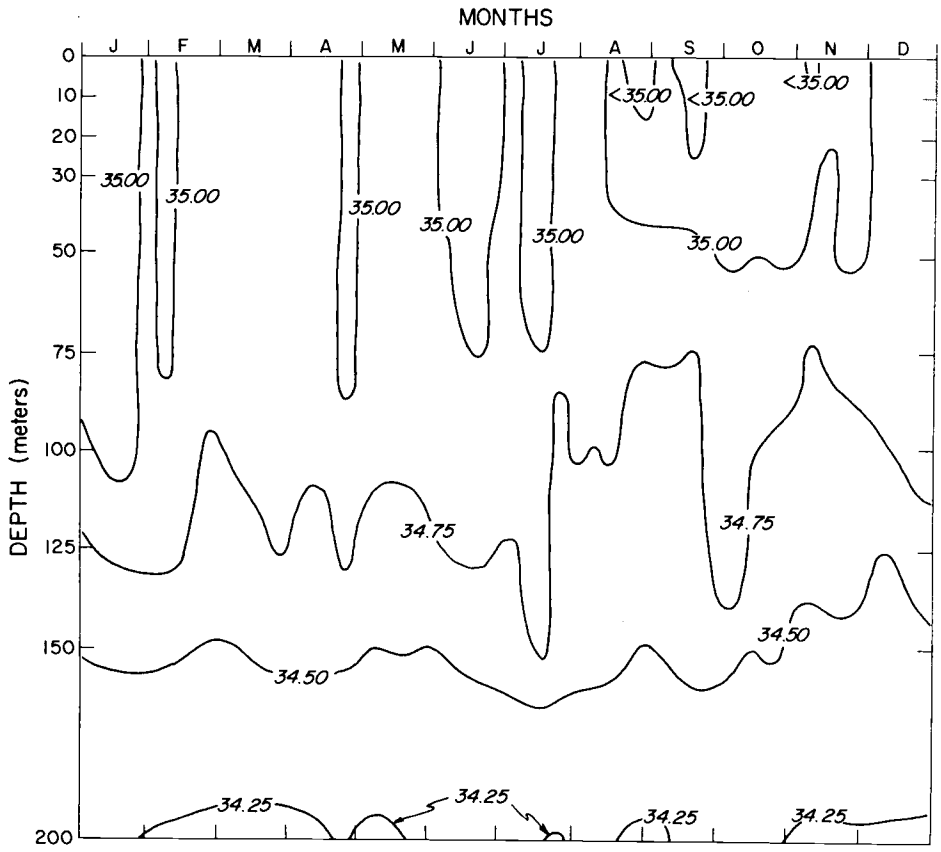

Figure 2.4. Seasonal cross section of salinity (‰) from hydrocasts at depths given in meters for 1964-1970.

2.4 Surface Heat Balance

Empirical formulas are used to estimate the heat fluxes at the sea surface. The incoming solar short wave radiation is estimated by (Berlyand, 1960)

$$Qshort = r_s(1-aC-a^2C^2)$$

where r is the reflection coefficient, s the clear sky radiation at the surface, C the fraction of total cloud cover, and a, an empirical constant which is the function of latitude. The above formula was also used by Wyrtki (1965) in his study of the heat balance of the North Pacific. However, in our case, the lower cloud amount was used in place of total cloud amount C to force the resulting heat balance more nearly to zero. The higher clouds represented on the average only about 1/8 of the total cloud cover. Including them in C has an unreasonably large effect on the estimated incoming solar radiation since they are on the average less impervious to solar radiation than lower clouds. There may also be a tendency for observers to over-estimate the contribution of high clouds to the total cloud amount when the high clouds are mostly obscured by lower cloud. For back radiation, the following formula was used (Wyrtki, 1965):

$$Qback = \sigma T_w^4(a-be_a^{1/2})(1-cC_L^2) + d\,T_w(T_w-T_a)$$

where σ is the Stefan-Boltzman constant, T_w the surface water temperature, e_a the vapor pressure of the air, and a, b, c and d are empirical constants, values of which are given by Wyrtki. The sensible and latent heat fluxes were calculated from the standard bulk transfer formulas (e.g. Malkus, 1962):

$$Qsen = \rho c_p C_d (T_w - T_a) u_a$$

$$Qlat = \rho C_d L (q_s - q_a) u_a$$

where ρ is the air density, c_p the heat capacity at constant pressure, C_d the drag coefficient, u_a the wind speed, L the latent heat of evaporation, q_s the saturation specific humidity at the surface temperature, and q_a the specific humidity of the air. C_d is taken equal 1.3×10^{-3} which is a value that was selected as it resulted in general flux agreements with other investigations. The heat balance at the surface is given by

$$Qbal = Qshort - Qlat - Qback - Qsen .$$

The above empirical formulas were applied to the monthly mean values of the observed variables at N for the period 1951 to 1970. The average seasonal variation of the fluxes and balance is shown in Figure 2.5 for the two decades, 1951 to 1960 and 1961 to 1970. The heat balance is dominated by the gain due to solar radiation and the

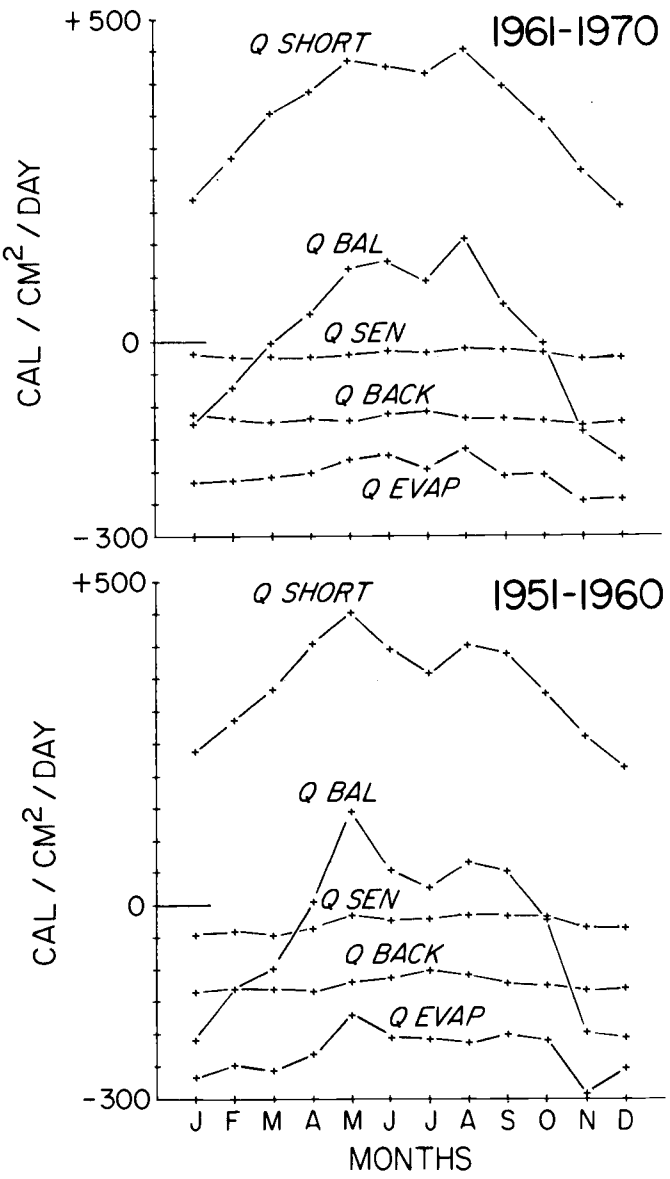

Figure 2.5. Heat balance for the two decades, 1951-1960, 1961-1970.

loss due to the flux of latent heat. The sensible heat flux is small, about 1/10 of the latent heat flux, and is a maximum during winter in the first decade but shows very little variation in the second decade. The variation of latent heat flux is also larger in the first decade, reaching a maximum in the winter. Computations based upon the three hourly meteorological values have the same basic details.

The average heat balance for the two decades is distinctly different. The first decade has a mean deficit of 40 ly/day while the second decade has a deficit near zero. The 1951-1960 decade may be partly affected by N being located 3 degrees north of its regular station from 1951-1953. However, the rest of the decade shows the same approximate annual deficit as 1951-1953.

Computations of the surface heat fluxes based upon the three hourly meteorological observations (not shown) have the same general seasonal trends as the monthly averaged meteorological values. However all of the heat losses to latent, back and sensible flux are slightly larger for the former. The heat budget based upon the three hourly meteorological observations results in a deficit average of 90 ly/day for the 1951-1960 decade and a deficit of 40 ly/day for the 1961-1970 decade.

A possible reason for the difference in heat balance for the two decades may be a change in climatic regime as suggested by Namias (1969). Namias noted a change in the thermal structure of the upper

layers of the North Central Pacific in 1961 characterized by the replacement of anomalously cool water by warmer water. This is consistent with the observed deficit in years preceding 1961 when a cool surface temperature would be associated with decreased fluxes of sensible and latent heat, as well as back radiation. It also agrees with Namias' observation that there was a cooling to great depths of surface waters in years prior to 1961.

2.5 Anomalies

Twenty-year time series of deviations from the mean, called anomalies, were constructed for various observed meteorological parameters as shown in Figure 2.6. These time series (excepting rainfall) represent deviations, following smoothing of weekly averages, from 20-year weekly means. The curves (excepting rainfall) have been smooth by a 13-week running mean. The 13-week running mean was selected as it filters out the sub-seasonal fluctuations, most of which appear to be spurious.

The plot of precipitation is estimated using Tucker's (1949) method. The deviation from the quarterly average (rather than weekly) is plotted. Due to the uncertain nature of the rainfall estimate, a quarterly average was selected in order to have each point based upon a significant amount of data.

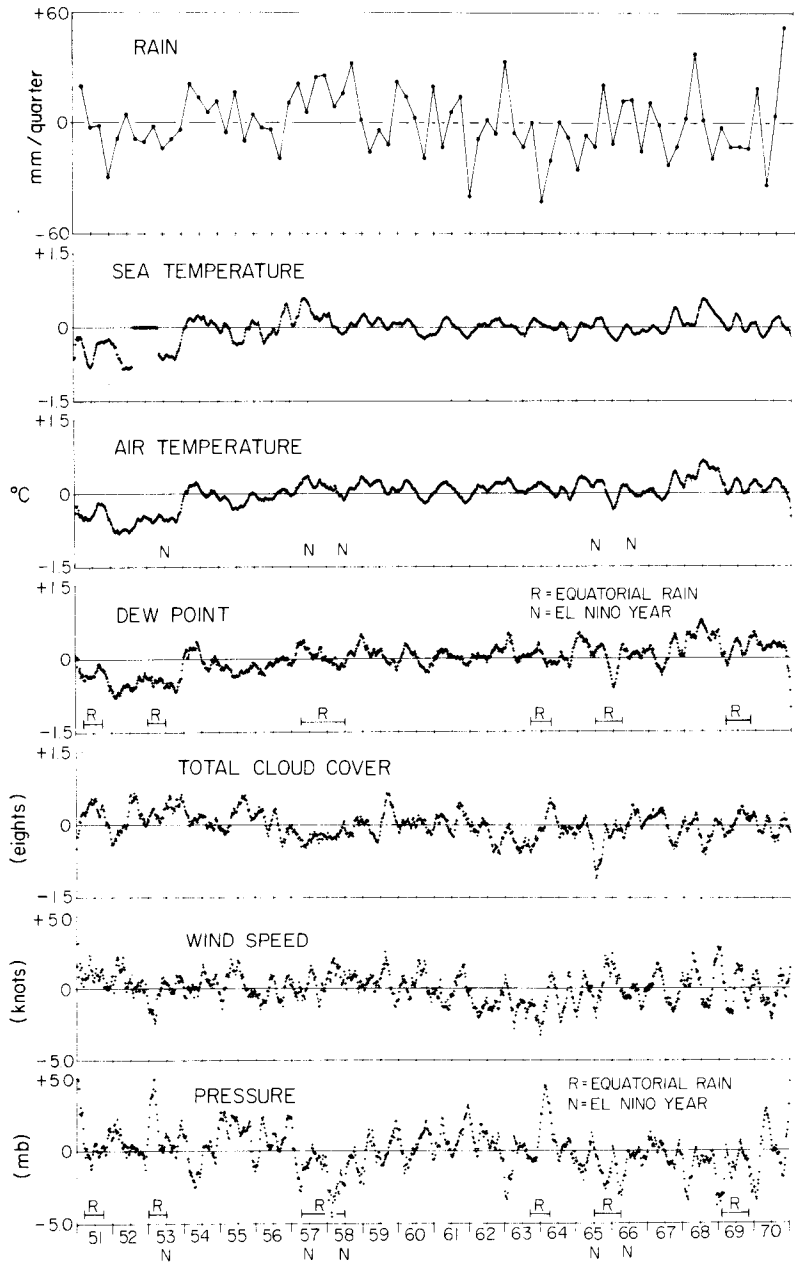

Figure 2.6. Time series of weekly means expressed as departures from the mean and smoothed by a 13-week running mean. N refers to "El Niño" and R refers to "equatorial rain".

In discussing the anomalies, the period before 1954 will be ignored as N was 3 degrees north of its regular station. In Table 2.1 and at the bottom of the anomaly graphs, certain climatic events in the equatorial Pacific for the period 1951 to 1970 are listed. These events include the El Niño and abnormal rainfall in the euqatorial Pacific dry zone (Quinn and Burt, 1972). El Niño is the term for anomalously warm water invasions associated with cessation of upwelling off the coast of Peru.

Table 2.1. Major climatic events in the Pacific.

Year	Equatorial Rain		El Niño
1951	NE		?
1952			No
1953	NE		Yes
1954			No
1955			No
1956	E		No
1957	E, NE	(strong)	Yes
1958	NE	(strong)	Yes
1959			No
1960			No
1961	NE		No
1962			No
1963	NE		No
1964	NE		No
1965	E	(weak)	Yes
1966	E	(weak)	Yes
1967			No
1968			No
1969	NE		No
1970			No

Equatorial Rain: E = extensive, NE = not extensive, no entry = none

El Niño: Yes or No.

The anomalies of sea temperature, air temperature and dew point are highly correlated and in phase. The only period in which the sea surface temperature anomaly significantly exceeds that of the air and dew point is during the 1957-1958 winter which coincided with a large scale warming of the North Pacific (Namias, 1959; Bjerknes, 1969), and the most disastrous El Niño of the 1951-1970 period (Quinn and Burt, 1972).

The most extreme variations can be seen in the pressure plots. Pressure may possibly be loosely correlated with equatorial developments. The largest and longest negative pressure anomaly is associated with the 1957-1958 equatorial rainfall and the most extreme El Niño of the 1951-1970 period. A large negative anomaly (more than -2.5 mb) is also associated with the weak El Niño of 1965-1966 and the equatorial rainfall of the same period. However, further relationships appear to be meaningless. The unusual 1957-1958 rainfall coincides with the extreme El Niño of the 1951-1970 period.

In addition to the meteorological anomalies, surface heat flux anomalies were constructed. Because of the difference in the heat balances, the heat flux anomalies were divided into the two decades 1951-1960 and 1961-1970 for reasons discussed in the previous section. In Figure 2.7, each point is the monthly heat flux computed from monthly averaged values, further smoothed by a 5-month running mean. Computations of the heat flux for each of the decades were

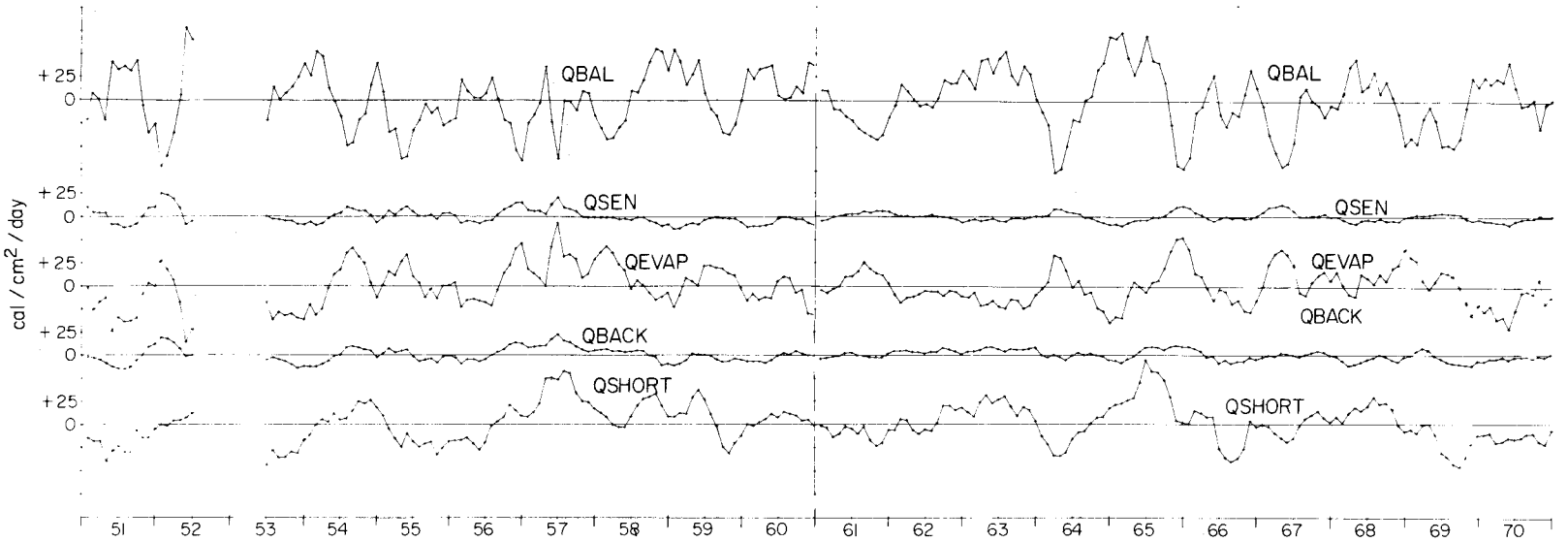

Figure 2.7. Time series of monthly means of the heat balance expressed as departures from the mean (1951-1960 and 1961-1970 respectively) and smoothed by a 5-month running mean. N refers to "El Niño" and R refers to "equatorial rain".

performed using three-hourly observations applying the flux formulas and then averaging (not shown). The time series of the heat flux based upon the three-hourly meteorological observations reveal the same essential structure for the heat fluxes based upon monthly averaged meteorological observations shown in Figure 2.7.

The heat balance is largely a reflection of the solar energy gain balanced by the loss to evaporation. The sensible heat and back radiation fluxes are minor components of the heat balance, and are in phase with the latent heat flux. The latent heat and short wave heat fluxes are generally in phase from 1953 to 1958, and 1966 to 1970 while they are out of phase from 1959-1965.

2.6 Diurnal Variation

The diurnal variation typical of a subtropical station is investigated by averaging together all of the 20 years of observations for a parameter for each of the eight 3-hourly observations in a day. Observations for a day were included only if all eight observations for that day were available so as to eliminate any bias for a particular hour. The average deviation from the daily mean of the meteorological variables is shown in Figure 2.8. The diurnal range, average and standard deviation of the variables for the seasons are given in Table 2.2. In the upper left hand corner of the figures is a bar which is the largest standard deviation on that curve divided by the square

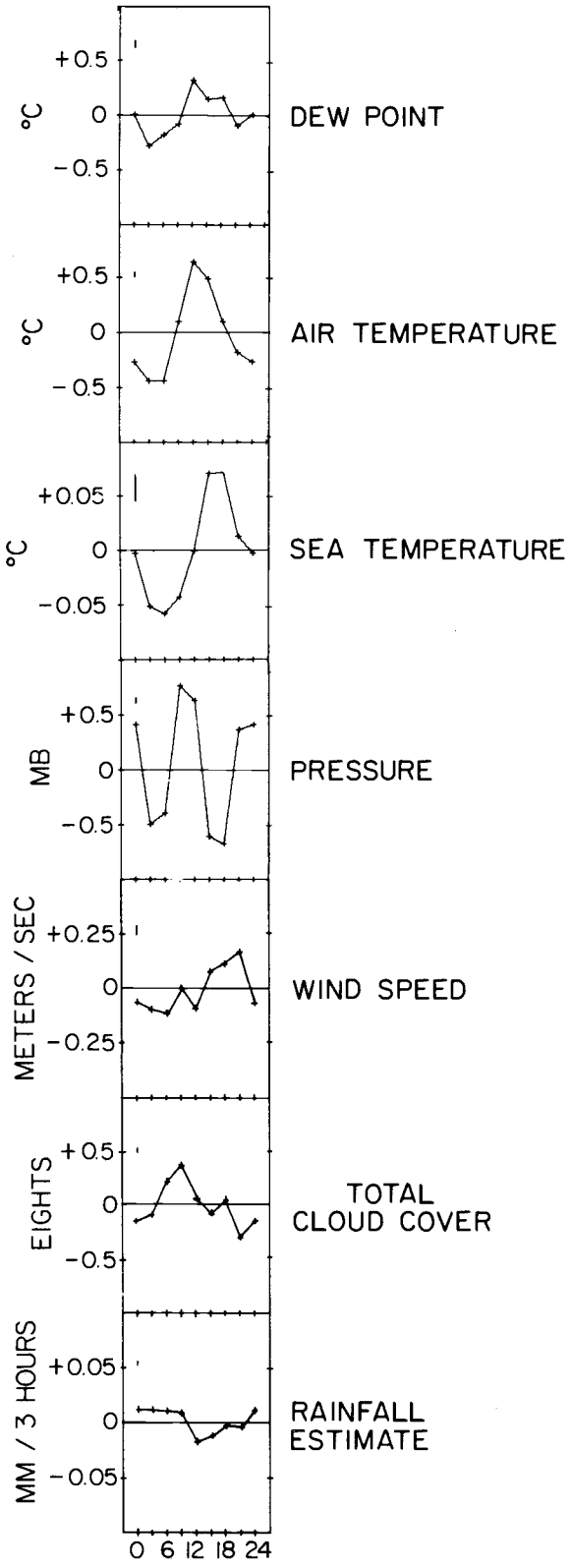

Figure 2.8. Diurnal variations expressed as departures from the daily mean. Time is local.

Table 2.2. Statistics for the diurnal deviation from the daily mean. Pressure means minus 1020 mb.

Variable	Season	Daily Mean	Daily Range	Daily Average Standard Deviation
Wind (m/sec)	W	7.3	.15	3.59
	S	6.7	.36	3.28
	S	5.7	.46	2.69
	F	5.4	.35	2.91
	avg	6.2	.31	3.22
Pressure (mb)	W	1.6	1.9	6.48
	S	3.5	1.5	5.67
	S	3.6	1.4	2.77
	F	0.9	1.6	3.52
	avg	2.4	1.4	5.01
Total cloud cover (eights)	W	5.74	.70	2.29
	S	5.93	.72	2.27
	S	6.02	.87	2.21
	F	5.19	.71	2.44
	avg	5.72	.64	2.33
T_{SEA} (°C)	W	19.71	.08	1.24
	S	18.52	.15	.99
	S	20.92	.17	1.54
	F	22.43	.15	1.16
	avg	20.41	.13	1.91
T_{Air} (°C)	W	18.17	.90	1.69
	S	16.86	1.12	1.53
	S	19.76	1.19	1.67
	F	21.29	1.14	1.32
	avg	19.01	1.08	2.28
T_{Dew} (°C)	W	13.76	.55	3.08
	S	12.22	.68	2.68
	S	15.87	.56	2.23
	F	17.02	.61	2.29
	avg	14.76	.60	3.18
Rain estimate (mm/3hr)	W	.11	.02	.487
	S	.08	.03	.367
	S	.06	.05	.269
	F	.06	.04	.324
	avg	.08	.03	374

root of the number of observations, and represents an error bar.

The diurnal variation of the sea temperature of each of the seasons has the same shape as the average for all seasons. There is a minimum of the sea temperature at 0600 L and a maximum between 1500 and 1800 L. The range of the diurnal variations for the winter is about half that of the other three seasons. The diurnal variation of the sea temperature is about that for these latitudes as cited by Roll (1965).

As with the sea temperature, the shape of the air temperature diurnal variation curve is the same for all seasons. The deviation from the daily mean of the air temperature diurnal variation has a minimum between 0300 and 0600 L, and a maximum at 1200 L. A part of the diurnal variation may be due to radiation errors (e.g. Roll, 1965).

Somewhat similar to the sea and air temperature is the deviation from the daily mean of the dew point. Also, all shapes of the seasonal curves are the same, so the average for all seasons is shown. The dew point deviation from the daily mean has a minimum at 0300 L and a maximum at 1200 L. The plateau in the dew point between 1500 and 1800 L appears in each of the seasonal curves.

The deviation from the daily mean of the diurnal variation of the surface pressure has a symmetrical semidiurnal variation. All curves of the diurnal variation of pressure have the same shape. Not

shown are the graphs of the spring and summer diurnal variations which have similar means and ranges. The minimums are between 0300 to 0600 L and 1500 to 1800 L, while the maximums are between 0900 to 1200 L and 2100 to 2400 L.

All four seasons of the deviation from the daily mean of the diurnal variation of wind speed are distinctly different, so all are shown in Figure 2.9. The diurnal variation of the wind speed has a minimum at 1200 L for all seasons and another minimum at 0600 L for all seasons except the winter. The apparent minimums in the winter diurnal variation at 0300 and 1800 L are not significant. The fall diurnal variation of wind speed has an additional minimum at 0000 L. In the spring, the diurnal variation of wind speed has a maximum at 1800 L, while in summer and fall it is at 2100 L. The spring, summer, and fall diurnal variation of wind speed have a local maximum at 1200 L, while the fall has an additional local maximum at 0300 L. It is interesting to note that the winter range of diurnal variation for the wind speed is at least half that of the other seasons. From these data, a slight semidiurnal trend can be seen in the variation of the wind speed, particularly during the spring through fall, which is to be expected (Roll, 1965). However, the range of the diurnal variation of wind speed at N is only about half that suggested by Roll (1965) as being typical of these latitudes.

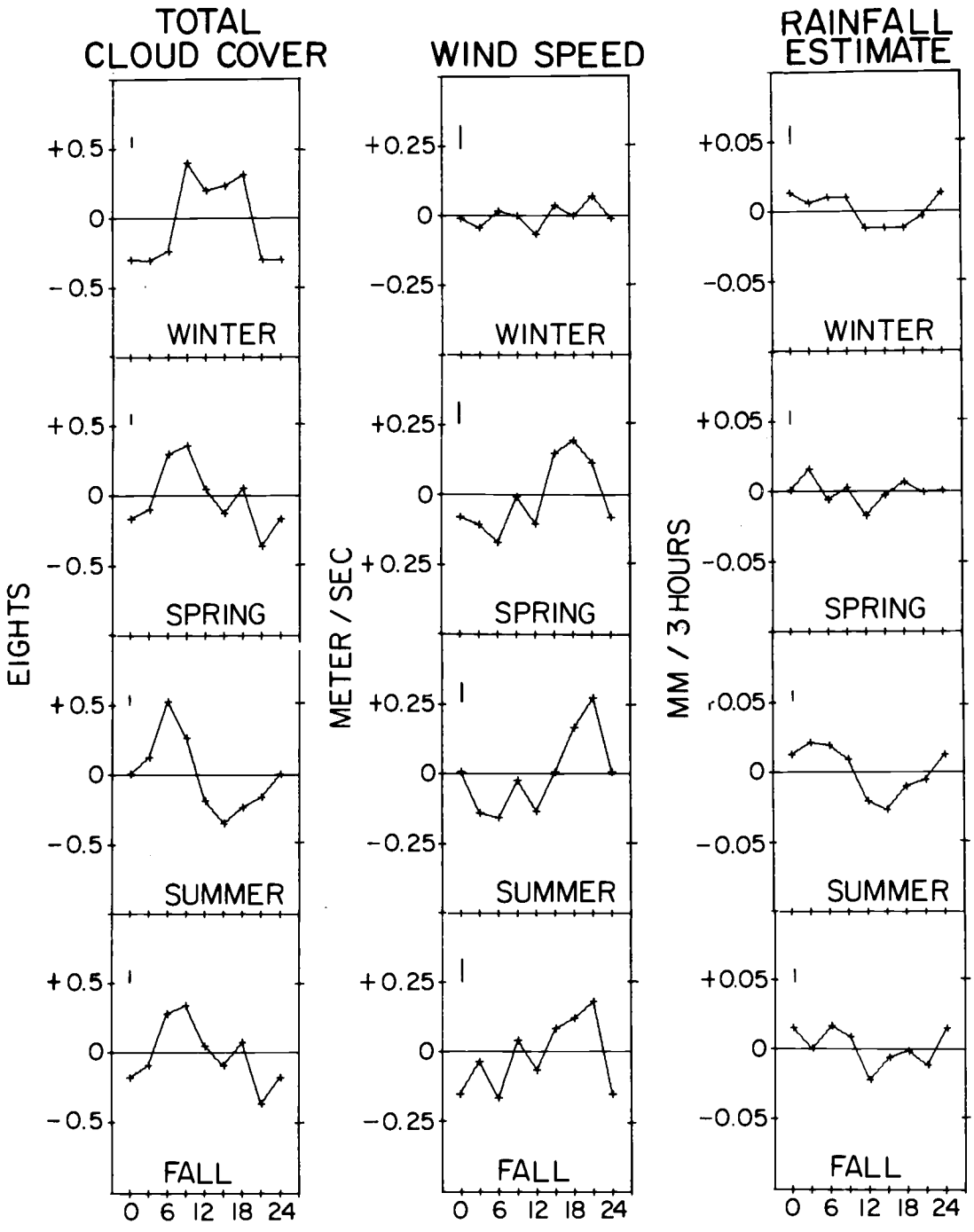

Figure 2.9. Diurnal variations of the wind speed, cloud cover and rainfall. Each is expressed as departures from the daily mean for four seasons.

Another complicated diurnal variation is that of the total cloud cover, so all four seasons are shown in Figure 2.9. The winter diurnal variation of the total cloud cover has a maximum at 0900 L and a local maximum at 1800 L. Spring and fall diurnal variation of the total cloud cover are exactly the same with a minimum at 1500 and 2100 L, as well as maximums at 0900 and 1800 L. The summer diurnal variation of the total cloud cover has one maximum at 0600 and one minimum at 1500.

The last diurnal variation to be considered here is that of the rain estimate (Figure 2.9). A rain estimate is derived from the "present weather", part of the synoptic observation by the method previously described. The graphs are constructed in the same manner as the previous diurnal trends, except that the vertical axis is ±.01 mm/3 hrs. The winter deviation from the daily mean of the diurnal trend of the rainfall has a broad maximum from 0000 to 0900 L, with a broad minimum from 1200 to 1800 L. The spring diurnal trend of rain does not have a distinct variation except for the largest maximum at 0300 L and the lowest minimum at 1500 L. However, the summer rainfall does have a diurnal variation with a maximum centered between 1500 and 1800 L. Finally, the fall diurnal trend is confused with maximums at 0000, 0300 and 2100 L.

2.7 Advection at Ocean Station Vessel N

We need to estimate the change of the mixed layer temperature (assumed uniform and equal to the surface temperature) and depth due to advection. In a following section we apply Denman's model to N data, and we can then determine the extent of the influence of advection on these variables. The basic formula used in calculating changes due to advection follows. Suppose we have some variable scaler A. The total change of A is then

$$\frac{dA}{dt} = \frac{\partial A}{\partial t} + \vec{u} \cdot \vec{\nabla} A$$

where the last term is the advection component and $\vec{u}$ is the velocity field. Further suppose that the variables may be divided into an average (denoted by an overbar) and a fluctuating component (indicated by a prime) such that

$$A = \overline{A} + A'$$

$$\vec{u} = \overline{\vec{u}} + \vec{u}'$$

Then the advective term averaged is

$$\overline{\vec{u} \cdot \vec{\nabla} A} = \overline{\vec{u}} \cdot \vec{\nabla} \overline{A} + \overline{\vec{u}' \cdot \vec{\nabla} A'}$$

The $\overline{\vec{u}' \vec{\nabla} A'}$ term is virtually unmeasured in the ocean mixed layer

on a scale greater than a few hours at isolated locations. Since there is no realistic way of estimating this term, the usual procedure is to ignore it. However, it is not unrealistic to expect that there could be eddies or organized motions on a horizontal scale in the ocean on synoptic scales, particularly since these atmospheric scales tend to drive the ocean surface layer. But, without any measured details, the turbulent transport term $\vec{u}' \cdot \nabla T'$ will have to be assumed to be zero. The advective change is assumed to be

$$\frac{dT}{dt} = \bar{\vec{u}} \cdot \nabla \bar{A}$$

Surface Layer Horizontal Gradients

The surface layer temperature gradient is taken from the Climatological and Oceanographic Atlas for Mariners Volume II (1961). The mixed layer depth gradient is taken from Bathen (1972).

Velocity Field

The surface layer current vector is assumed to be equal to the mixed layer currents which are also uniform throughout the layer. Some evidence of this is cited in Pollard et al. (1973). Five methods of estimating the surface currents will be used. The first is a climatological average from the Climatological and Oceanographic Atlas for Mariners Volume II (1961). The second estimate is also a

climatological average taken from Tully (1965).

The third current estimate comes from geostrophic computations based upon hydrographic data. A level of no motion is assumed at 800 meters. Examination shows that the baroclinic shear is insignificant at or below this level. The surface current velocity is given by

$$u = \frac{10}{f}\left(\frac{\Delta a - \Delta b}{\Delta X}\right)$$

where u is the current velocity in cm/sec, Δa and Δb are the sums of the dynamic depths at each station in meters, and f is the Coriolis force. Hydrographic data was supplied by the NOAA Oceanographic data center, which also computed the dynamic depths.

A fourth current estimate is also based upon the dynamic depth. In this case, the dynamic depth gradient at N is a climatological average taken from Fairbridge et al. (1966).

The fifth type of current estimation comes from the Ekman drift. The Ekman drift current is the current resulting from the direct action of the wind stress on the sea surface. These drift currents are computed by Wickett and Thompson (1971). Their computations are based upon the assumption that the surface transport is 90 degrees to the right of the geostrophic surface wind, which in turn is computed from monthly mean surface pressures. These calculations also assume instant response by the sea to the wind stress and ignore

existing sea currents.

Temperature Advection in May, 1969

The temperature advection estimates vary widely as shown in Table 2.3. Various methods estimate the advection at N to be in the range of -.5 to +.3 degrees C/17 days. The large negative estimates from the Mariner's Log are probably due to excessive current range (only one current range is given for the whole year). Also, the actual vector orientations, which are very important, are difficult to determine in the Mariner's Log.

Temperature Advection in December, 1970

The December temperature advection estimates are at least in better agreement than the May case. The range of temperature estimates run from -2.1 to -.1 °C/15 days. The larger negative temperature advection may be more realistic since the North Pacific gyre is strengthened in December resulting in stronger currents.

Mixed Layer Advection

The mixed layer depth gradient is quite small for all seasons. Realizing that $|\vec{u}||\vec{\nabla D}| \geq |\vec{u} \cdot \vec{\nabla D}|$, the former is less than 5 m/17 days, even for the largest estimate.

Table 2.3. Advection estimates.

May temperature advection

Atlas	-.81 °C/17 days to -2.43 °C/17 days
Tully	-.49 °C/17 days
Fairbridge	-.21 °C/17 days
Bottle	+.32 °C/17 days
Ekman	+.02 °C/17 days

Mixed layer depth advection

Maximum estimate less than 5 m/17 days

December temperature advection

Atlas	-.72 °C/15 days to -2.15 °C/15 days
Tully	-.44 °C/15 days
Fairbridge	-.10 °C/15 days
Bottle	-.29 °C/15 days
Ekman	+.01 °C/15 days

Mixed layer depth advection

Maximum estimate less than 1 m/15 days

Legend:

Atlas = Climatological and Oceanographic Atlas for Mariners (1961).
Tully = Tully (1965).
Fairbridge = Fairbridge et al. (1966).
Bottle = Computation from hydrographic data.
Ekman = Wind drift estimate from Wickett and Thomson (1971).

2.8 Summary of Descriptive Section

Meteorological and Oceanographic variables were analyzed based upon 20 years and 7 years of data, respectively. These variables, which include sea temperature, air temperature, dew point, rain, wind speed, pressure, mixed layer depth, and surface density, all have a significant seasonal trend. Another variable, the total cloud cover, has only a weak seasonal trend with a yearly average of about five-eighths. Most of the cloud cover is due to low stratiform clouds. As the surface salinity does not have a significant seasonal trend, and the surface density does, it is concluded that the salinity does not have a significant effect on the seasonal surface density. In addition to the seasonal trend, the surface pressure has a local maximum at the end of December and early January. The yearly average rainfall is only 225 mm, less than half of previous estimates.

The cross section of temperature with depth is as expected, with the large seasonal trends in the near surface. But the salinity cross section does not have a significant seasonal trend. A cross section of density appears to be similar to the temperature, and it is concluded that the seasonal trend of the subsurface density is a function of temperature.

The seasonal variation of the surface heat balance also has a seasonal trend. However, the two decades have distinctly different

balances, with the 1961-1970 decade having a larger average than the 1951-1960 decade. This heat balance change coincides with a large scale climatic change in the North Pacific (Namias, 1963).

Of the 20-year anomalies, the extreme pressure anomalies in some cases may correlate with anomalous large scale events in the equatorial Pacific. The total cloud cover, rainfall and sea temperature-air temperature reflect the 1957/1958 large scale climatic changes in the equatorial zone which included the extreme El Nino occurrence of the 1951-1970 period.

The sea temperature, air temperature, dew point, pressure, wind speed, and total cloud cover all have distinct diurnal trends. The wind speed, rainfall, and total cloud cover also have significantly different diurnal trends during each of the four seasons.

Advective effects at N were also examined from the available data. The advection of temperature may be a significant portion of the total change in the surface temperature except during the summer. This probably results from the decreased current speeds experienced in summer. The mixed layer depth changes are always locally generated.

3. SPECTRA

3.1 Introduction

The ten-year time series (1961-1970) of surface meteorological observations at N was spectrally analyzed. The variables analyzed were wind speed, pressure, sea temperature, air temperature and dew point. The parameters were examined in two ways: (1) spectra of the 10-year record and (2) spectra of the 4 seasons averaged over 10 years. Since long term spectra of open ocean stations have been seldom available, these spectra have particular significance in identifying the dominant scales of synoptic and longer-period air-sea interaction processes. Besides their descriptive value, open-ocean surface spectra can provide forcing conditions or be used for comparison to the results of mathematical models of the atmosphere and ocean.

The data used in this paper were taken at N during the period 1961 to 1970 when its average position of N was 30 N 140W. The meteorological observations were taken every 3 hours except for dew point which was taken only from four to six times a day from 1961 to the first half of 1963. Excepting the dew point from 1961 to 1963, less than 2% of the observations were missed. The effect on the spectra of the missing observations is expected to be small which is supported by a study of upper level wind and temperature spectra by

Chiu (1960) who found that there was no significant change in the spectra if up to 10% of the observations were missing. The missing observations were filled in by linear extrapolation.

3.2 Analysis

The longest records analyzed were 10 years in length. For each variable, every seven points of the first 28,672 data points beginning in 1961 (almost 10 years) were averaged together, creating a record of 4096 points. This record of 4096 averaged points was transformed by use of the Fast Fourier transform and an autospectrum produced of 2048 spectral estimates (ϕ). The autospectrum was then averaged over equal intervals of the logarithm of frequency resulting in a smoothed spectrum of 22 uncorrelated estimates.

Spectra were also computed by breaking the 10-year time series into 4 month periods for a total of 28 blocks. (This division actually fell short of the 10-year period by a few days.) Each 4-month period or block, consisting of 1024 points, had, unlike the 10-year record, notable energy at the annual distinct trends due to annual variations. Before the 4-month variables were Fast Fourier transformed, each block of 1024 points had the trend removed. The blocks were then Fast Fourier transformed and an autospectrum created. The autospectrum of each block was logarithmically band averaged in the same manner as for the 10-year spectrum. The 4-month spectra were then

combined with the 10-year spectra to give a single spectra over the range of periods from 6 hours to 10 years. In the region of overlapping frequency, the values from the 10-year spectra were used.

Seasonal spectra were also computed. From the 10 year data series, each variable was divided into blocks of 256 points (32 days). It was arranged so that each calendar year has twelve 256 blocks that nearly corresponded to calendar months by overlapping the last 256-point block of the year by a few points. Each of the 256-point blocks was detrended, Fast Fourier transformed and an autospectrum computed. This autospectrum was logarithmically band averaged as described previously. The band averages of the 256-point blocks were averaged according to the four seasons, each season containing averages over 3 blocks (months) for each of 10 years. The final result was four seasonal autospectra for each variable, each containing 14 smoothed spectral estimates.

In addition to the standard spectrum analysis, rotary spectra were calculated for wind speed. The theoretical basis for a rotary spectrum is discussed in Mooers (1970) and Gonella (1972).

The basic foundation of rotary spectrum analysis is that a two-dimensional vector varying in time can be transformed to frequency space and uniquely represented as two oppositely rotating vectors for each frequency. To sketch this process, consider a two-dimensional vector in time and space.

$$u = u_x + iu_y$$

This vector may be complex demodulated into

$$u = \sum^{\omega=\infty} u_a(\omega) + iu_b(\omega) \ .$$

The original vector may also be thought of in the form of the inverse Fourier transform,

$$u = \sum_{j=-\infty}^{+\infty} U_j e^{i\omega_j t} \ .$$

Consider a particular frequency ω_0; then

$$u_a(\omega_0) + iu_b(\omega_0) = U_+ e^{i\omega_0 t} + U_- e^{-j\omega_0 t}$$

Here U_+ and U_- are the Fourier amplitudes that represent the amplitude of positively and negatively rotating vectors, both rotating at the same frequency. If $U_+ = U_-$, then the resulting vector u at this frequency is only oscillating along a line. If U_+ or U_- is zero, then the vector u moves in a circular motion for this frequency. Usually, U_+ and U_- are non zero and not equal. Thus, the rotational autospectrum illustrates the intensity and the sense of the rotation or turning of a two-dimensional vector.

Both 10-year and seasonal rotational spectra were created for the wind in a manner similar to that discussed in the preceding sections. The difference was that the separate north and east components of the wind velocity were formed (the 4-month and the seasonal time series were detrended) and then Fast Fourier transformed. These Fast Fourier coefficients were manipulated so as to produce rotational spectra analyzed over frequency bands and blocks. The averaging schemes, band frequencies, etc., are the same for the rotational 10-year and seasonal spectra as for the corresponding spectra discussed before.

Although it is impossible to determine exactly the extent of aliasing, it is likely small. The wind, air temperature, dew point and pressure observations are averages of the order of a minute. The sea temperature is taken as the temperature of a bucket of water taken from near the surface. Aliasing will occur due to variations with periods of less than 3 hours. For all variables, the energy density falls off rapidly up to the Nyquist frequency. It is also expected that the energy density for all variables either levels off or decreases at frequencies greater than the Nyquist frequency. Examples of energy density leveling off or decreasing at higher frequencies is referred to in Busch et al. (1973). Therefore, the aliased energy should be small except perhaps at the highest frequencies.

Two types of plots are used in this paper. The first is a plot of $f \cdot \phi$ v.s. log f for an autospectrum. Such a plot conserves variance; that is, equal areas under the curve contribute equally to the total variance. Log f is used rather than ln f since frequencies are more identifiable from log f than ln f. Care should be taken in the interpretation of peaks in this plot since a maximum or minimum in a $f \cdot \phi$ vs log f plot is not necessarily a maximum or minimum in a ϕ vs f plot. The hatch mark in the upper left hand corner is an 80% confidence interval for the synoptic peak, calculated according to Blackman and Tucky (1958). A plot of log ϕ vs log f is also presented. This type of plot most directly presents the actual spectral value of the autospectrum and is useful for identifying power laws. However, equal areas under the curve do not contribute equally to the total variance. For this plot, an 80% confidence interval is drawn on the spectral estimate at the 10-day period.

3.3 Wind

We will first consider the 10-year wind-speed autospectrum. A plot of $f \cdot \phi$ vs log f (Figure 3.1) shows a broad maximum around an 8 day period and a spike at the annual period. A plot of log ϕ vs log f for the 10-year wind-speed autospectrum is shown in Figure 3.2. As might be expected, the spectrum of the wind-speed is a minimum at the shortest period and increases to a period of a year.

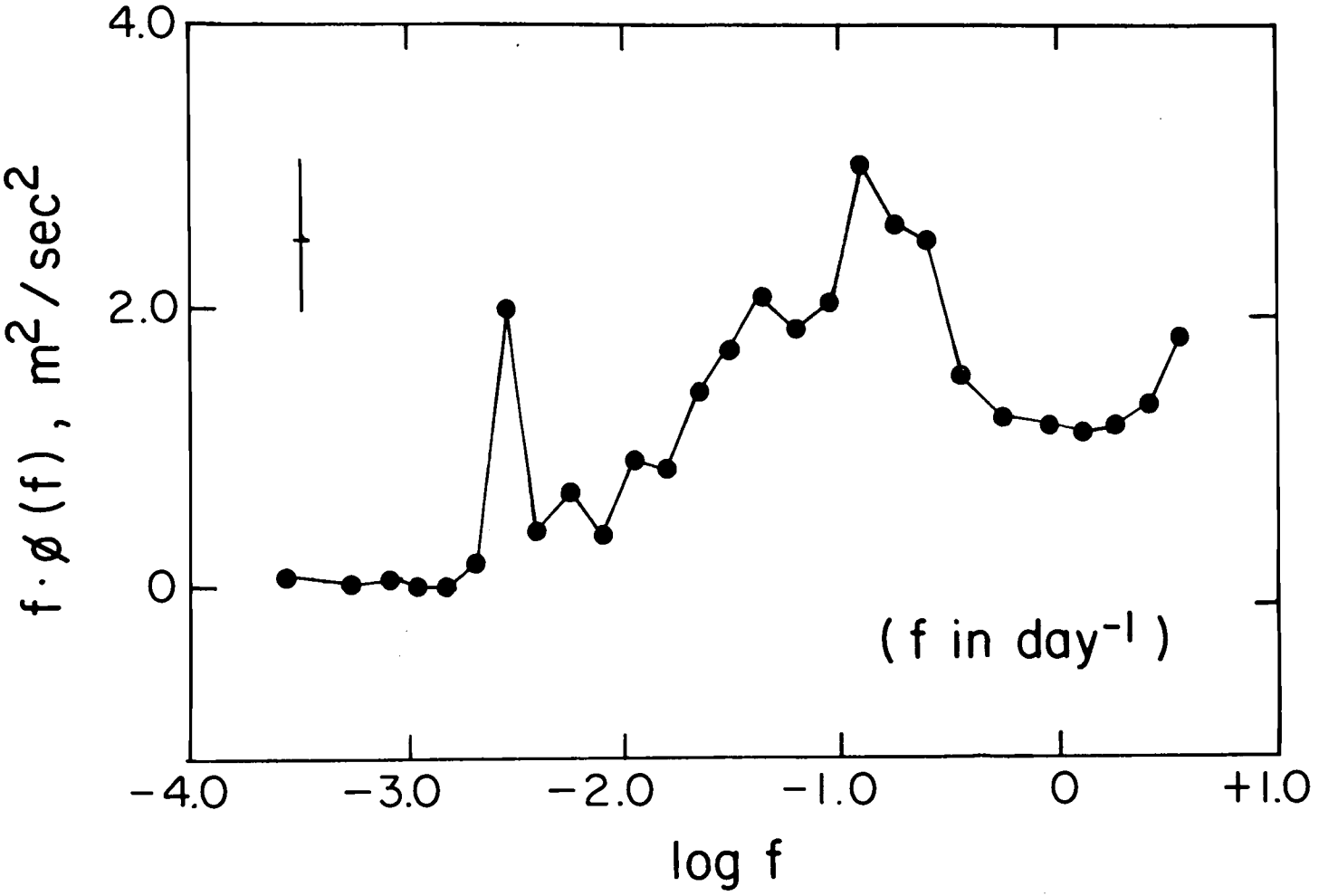

Figure 3.1. A $f \cdot \phi(f)$ vs log f plot of the 10-year composite wind speed spectrum.

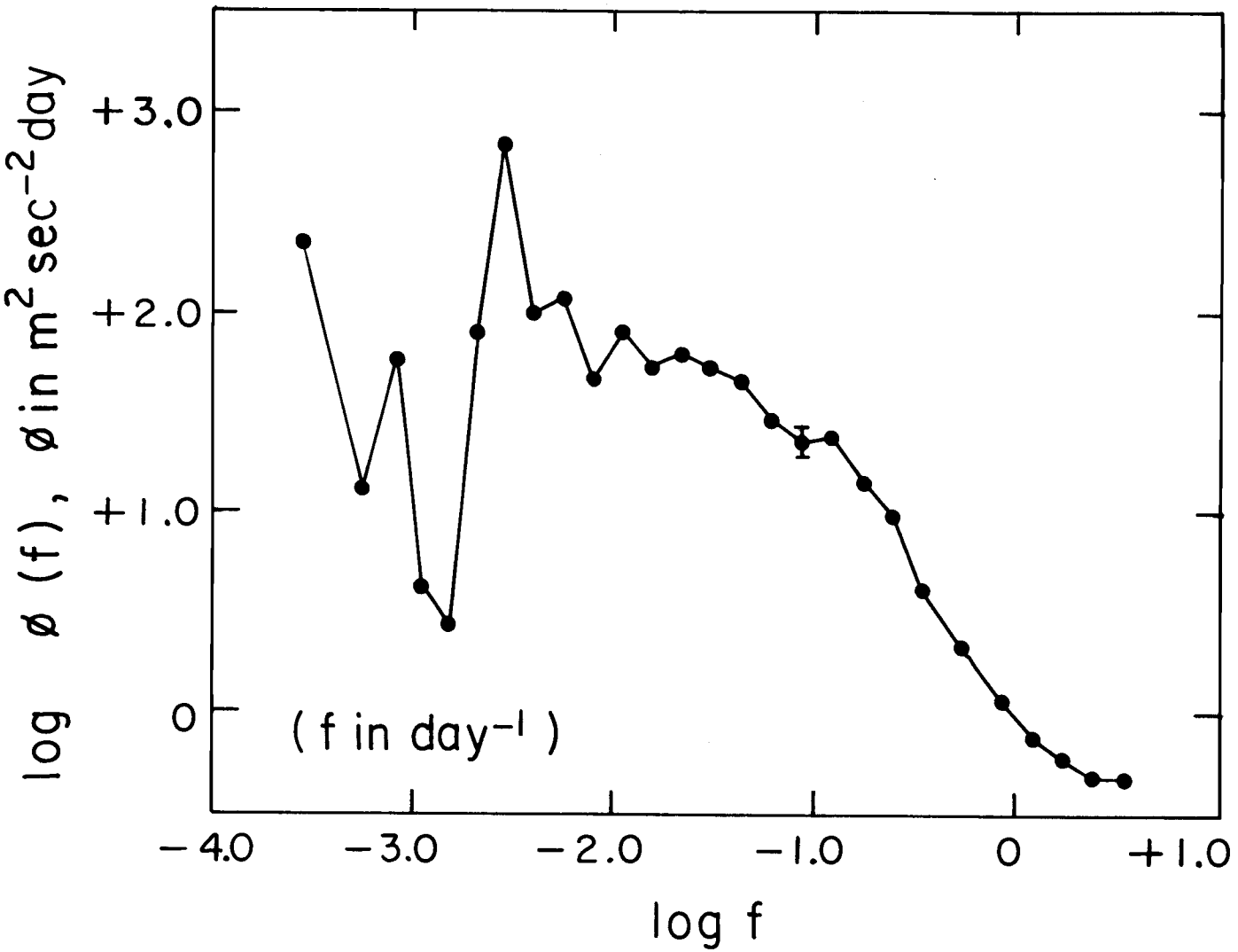

Figure 3.2. A log $\phi(f)$ vs log f plot of the 10-year composite wind speed spectrum.

The annual period of the wind spectral estimate appears as a spike. At periods greater than a year, the spectral values wander. It should be noted that these longest periods have little statistical significance due to the few unaveraged spectral estimates that make up these band averages.

The seasonal wind speed spectrum is shown in Figure 3.3. Only winter and summer spectra are plotted. Fall and spring spectra generally lie between the summer and winter curves. The winter spectrum has the most energy and is more sharply peaked than the spring spectrum. The spring and fall spectra have about 1/3 less energy at the peak than the winter wind-speed spectrum (see Table 3.1). In the summer wind-speed spectrum the peak is at 15.9 days, which is a much lower period than the other seasonal wind-speed energy peaks. All seasons have an increase from about a .5 day period to the shortest period. Without band averaging, the wind-speed autospectrum has prominent peaks at the diurnal and semi-diurnal periods (see Table 3.2).

In comparing wind speed-spectra at N with other data, we find similar qualitative results. Millard (1971) constructed a wind spectrum from buoy data in the Atlantic along 70 degrees W between 30 and 40 degrees North. The spectrum was constructed ranging from a period of 2 seconds to 20 days. The spectrum ($f \cdot \phi$ vs log f) has an energy peak at a period of a little more than 4 days, with a value of

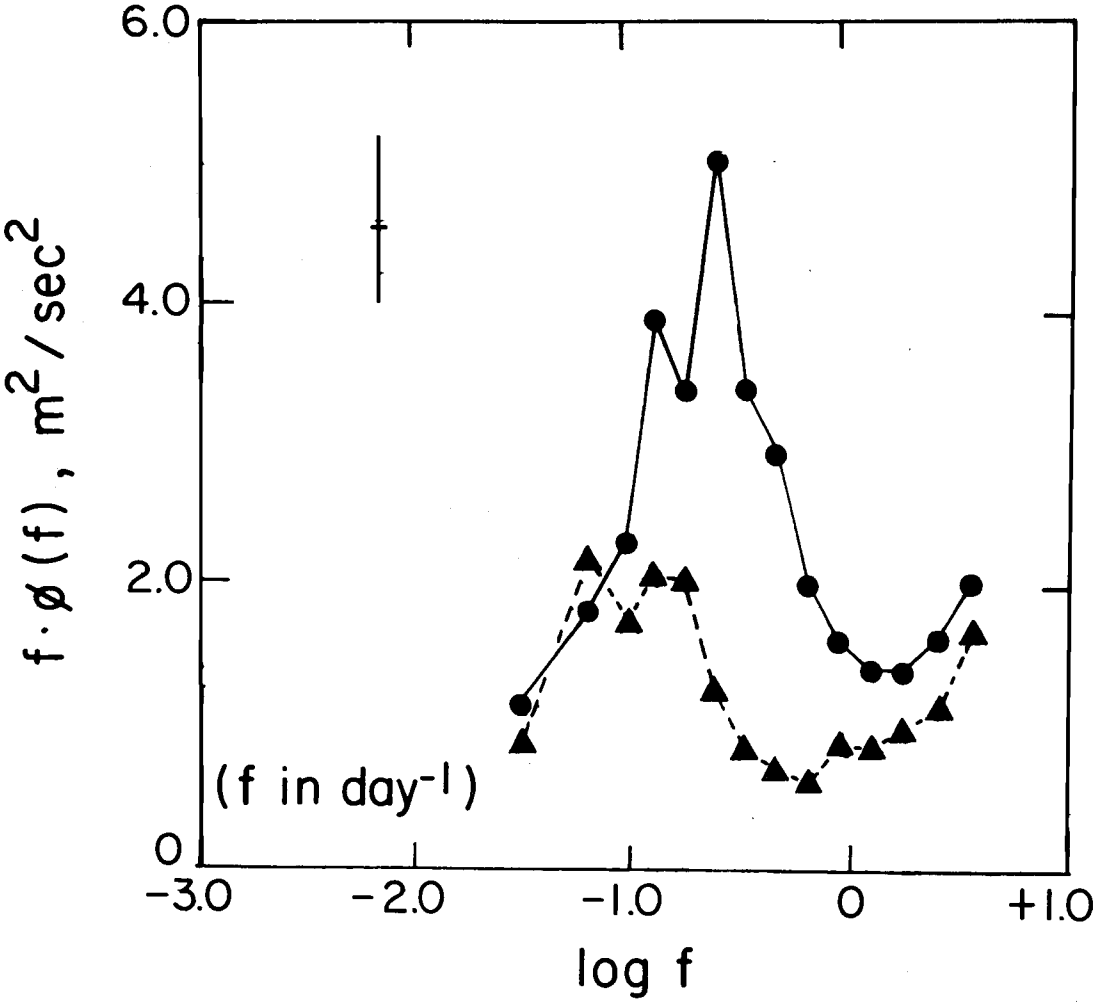

Figure 3.3. A $f \cdot \phi$ vs log f plot of the seasonal wind speed spectrum (circles are the winter spectra and the triangles are the summer spectra).

Table 3.1. Integrals of the spectra.

Variable	4096 (10 year)	1024 (4 month)	Winter	Spring	Summer	Fall	Average of Seasons
T_{Sea} ($°C^2$)	3.59	.458	.339	.476	.417	.427	.415
T_{Air} ($°C^2$)	4.48	1.34	1.25	1.14	.733	.915	1.01
T_{Dew} ($°C^2$)	8.52	5.27	5.82	5.09	1.90	4.26	4.27
Press (mb^2)	24.0	22.3	36.0	16.7	5.94	13.9	18.1
Wind (m^2/sec^2)	8.59	10.8	12.0	8.75	7.53	9.38	9.41
Clockwise rotation (m^2/sec^2)	11.1	12.0	17.1	9.17	4.20	10.0	10.1
Counterclockwise rotation (m^2/sec^2)	6.68	6.97	8.27	5.51	3.43	5.15	5.59

Table 3.2. Diurnal and semidiurnal spectral densities of the individual Fourier frequencies (not band averaged).

	Diurnal	Semidiurnal
T_{Sea} ($°C^2$ sec)	7.54	5.26
T_{Air} ($°C^2$ sec)	16.7	2.02
T_{Dew} ($°C^2$ sec)	3.35	.511
Pressure (mb^2 sec)	3.30	38.2
Wind (m^2 sec^{-2} sec)	2.00	1.39
Clockwise rotation (m^2 sec^{-2} sec)	2.74	1.95
Counterclockwise rotation (m^2 sec^{-2} sec)	1.20	.445

about 6 m^2/sec^2. This compares with the N wind spectrum which has a peak between 4.5 days and 8 days. The N wind spectrum energy is about 2.9 m^2/sec^2, less than that for the Atlantic buoy data. However, the difference is due to the latter being taken further North where there is more synoptic activity.

Another composite wind spectrum for the Atlantic has been constructed by Byshev and Ivanov (1969). They divided several island and weather ship stations in the Atlantic into zones of 40-60N, 30N-30S and 40-60S. They found a maximum of wind energy ($f \cdot \phi$ vs log f) between 11.6 and 6.4 days, with the longest period of the maximum at the equator. The 40-60N section is most like the spectrum at N, with an energy peak of about 5 m^2/sec^2. The energy peak in the 30N-30S band is about 10^{-1} m^2/sec^2. This is comparable with the N spectrum, which had a peak of 3 m^2/sec^2 between periods of 4 and 8 days. N is really typical of a latitude between the 40-60N and 30N-30S zones selected by Byshev and Ivanov, so it is not surprising that the wind-speed spectral peaks at N are also between the values of the Atlantic zones of 40-60N and 30N-30S.

The wind rotary spectrum consists of the clockwise (or negative) component and the counterclockwise (or positive) component. Both are shown together in Figure 3.4. The clockwise component is greater than the counterclockwise component at short periods up to periods less than a year. The clockwise amplitude being larger than

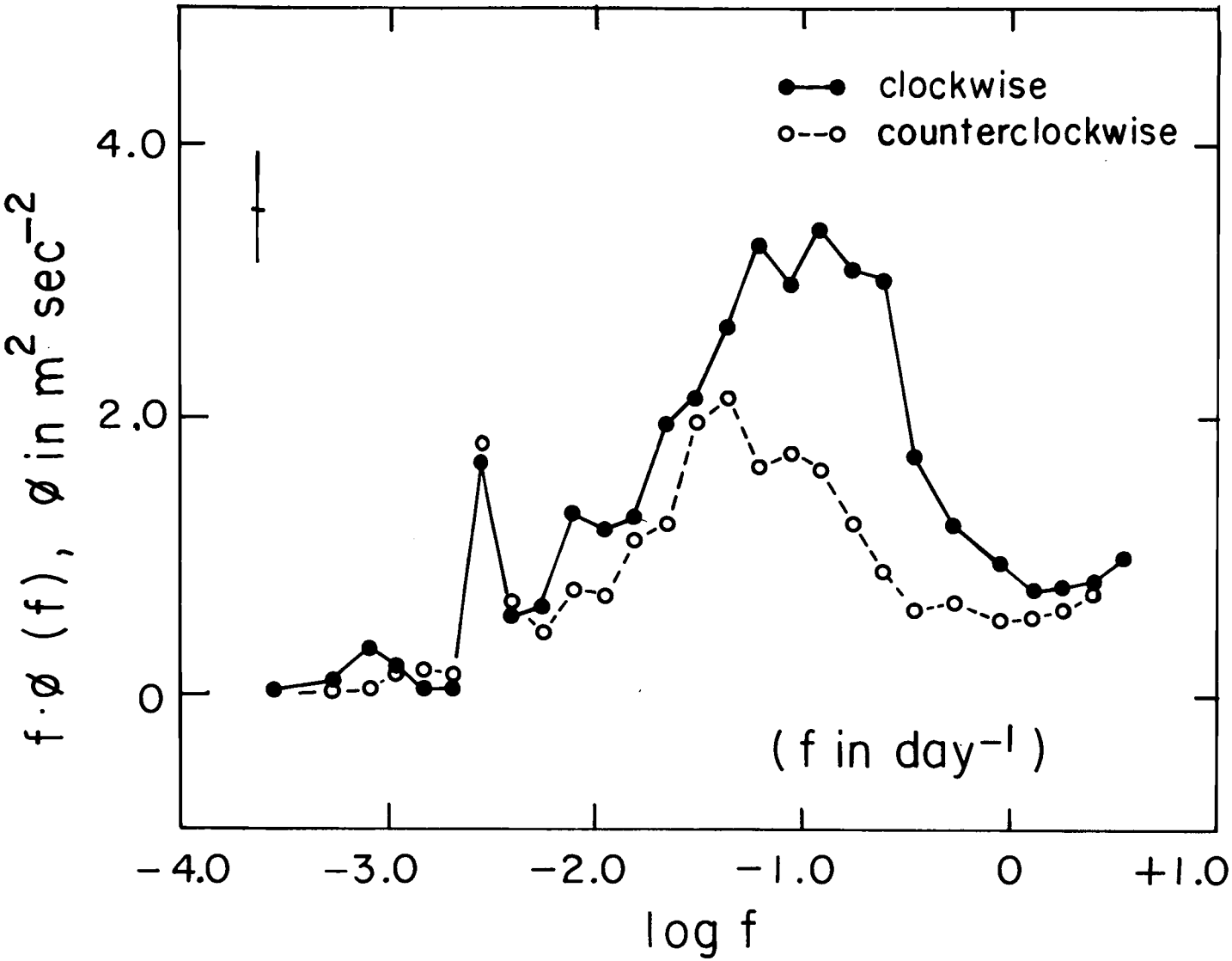

Figure 3.4. A $f \cdot \phi$ vs log f plot of the 10-year composite rotational wind spectrum.

the counterclockwise is a reflection of the clockwise motion of the earth and the eastward-moving synoptic systems, with centers to the North of N, that cause a clockwise rotation of the wind vector. Both clockwise and counterclockwise components are largest in the winter due to the increased synoptic activity during this season. The near equality of the two rotational senses during the summer is a reflection of the prevailing summer synoptic situation which is a slower translation around the general area of N by weak surface pressure highs.

Individual frequencies of the rotary spectrum were investigated in addition to the band averages for the 4-month spectrum. Both the clockwise and counterclockwise components had peaks in the spectral density at the semidiurnal and the diurnal periods. These peaks were larger for the clockwise rotation; also, the diurnal peaks are larger than the semidiurnal peaks.

The seasonal plots (Figure 3.5) reveal that the clockwise component is larger than the counterclockwise component except in summer when they are about equal. Both components are peaked in the synoptic period. Also, the period of the peak is less for the clockwise than the counterclockwise in all seasons except the summer when the periods of the peak are about equal. The peaks of the spectra are largest in the winter and smallest in the summer.

Rotational wind spectra at other locations are not common. However, Pillsbury et al. (1974) have computed rotational wind

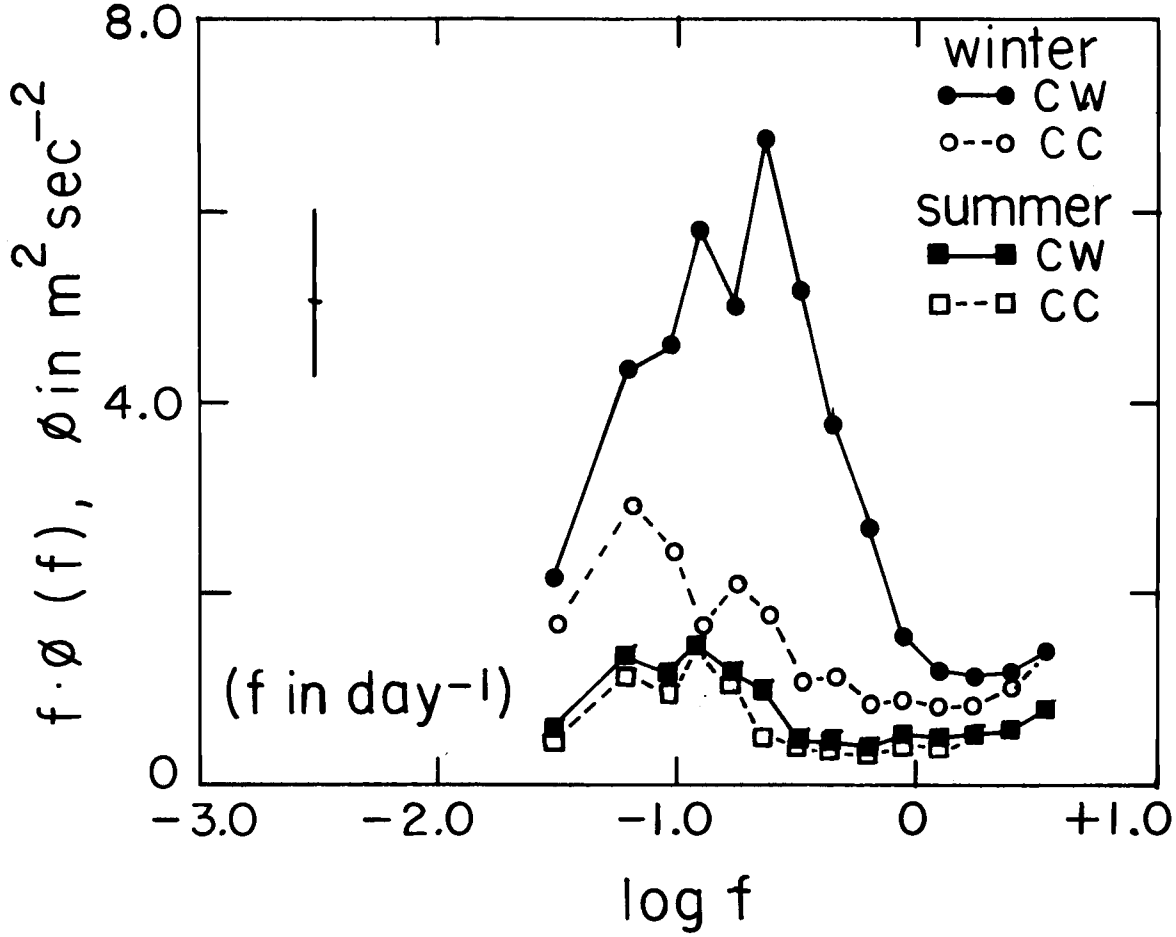

Figure 3.5. A $f \cdot \phi$ vs log f plot of the seasonal rotational wind spectrum.

spectra taken from a meteorological buoy 15 miles off the coast of Newport, Oregon. From a data sample 19 days long, collected in August 1971, they found a semidiurnal peak of 2.9 $m^2/sec^2/CPD$ which is about half the semidiurnal peak in the clockwise component of the rotary spectrum at N.

3.4 Pressure

The general form of the pressure spectrum curves is similar to the wind speed spectrum. The $f \cdot \phi$ vs log f plot (Figure 3.6) of the 10 year pressure spectrum has a peak at a period of 16 days. A spike appears at 126 days in addition to a spike at the annual period. This maximum is related to the appearance of a secondary maximum and minimum in the annual cycle of pressure shown previously. The rate of decrease of energy with frequency increasing from the synoptic peak (16 day period) is much faster for pressure than wind speed. A log ϕ vs log f plot of the pressure spectrum is shown in Figure 3.7. The spectral values increase from the shortest period up to the annual period. As with the wind speed, spectral values fluctuate at the longest periods, but these fluctuations have little statistical significance. There is a sharp peak at a period of 12 hours, reflecting the semidiurnal pressure fluctuation referred to previously.

The winter and summer seasonal spectra of pressure in the form of $f \cdot \phi$ log f is shown in Figure 3.8. The winter pressure

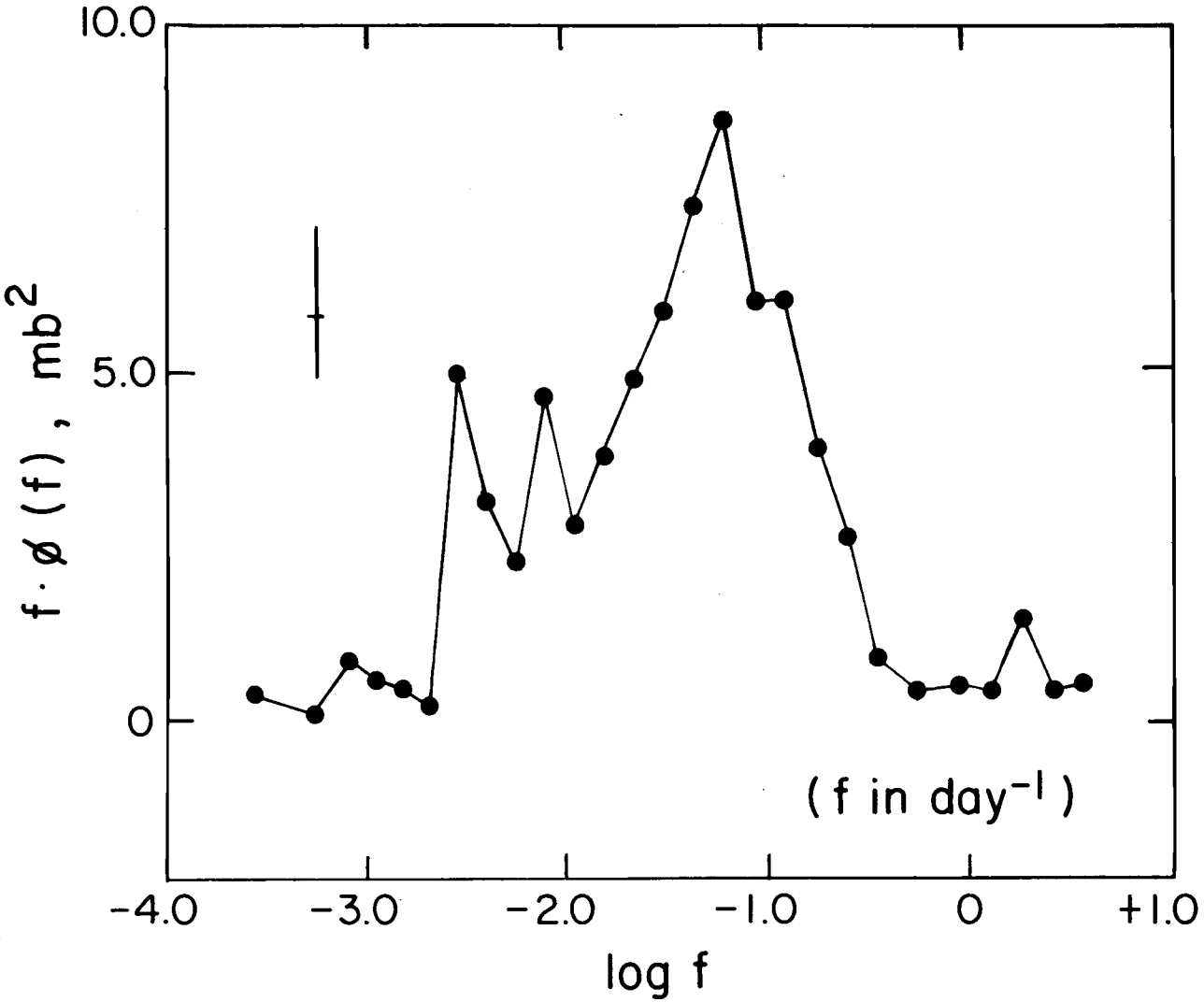

Figure 3.6. A $f \cdot \phi$ vs log f plot of the 10-year composite pressure spectrum.

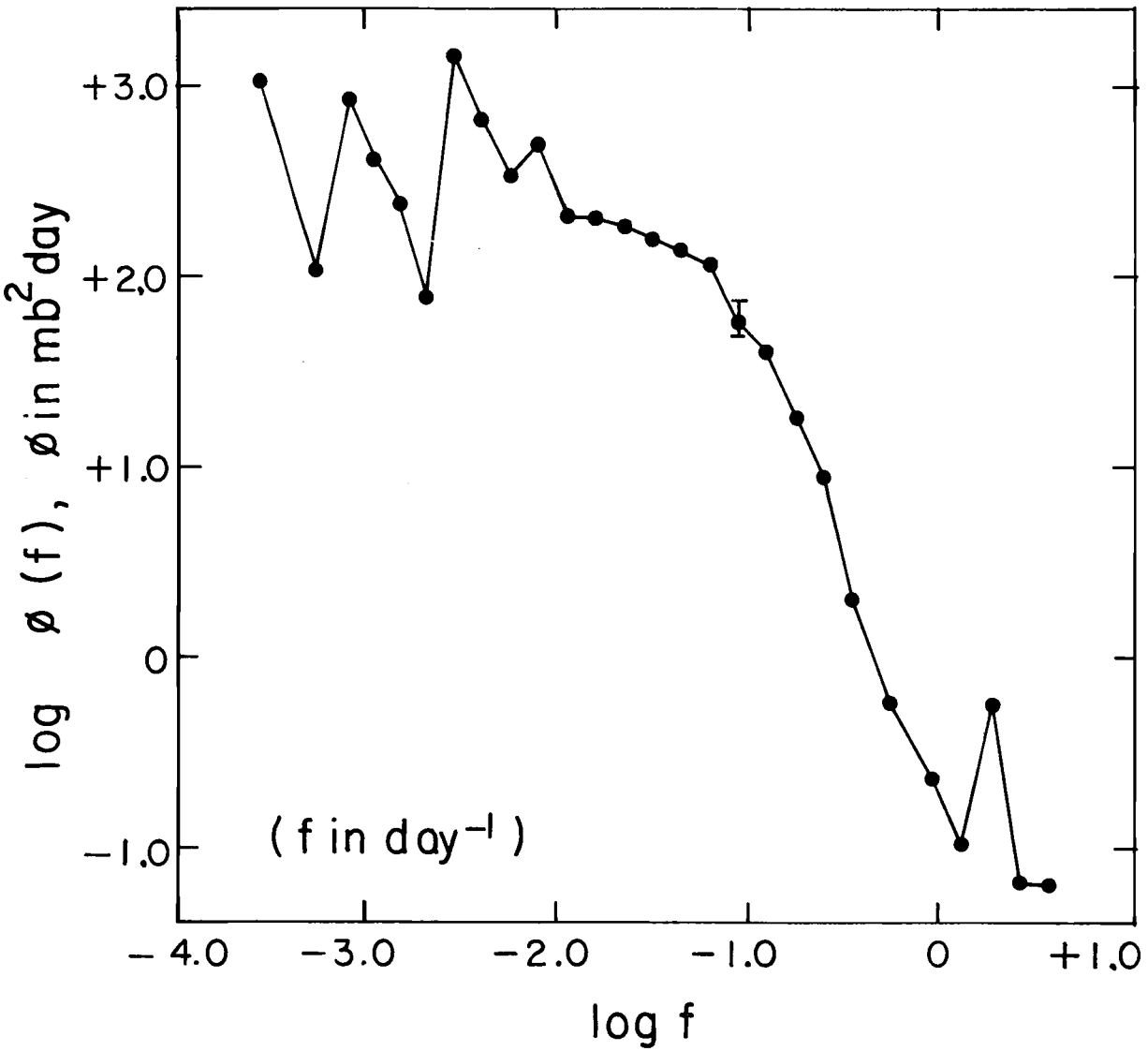

Figure 3.7. A log ϕ vs log f plot of the 10-year composite pressure spectrum.

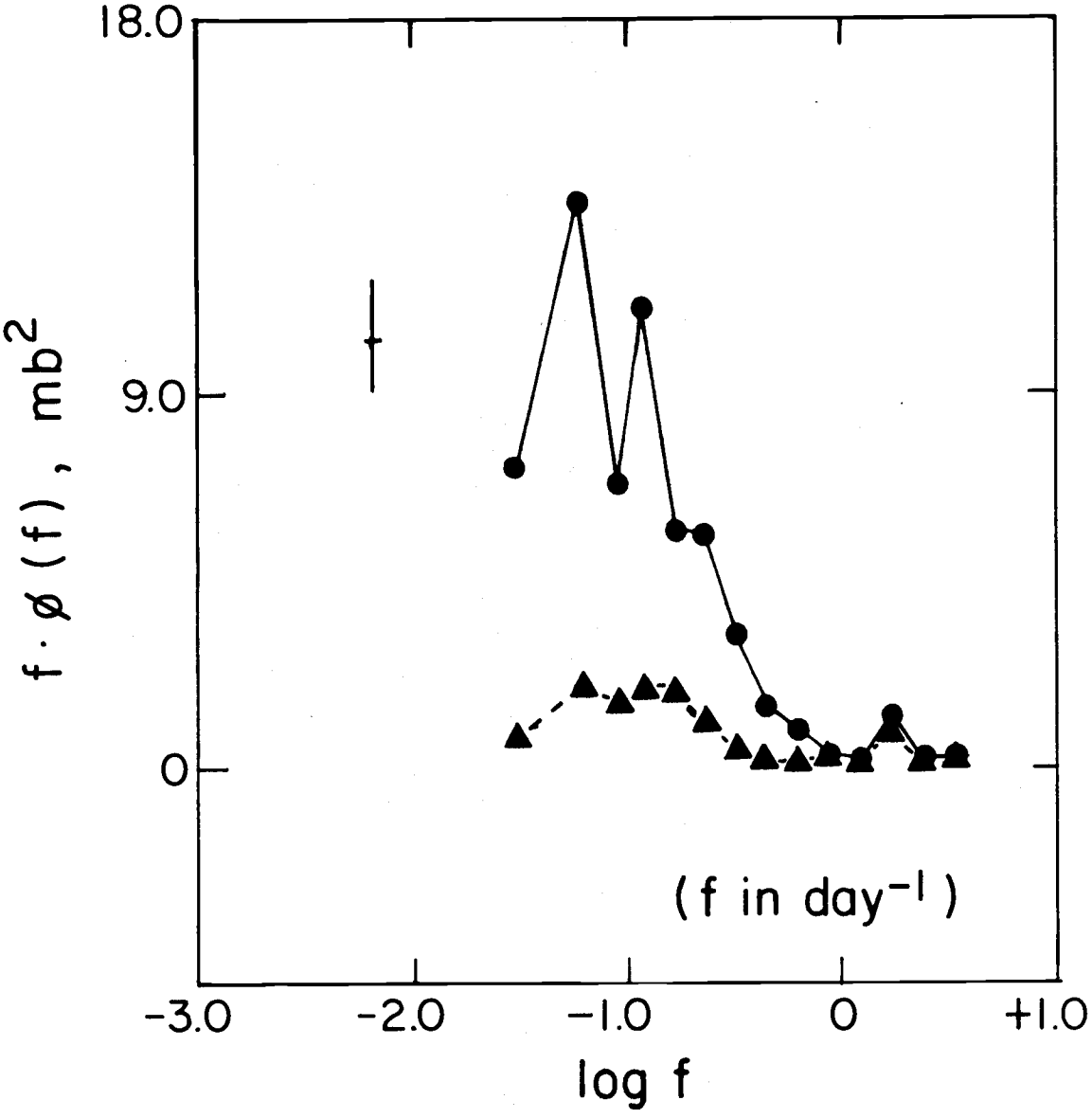

Figure 3.8. A $f \cdot \phi$ vs log f plot of the seasonal pressure spectrum (circles are the winter spectra and the triangles are the summer spectra).

spectrum has a peak at 15.9 days. The spring and fall have similar spectra (not shown) with a peak at 10.6 days of similar magnitude. The summer seasonal pressure spectrum has a broad peak with a maximum at 18.9 days but is only 1/10 the magnitude of the winter maximum or 1/5 that of the spring and fall seasonal pressure maximum. All seasons have a spike at the semidiurnal period.

The spectra unaveraged over frequency bands (not shown) show spikes at the semidiurnal and diurnal periods. The energy at the diurnal period is an order of magnitude larger than that of the surrounding periods while the semidiurnal energy is two orders of magnitude larger than the energy of the surrounding periods.

Pressure spectra for the Pacific are not common. However, Roden (1963) calculated pressure spectra for Wake Island and Honolulu, Hawaii. Roden found an annual peak at both stations of 3.6×10^2 mb^2/CPD, which is about 1/3 the value at N. The difference between the southerly stations and N is reasonable, since N experiences seasonal synoptic patterns and the others do not.

The Byshev and Ivanov study (1969), mentioned in the wind speed section, included pressure spectra in the Atlantic. Byshev and Ivanov found that the pressure energy peak in the $f \cdot \phi$ vs log f plot was in the synoptic range with 6.4 days period for all zones. While the energy peak of the 40-60N zone was about 8 mb^2, the 30N-30S zone energy peak was about .08 mb^2. In addition, there were energy peaks

in the 30N-30S zone of 2.1 and .5 days. N had a pressure energy peak of .9 mb^2 at the semidiurnal period. In addition, N also had a peak at the diurnal period. The pressure spectrum at N is most similar to that of the Northern zone of the Byshev and Ivanov study.

Another study was done on long-period variations in the seasonal sea-level pressure over the Northern Hemisphere by Wagner (1971). He found relative pressure peaks in the period range of 26 to 28 months. Much of the same thing occurred at N, where an examination of the N data shows a minor but prominent peak in the pressure energy near the period of 29 months.

3.5 Sea Surface Temperature

A plot of the sea surface temperature spectrum in the form of $\log \phi$ vs $\log f$ is shown in Figure 3.9. There is a sharp peak at the annual period, with comparatively little energy elsewhere. This is in contrast to the wind speed and pressure spectra which have comparable energy in the synoptic and annual periods. A plateau appears at periods of about one to four days which may be associated with synoptic scale weather systems.

The seasonal spectra of the sea temperature plotted as $f \cdot \phi$ vs $\log f$ in Figure 3.10 are remarkably different from each other. The summer sea temperature spectrum has a general minimum at the intermediate periods with the largest diurnal peak of any

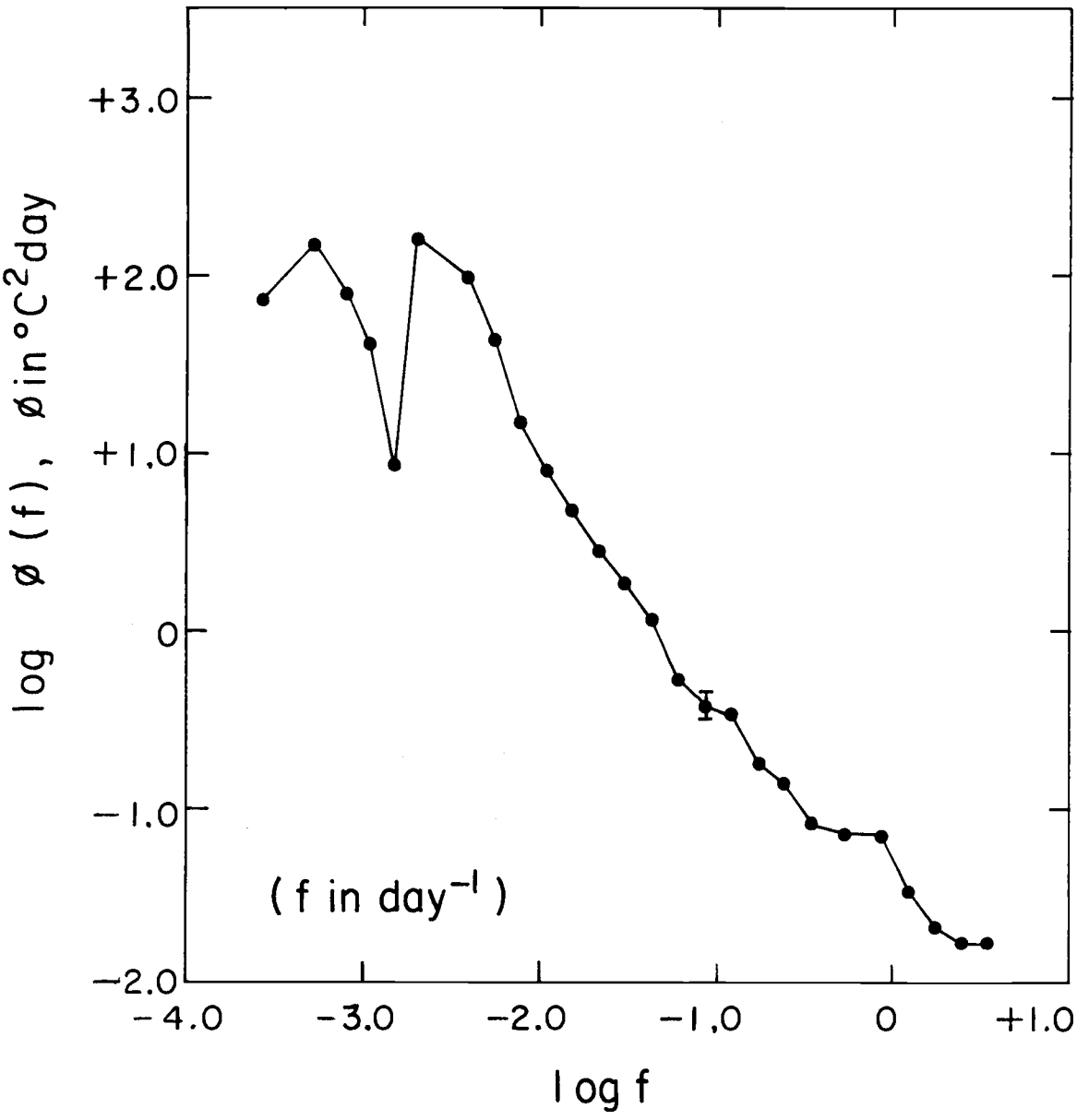

Figure 3.9. A log ϕ vs log f plot of the 10-year composite sea temperature spectrum.

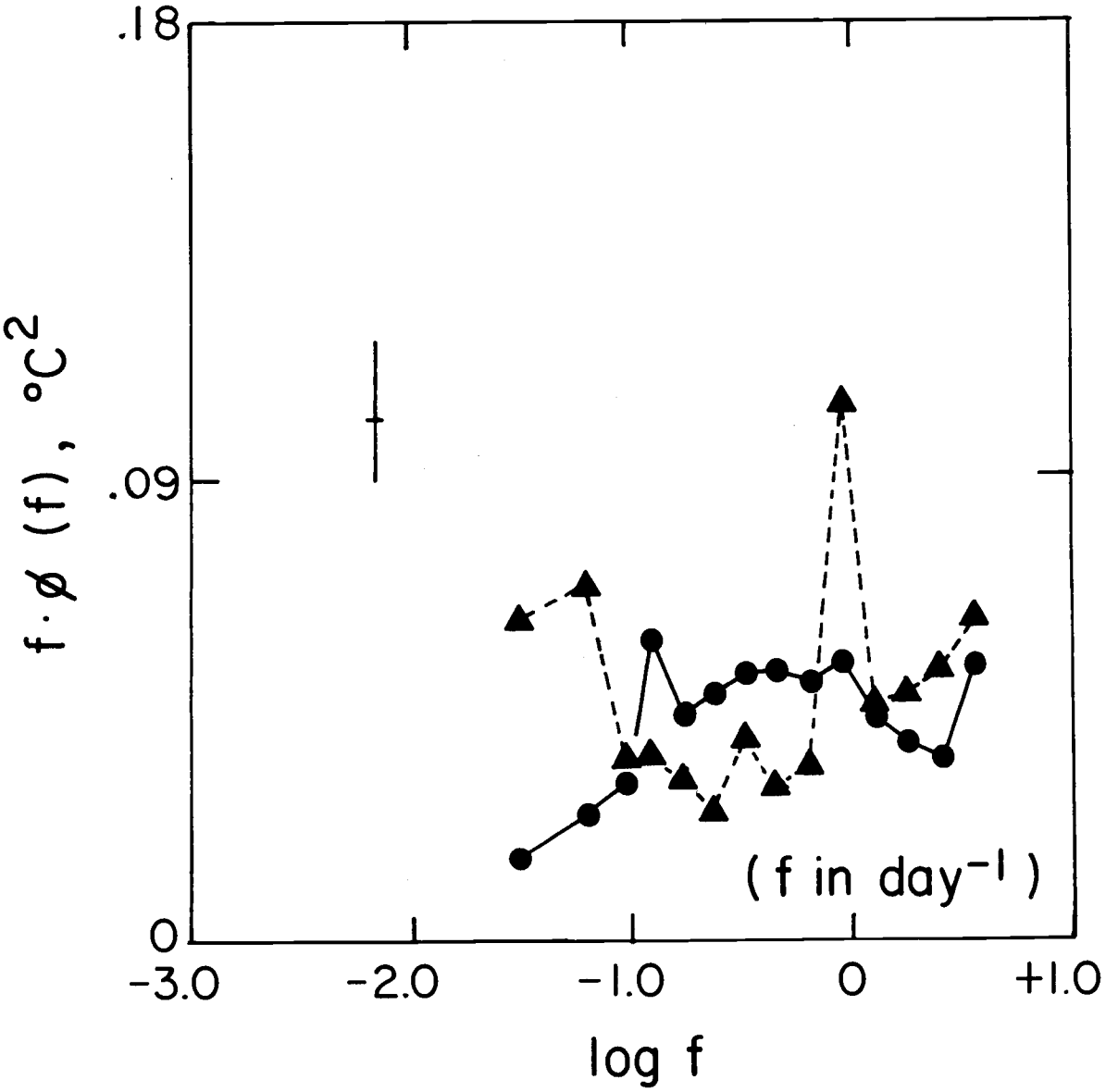

Figure 3.10. A $f \cdot \phi$ vs log f plot of the seasonal sea temperature (circles are the winter spectra and the triangles are the summer spectra).

of the seasons, a reflection of greater solar insolation and a shallow mixed layer. The winter seasonal spectrum has a plateau from 1 to 6 days with a distinctive spike at 8.0 days and a diurnal peak very much smaller than that for summer.

The sea temperature spectra can be compared to spectra at other locations. Lee and Cox (1966) constructed sea surface spectra for a station near 30N 120W. On a short term series taken during December and January, they found no diurnal peak and only a semi-diurnal peak at the surface of 1.2 $°C^2$/CPD. This is about one order of magnitude less than the semidiurnal spectral density of the sea surface temperature spectra at N which also has an even larger diurnal peak. The spectral density of the annual peak at 30N 120W was about 1.6×10^3 $°C^2$/CPD, or 1/3 less than the annual peak at N.

Roden (1963) found smaller annual peaks of the sea temperature spectral density at two Pacific Island stations. The annual spectral density of the sea temperature at Honolulu was about 3.6×10^2 $°C^2$/CPD and the annual spectral density of the sea temperature at Wake was about 1.5×10^2 $°C^2$/CPD, or an order of magnitude less than at N. This is to be expected since Honolulu and Wake are more in the tropics where annual variations are less than those of higher latitudes.

3.6 Air Temperature

The air temperature spectrum is similar in shape to the sea surface temperature spectrum as Figure 3.11, a plot of log ϕ vs log f, shows. There is a dramatic spike at the annual period. There is also a spike at the diurnal cycle. There is no evidence of a peak at synoptic periods, indicating that air temperature is largely controlled by sea surface temperature.

The seasonal power spectra of the air temperature are shown in Figure 3.12. The seasonal spectra of the air temperature have a spike at the diurnal period, which has the largest value in the summer and the smallest in the winter. The summer power spectrum is rather uniform for periods greater than a day while the other seasons (winter shown only) are distinctly peaked between 5.8 and 10.6 days.

When the air temperature spectra are considered without averaging over frequency bands, the spectra reveal that the spectral density at the diurnal period has a spike that is more than an order of magnitude larger than energy at the surrounding frequencies.

We can compare the N spectra with Roden's (1963) island data. The air temperature spectral density annual peak at Wake and Honolulu is about 3.6×10^{2} $^{\circ}C^{2}$/CPD, or about 1/10 that at N. The variation of the air temperature at the tropical Pacific island stations should be greatly modulated by the sea temperature variations which, as pointed

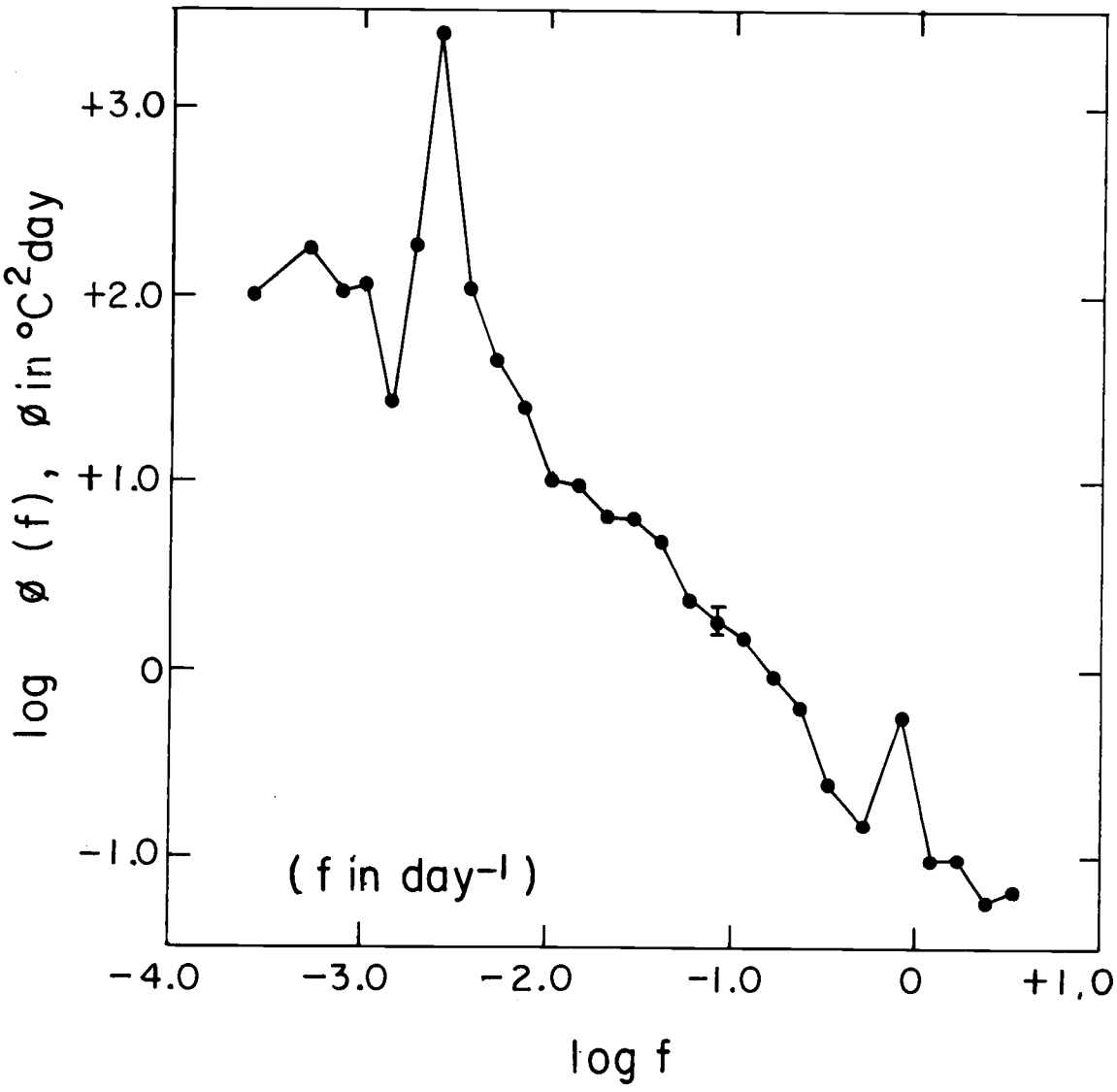

Figure 3.11. A log ϕ vs log f plot of the 10-year composite air temperature spectrum.

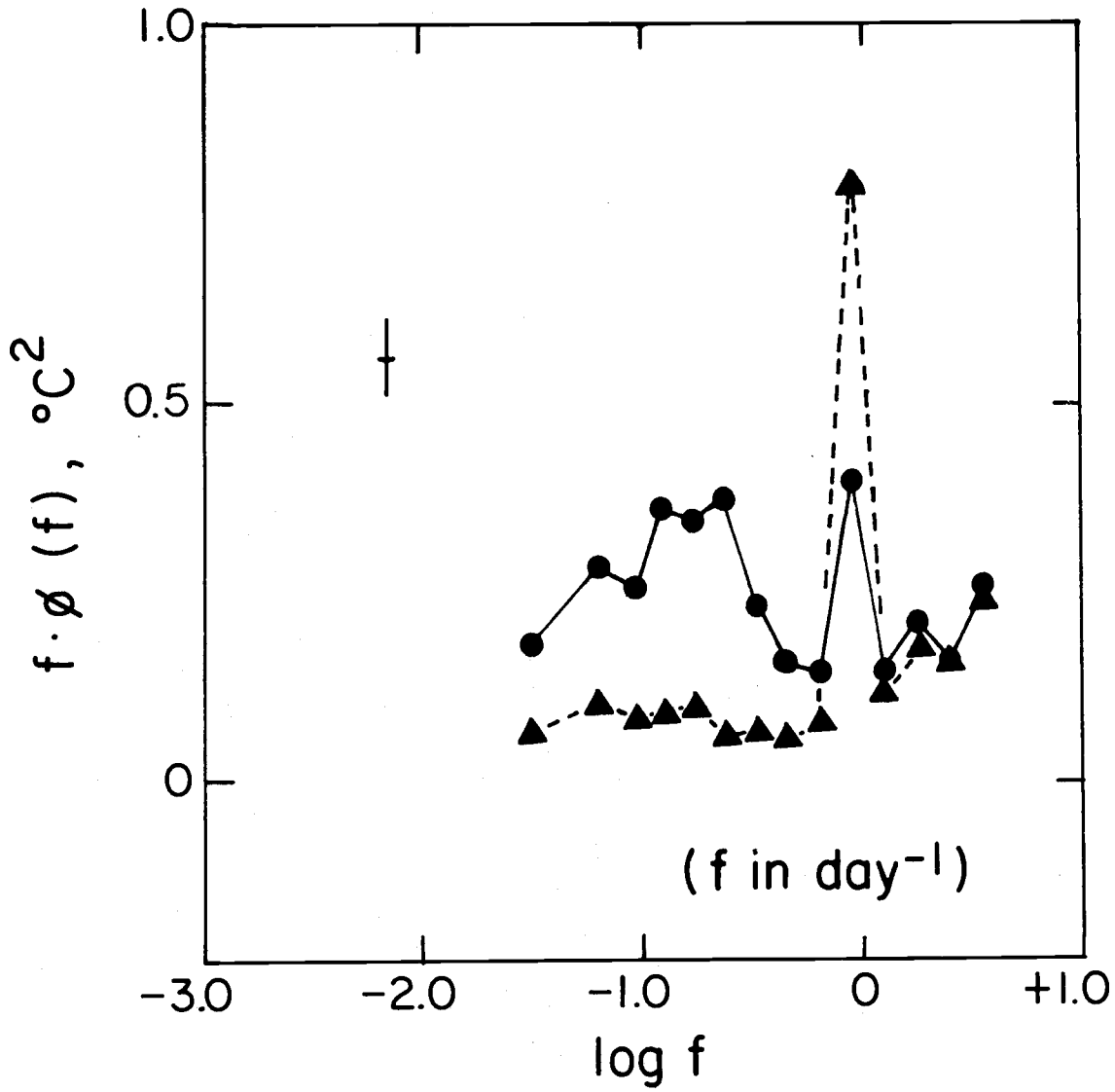

Figure 3.12. A $f \cdot \phi$ vs log f plot of the seasonal air temperature spectra (circles are the winter spectra and the triangles are the summer spectra).

out in the sea temperature section, were also about 1/10 that at N.

The Byshev and Ivanov Atlantic spectral analysis (1969) also included air temperature. Byshev and Ivanov found a seasonal peak in the energy of the air temperature of .7 $°C^2$ in the North Atlantic zone between 40N-60N. However, they found no seasonal peak of the energy of the air temperature in the 30N-30S zone. The maximal energy peak of the air temperature at N is seasonal, but the value is .8 $°C^2$. Clearly, N at 30N is under at least some synoptic influence and is more like the 40N-60N Atlantic zone.

3.7 Dew Point

The dew point spectrum has more structure than the air or sea temperature spectra as shown in Figure 3.13. Like the air and sea temperature spectra but the dew point has maximal energy in a dramatic peak associated with the annual period. There is a small maximum or a plateau at a period of about 80 days which is similar to the air temperature spectrum but more pronounced. There is a change in slope in the dew point spectrum at a period of 122 days. The increase in energy at the shortest period may be due to aliasing.

The spectrum of the seasonal dew point spectra as plots of $f \cdot \phi$ vs log f is shown in Figure 3.14. The winter spectrum is most sharply peaked while the summer spectrum is almost flat. All seasons have a maximum around 5.8 days.

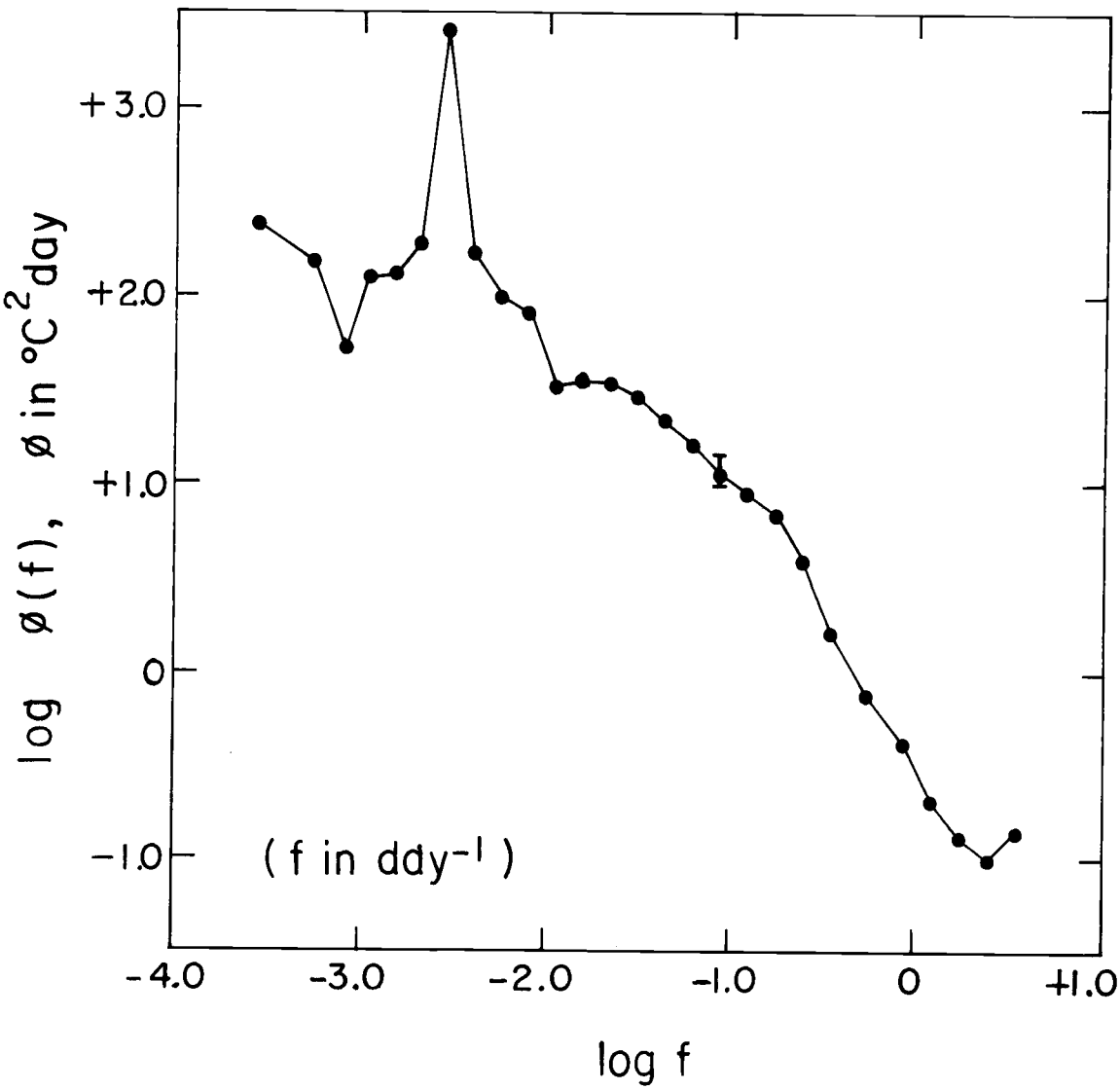

Figure 3.13. A log ϕ vs log f plot of the 10-year composite dew point spectrum.

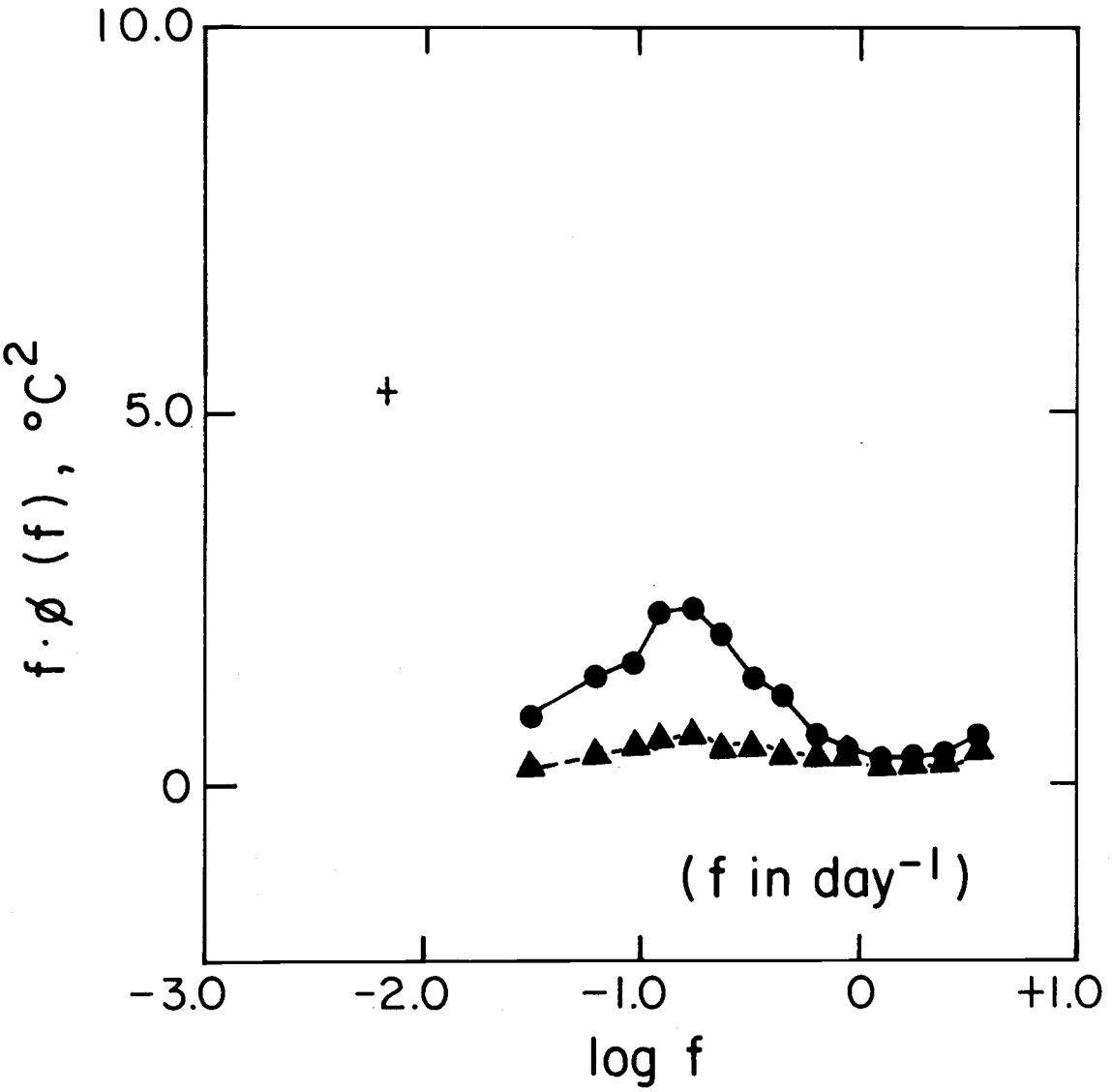

Figure 3.14. A $f \cdot \phi$ vs log f plot of the seasonal dew point spectrum (circles are the winter spectra and the triangles are the summer spectra).

Examination of the spectra without band averaging shows a spike at the diurnal period that is about an order of magnitude larger than the surrounding frequencies. Energy at the semidiurnal period has a prominent but smaller spike than the diurnal period.

3.8 Summary of Spectra

Meteorological spectra were calculated for N at 30N 140W. The variables investigated were wind speed, surface air pressure, sea temperature, air temperature, and dew point. Spectra were computed for periods ranging from 6 hours to 10 years.

For all variables, significant peaks of energy were observed at the annual, diurnal, and semidiurnal periods. Also, all variables had the largest variance in winter and the smallest variance in the summer, except for sea temperature which had the largest variance in the spring and the smallest variance in the winter. The maximum spectral density of all variables was associated with the annual period. The spectral densities of all of the variables generally decreased from the annual period to the shortest period. Furthermore, the spectra are similar to those found by other investigators at approximately the same latitude.

4. THE MIXED LAYER DYNAMICS

Now that a descriptive background has been constructed for N, we are able to investigate some details of mixed layer dynamics at the station. As was mentioned in the introduction, there are several mixed layer models that could be used. However, we are limited in testing models because the mixed layer at N is measured by only a few mechanical BTs a day and much less frequent bottle casts. There are no direct current measurements. Therefore, Denman's (1972) model must be used since it requires no current measurements and is responsive to time scales of the order of a day. Before actually applying Denman's model to data from N, we describe the Denman model itself in detail.

4.1 Denman's Model

This model can be broken down into two regimes, the first of which is the deepening or wind-dominated regime. For this deepening regime, Denman's (1972) model is described by three equations. They are:

$$(4\text{-}1) \qquad \frac{dT_s}{dt} = \frac{2}{\rho_0 h}\left[-\frac{(G-D)}{\alpha g} + \frac{h}{c_p}(B+He+Hs) + \frac{R}{c_p}(h-\gamma+\gamma^{-1}e^{-\gamma h})\right]$$

(4-2)

$$H[w+\frac{dh}{dt}] = \frac{2[\frac{1}{ag}(G-D)+\frac{R\gamma^{-1}}{c_p}(1-e^{-\gamma h})]-\frac{h}{c_p}[B+He+Hs+R(1+e^{-\gamma h})]}{\rho_0 h(T_s-T_{-h})}$$

(4-3)

$$\frac{dT_{-h}}{dt} = \frac{\gamma R e^{-\gamma h}}{\rho_0 c_p} - (w+\frac{dh}{dt})\frac{\partial T}{\partial z}\Big|_{-h}$$

boundary equation:

(4-4)

$$\frac{\partial T(z)}{\partial t} = \frac{\gamma R e^{\gamma z}}{\rho_0 c_p} - w\frac{\partial T(z)}{\partial z}$$

For the Equations (4-1) to (4-4), the following symbols are used.

T_s = temperature of the mixed layer.

T_{-h} = temperature of the water just below the mixed layer.

T = water temperature at a point.

w = large scale upwelling.

h = mixed layer depth.

ρ_0 = average density of the sea water.

c_p = heat capacity of the sea water.

G = wind energy.

D = dissipation.

B = back radiation.

He = latent heat flux.

Hs = sensible heat flux.

R = solar radiation.

α = coefficient of thermal expansion.

g = acceleration of gravity.

γ = an average extinction coefficient for sunlight.

t = time

$H[w+\frac{dh}{dt}]$ is the Heaviside step function which is

$$H = \begin{cases} 0 & \text{if } [w+\frac{dh}{dt}] \geq 0 \quad \text{no entrainment mixing.} \\ 1 & \text{if } [w+\frac{dh}{dt}] < 0 \quad \text{entrainment mixing.} \end{cases}$$

The equations of the mixed layer itself are expressed by (4-1) and (4-2). The dependent variables are T_s, the temperature of the surface layer and h, the mixed layer depth. The empirically derived, independent variables that drive the model are: the surface heat fluxes of the back radiation (B); latent heat (He) and sensible (Hs) heat, the penetrative solar radiation (R); and the wind energy available for turbulent mixing (G-D). The factors ρ_0, g, c are constants. The extinction length of light energy, γ^{-1}, is a "floating" constant with a limited range of values though fixed for a particular case. A hidden floating parameter is the assumption of the partition of wind energy, or the actual amount of turbulent-energy production in the mixed layer by wind action.

Equation (4-3) expresses the temperature change below the

mixed layer. The temperature change depends only on the fraction of solar radiation that escapes the mixed layer (if w is negligible). Equation (4-4) expresses the temperature of the water just below the mixed layer. The temperature of the water, during small time steps, depends mostly on the rate of descent (in the case of descending mixed layer depths).

The Equations (4-1) to (4-4) are solved numerically with small time steps (about 60 seconds) by the Runge-Kutta technique.

For the second case in Denman's model, the heat regime or decreased mixed layer depth, then $H = 0$ and the Equations (4-1) to (4-4) can be rearranged to

$$(4\text{-}5) \qquad \frac{1}{\alpha g}(G-D) + \frac{R\gamma^{-1}}{c_p}(1-e^{-\gamma h}) = \frac{1}{2}\frac{h}{c_p}[R(1+e^{-\gamma h})+B+He+Hs]$$

$$(4\text{-}6) \qquad \Delta T_s = \frac{1}{h\rho_0 c_p}[R(1-e^{-\gamma h})+B+He+Hs]\Delta t$$

In Equation (4-5) h, the mixed layer depth, is the only variable once the driving fluxes (B, He, Hs, R, G-D) have been specified for a particular time step. The Equation (4-5) is solved by Newton's method for time steps of about 60 minutes. Once h has been determined from (4-5) for a particular time step, (4-5) is used in (4-6) to find the temperature change of the mixed layer T_s for that same time step.

Basically, the model is driven by hourly fluxes of latent heat, sensible heat, back radiation, solar radiation and wind-turbulent energy computed from hourly meteorological observations. With the start of each hour the wind regime is calculated through one time step to check for a descending mixed layer. If the mixed layer depth is not increasing, then the equations for the heat regime are used.

Let us cite a couple of examples to demonstrate how this model works. Suppose that the mixed layer depth is at equilibrium, since the heat flux and wind speed have not changed for a long time. Then, when either the wind speed is increased or the surface heat flux is decreased in a step fashion to a new constant value, the mixed layer will be out of equilibrium. At that time, the wind-turbulent energy works against buoyancy forces by entraining colder water from below (Equation 4-1 to 4-2). Deepening will continue until a new equilibrium depth is reached. At equilibrium depth, the wind-turbulent energy will just equal that energy needed to redistribute all of the heat buoyancy throughout the mixed layer. Equations (4-5) to (4-6) will apply now.

Suppose that again the mixed layer is at equilibrium for a long time. Then, the heat flux is increased, or the wind speed is decreased, in a step-like way. The mixed layer will instantaneously reform at a decreased mixed layer depth. The actual depth is determined by Equation (4-5). At this depth, all of the wind turbulent energy is required to redistribute all of the heat flux throughout the

layer. These examples point out that the mixed layer depth, determined from Denman's model, is dependent upon a balance between wind energy and heat flux.

4.2 The Effect of Salinity on Mixed Layer Dynamics

In Denman's model, the only variable affecting the density and buoyancy is temperature. However, in the subtropics, where N is located, evaporation exceeds precipitation. The question then arises: does salinity have a significant effect on mixed layer dynamics at N? In other words, can Denman's model be applied to the data from N? In order to answer this question, a mixed layer model like Denman's is derived which includes the effect of salinity on the mixed layer. A method of development quite similar to Denman's (1972) is used.

The assumptions here are the same as those in Denman (1972) with the exception that density is also a function of salinity. Basically, the assumptions are that the sea is an incompressible, stably stratified, horizontally homogeneous fluid that obeys the Boussinesq approximation. Wave dynamics effects such as internal, inertial, and Rossby waves are ignored. The mixed layer is assumed to be homogeneous. The submixed layer waters are assumed laminar and non-turbulent. It is also assumed that any property introduced into the layer is instantaneously distributed throughout the layer.

Conservation of Mass, Heat and Salinity

The equation of state for sea water is

$$\frac{dT}{dt} = \frac{\partial T}{\partial \rho}\frac{\partial \rho}{\partial t} + \frac{\partial T}{\partial s}\frac{\partial S}{\partial t} + \frac{\partial T}{\partial \xi}\frac{\partial \xi}{\partial t} \tag{4-7}$$

where T is the temperature, S is the salinity, ρ is the density and ξ is the entropy per unit mass defined such that

$$\rho \frac{\partial \xi}{\partial t} \cong \frac{Q_T}{T_A} .$$

Here Q_T is a heat source term and T_A is the absolute temperature. The specific heat at constant volume is $c_v = T_A(\frac{\partial \xi}{\partial T})_p$. In the upper layer $c_v = c_p$, the specific heat of sea water at constant pressure.

The conservation of mass for an incompressible fluid is $\frac{dP}{dt} = 0$. Also, $\frac{\partial T}{\partial S} \approx 0$, so (4-7) can be written as

$$\frac{dT}{dt} = \frac{Q_T}{\rho_0 c_p}$$

Suppose that the absorption of solar radiation can be represented by a single extinction coefficient γ; then the heat source term is

$$\frac{Q}{\rho_0 c_p} = \frac{\gamma R e^{\gamma z}}{\rho_0 c_p}$$

where R is the solar radiation falling on the sea surface. Substituting the expression for Q_T in the turbulent form of (4-7) gives the following form of the heat conservation equation

$$\frac{\partial T}{\partial t} + w\frac{\partial T}{\partial z} + \frac{\partial}{\partial z}(\overline{w'T'}) = \frac{\gamma R e^{\gamma z}}{\rho_0 c_p} \tag{4-8}$$

The turbulent form of the salt conservation equation is just

$$\frac{\partial S}{\partial t} + w\frac{\partial S}{\partial z} + \frac{\partial}{\partial z}(\overline{w's'}) = 0 \tag{4-9}$$

In these equations ρ_0 is the average density and the prime represents a fluctuating component.

Conservation of Mechanical Energy

The turbulent mechanical energy equation as derived by Phillips (1966) is

$$\frac{\partial}{\partial t}\left(\frac{c^2}{2}\right) = -\overline{u'w'}\frac{\partial u}{\partial z} - \frac{\partial}{\partial z}\left[w'\left(\frac{P'}{\rho_0} + \frac{c^2}{2}\right)\right] - \frac{\overline{w'\rho'}}{\rho_0}g - \epsilon \tag{4-10}$$

where $c^2 = u'^2 + v'^2 + w'^2$, ϵ is the rate of dissipation of turbulent energy, g is the acceleration of gravity, p' is the pressure fluctuation and ρ' is the density fluctuation.

Based upon dimensional arguments, Denman (1972) shows that

$$\frac{\partial}{\partial t}\left(\frac{c^2}{2}\right) \ll \epsilon ,$$

or, the local rate of change of the turbulence kenetic energy per unit mass is negligible compared to the dissipation of kinetic energy.

Now, the density is a function of salinity and temperature, so

$$d\rho = \alpha_T \rho_0 dT + \alpha_S \rho_0 dS$$

where

$$\alpha_T = \frac{1}{\rho_0}\left(\frac{\partial \rho}{\partial T}\right)_S \quad \text{and} \quad \alpha_S = \frac{1}{\rho}\left(\frac{\partial \rho}{\partial S}\right)_T$$

are the coefficients of expansion for temperature and salinity. Thus, (4-10) becomes

$$(4\text{-}11) \qquad -\overline{u'w'}\frac{\partial U}{\partial z} - \frac{\partial}{\partial z}\left[w'\left(\frac{P'}{\rho_0} + \frac{c^2}{2}\right)\right] = \alpha_T g\overline{w'T'} + \alpha_S g\overline{w'S'} + \epsilon ,$$

which is a simplified form of the mechanical energy equation.

Mixing Entrainment

According to Kraus and Turner (1967) $\overline{w'T'}(-h)$, the mixing term at the bottom of the layer, may be expressed as

$$(4\text{-}12) \qquad \overline{w'T'}(-h) = H(-w_m)(T_s - T_{-h})$$

where T_s = temperature of the mixed layer, T_{-h} is the

temperature immediately below the layer, $-w_m$ is the entrainment velocity, H is the Heaviside step function having the properties

$$H = \begin{cases} 0 & \text{if } -w_m \leq 0 \quad \text{no entrainment mixing} \\ 1 & \text{if } -w_m > 0 \quad \text{entrainment mixing at } z = -h \end{cases}$$

The entrainment velocity can be written as $-w_m = w + \frac{dh}{dt}$ where w is the mean vertical advective velocity immediately below the mixed layer. w is determined predominantly by the local curl of the wind stress and is usually small in the open oceans. Equation (4-12), the mixing entrainment for heat, becomes

$$\overline{w'T'(-h)} = -H(w+\frac{dh}{dt})(T_s - T_{-h}) \quad (4\text{-}13)$$

In a similar manner, the mixing entrainment for the salinity is

$$\overline{w'S'(-h)} = -H(w+\frac{dh}{dt})(S_s - S_{-n}) \quad (4\text{-}14)$$

Turbulent Fluxes

At the lower boundary, the mixing entrainment of heat is $\overline{w'T'}(-h)$. At the upper boundary $\overline{w'T'}(0) = F$, where $F = He + Hs + B$; the sum of the latent heat flux, sensible heat flux and back radiation.

We are assuming that the heat inputs are instantaneously distributed uniformly through the layer by the turbulent diffusion of $\overline{w'T'}$. The equations for $\partial T_s/\partial t$ and $\overline{w'T'}$ eliminate the z dependence of the heat equation and match the boundary equations. The equation for the temperature change of the mixed layer $\partial T_s/\partial t$ is,

$$(4\text{-}15) \qquad \frac{\partial T_s}{\partial t} = \left[-H\left(w+\frac{dh}{dt}\right)(T_s - T_{-h}) + \frac{F}{\rho_0 c_p} + \frac{R}{\rho_0 c_p}(1-e^{-\gamma h})\right]\frac{1}{h} \ .$$

The equation for the turbulent heat flux $\overline{w'T'}$ is,

$$(4\text{-}16) \qquad \overline{w'T'}(z) = \left[H\left(w+\frac{dh}{dt}\right)(T_s - T_{-h}) - \frac{F}{\rho_0 c_p} - \frac{R}{\rho_0 c_p}(1-e^{-\gamma h})\right]\frac{z}{h}$$

$$+ \frac{1}{\rho_0 c_p}\left[-R(1-e^{\gamma z}) - F\right] \qquad \text{for } (-h \leq z \leq 0) \ .$$

Similarly for salt the mixing entrainment at the lower boundary is $\overline{w'S'}(-h)$. At the upper boundary, the salt flux, $\overline{w'S'}(0) = -E$ where

$$E = \frac{He \cdot S_s}{L} - P_r$$

and L = latent heat of evaporation, S_s is the salinity of the surface layer and P_r is the precipitation. The comparable equations of (4-15) and (4-16) for the change of salinity of the mixed layer and the

turbulent flux of salt are

$$\frac{\partial S_s}{\partial t} = \left[-H(w+\frac{dh}{dt})(S_s - S_{-h}) + E\right]\frac{1}{h} \tag{4-17}$$

$$\overline{w'S'}(z) = \left[H(w+\frac{dh}{dt})(S_s - S_{-h}) - E\right]\frac{z}{h} - E\ . \tag{4-18}$$

The Bottom Boundary Condition

The temperature below the mixed layer (assuming no turbulent energy penetrates below $z = -h$) is

$$\frac{\partial}{\partial t}T(z) = \frac{\gamma R e^{\gamma z}}{\rho_0 c_p} - w\frac{\partial T}{\partial z}(z)$$

At the interface, the temperature is given by

$$\frac{dT(-h)}{dt} = \frac{\gamma R e^{-\gamma h}}{\rho_0 c_p} - \{w+\frac{dh}{dt}\}\frac{\partial T}{\partial z}\Big|_{-h} \tag{4-19}$$

Thus, the temperature of the water just below the mixed layer depends upon the small fraction of solar radius that is available at that depth for absorption and the advection of the mixed layer down the submixed layer temperature field. For salt, the change below the mixed layer is given by

$$\frac{\partial S(z)}{\partial t} = -w\frac{\partial S(z)}{\partial z}\ .$$

At the interface, the salinity is given by

$$\frac{dS(-h)}{dt} = -\{w+\frac{dh}{dt}\}\frac{dS}{dz}\Big|_{-h} \quad . \tag{4-20}$$

The salinity of the water just below the mixed layer depends only upon the advection of the mixed layer down the salinity field.

Integration Over the Layer

The conservation equation of heat, salt and mechanical energy will now be integrated vertically over the mixed layer. The heat Equation (4-8) becomes

$$h\frac{\partial T_s}{\partial t} + H(w+\frac{dh}{dt})(T_s - T_{-h}) = [F+R(1-e^{-\gamma h})]\frac{1}{\rho_0 c_p} \quad . \tag{4-21}$$

The integrated salt equation from (4-9) becomes

$$h\frac{\partial S_s}{\partial t} + H(w+\frac{dh}{dt})(S_s - S_{-h}) = E \quad . \tag{4-22}$$

The integration of the mechanical energy Equation (4-11) changes to

$$-\int_{-h}^{0} \overline{u'w'}\frac{\partial u}{\partial z}\,dz - \overline{w'(\frac{P'}{\rho_s} + \frac{c^2}{2})}\Big|_{z=0} \tag{4-23}$$

$$= \alpha_T g\int_{-h}^{0} \overline{w'T'}dz + \alpha_S g\int_{-h}^{0} \overline{w'S'}dz + \int_{-h}^{0} \epsilon\,dz \quad .$$

In this case, $w'\{\frac{P'}{\rho_0} + \frac{c^2}{2}\}\Big|_{z=-h}$ is assumed to be zero. The term $\overline{w'T'}$ can be eliminated by the double integral of (4-8) giving

$$(4\text{-}24) \qquad \int_{-h}^{0} w'T'(z)dz = \frac{h^2}{2}\frac{dT}{dt} - \frac{Fh}{\rho_0 c_p} - \frac{R}{\rho_0 c_p}(h-\gamma^{-1}) - \frac{\gamma^{-1}Re^{-\gamma h}}{\rho_0 c_p}$$

The term $\overline{w'S'}$ can be eliminated by the double integral of (4-9) giving

$$(4\text{-}25) \qquad \int_{-h}^{0} \overline{w'S'}(z)dz = \frac{h^2}{2}\frac{dS}{dt} - Eh$$

We shall also make the following substitutions:

$$G = \rho_0 \int_{-h}^{0} \overline{u'w'}\frac{\partial u}{\partial z}\,dz + \rho_0 w'\{\frac{P'}{\rho_0} + \frac{c^2}{2}\}\Big|_{z=0}$$

(the rate of turbulent energy production by wind stress acting at the upper boundary)

$$D = -\rho_0 \int_{-h}^{0} \epsilon\,dz$$

(the total dissipation of energy within the layer), as well as (4-24) and (4-25) into (4-23) and we have

$$(4\text{-}26)\qquad \frac{h^2}{2}\left[\alpha_T \frac{dT_s}{dt} + \alpha_S \frac{dS_s}{dt}\right]$$

$$= -\frac{1}{\rho_0 g}(G-D) + \frac{\alpha_T}{\rho_0 c_p}\left[Fh + R(h-\gamma^{-1}) + \gamma^{-1}Re^{-\gamma h}\right] + \alpha_S[Eh]\ .$$

Equations (4-21) and (4-22) may be used to eliminate dT_s/dt and dS_s/dt from (4-26) giving

$$(4\text{-}27)\qquad -2\left[\frac{1}{\rho_0 g}(G-D) + \frac{\alpha_T}{\rho_0 c_p}\{Fh+R(h-\gamma^{-1}) + \gamma^{-1}Re^{-ah}\} + \alpha_S Eh\right]$$

$$H\left(w+\frac{dh}{dt}\right) = \frac{+\frac{h}{\rho_0 c_p}\left[\alpha_T F + \alpha_T \gamma R(1-e^{-\gamma h})\right] + \alpha_S Eh}{h\left[\alpha_T(T_s - T_{-h}) + \alpha_S(S_s - S_{-h})\right.}$$

To find $\partial S_t/\partial t$ and $\partial T_s/\partial t$ we will use (4-27) in Equations (4-15) and (4-17) respectively.

The equations for the model for the mixed layer model with the salinity effect are

$$(4\text{-}28)\qquad 2\left[\frac{1}{\rho_0 g}(G-D) + \frac{\alpha_T R\gamma^{-1}}{\rho_0 c_p}(1-e^{-\gamma h})\right]$$

$$H\left(w+\frac{dh}{dt}\right) = \frac{-h\left[\frac{\alpha_T}{\rho_0 c_p}(He+Hs+B) + \alpha_S E + \frac{\alpha_T}{\rho_0 c_p}R(1+e^{-\gamma h})\right]}{\left[\alpha_T(T_s - T_{-h}) + \alpha_S(S_s - S_{-h})\right]h}$$

$$(4\text{-}29)\qquad \frac{\partial T_s}{\partial t} = \left[-H\left(w+\frac{dh}{dt}\right)(T_s - T_{-h}) + \frac{1}{\rho_0 c_p}(He+Hs+B) + \frac{R}{\rho_0 c_p}(1-e^{-\gamma h})\right]\frac{1}{h}$$

$$\frac{\partial S_s}{\partial t} = \left[-H\left(w+\frac{dh}{dt}\right)(S_s - S_{-h}) + E\right]\frac{1}{h} \tag{4-30}$$

$$\frac{dT}{dt}(-h) = \frac{\gamma R e^{-\gamma h}}{\rho_0 c_p} - \left\{w+\frac{dh}{dt}\right\}\left.\frac{dT}{dz}\right|_{-h} \tag{4-19}$$

$$\frac{dS}{dt}(-h) = -\left\{w+\frac{dh}{dt}\right\}\left.\frac{dS}{dz}\right|_{-h} \tag{4-20}$$

Equation (4-28) expresses the change of the mixed layer depth; (4-29) expresses the change of the mixed layer temperature; and (4-30) expresses the change of the mixed layer salinity. These three equations are "driven" by the empirical fluxes of heat (He, Hs, B), solar radiation (R), the rate of wind-turbulent energy production (G) as well as the salt flux at the surface ($E = \frac{He \cdot S_s}{4}$ - Precipitation). The interface temperature and salinity are given by (4-19) and (4-20). Both the interface temperature and salinity depend primarily upon the advection of the mixed layer depth over the vertical temperature and salinity fields.

In the absence of entrainment, the Heaviside function H in Equation (4-28) is zero and the equations forming the model rearrange to

$$\frac{1}{\rho_0 g}(G-D) + \frac{\alpha_T R \gamma^{-1}}{\rho_0 c_p}(1-e^{-\gamma h}) \tag{4-31}$$

$$= \frac{h}{2}\left[\frac{\alpha_T}{\rho_0 c_p}(He+Hs+B) + \alpha_S E + \frac{\alpha_T}{\rho_0 c_p} R(1+e^{-\gamma h})\right]$$

$$\frac{\partial T_s}{\partial t} = \frac{1}{\rho_0 c_p} [He+Hs+B+R(1-e^{-\gamma h})] \frac{1}{h} \tag{4-32}$$

$$\frac{\partial S_s}{\partial t} = E \frac{1}{h} \quad . \tag{4-33}$$

Again, Equations (4-19) and (4-20) give $\frac{dT}{dt}(-h)$ and $\frac{dS}{dt}(-h)$.

Equations (4-29) through (4-33) represent the mixed layer model with the effect of salinity on buoyancy included. This model and that in Equations (4-1) through (4-6) are driven by empirically determined values of He, Hs, B, R and G. The main difference between these equations and those of the original model (Equations 4-1 to 4-6) is the inclusion of a third dependent variable, salinity.

The effect of including salinity in the model is to deepen the mixed layer depth and to decrease the mixed layer temperature when applied to the subtropics. A discussion of this follows. In the subtropics $S_s - S_{-h}$ is positive (salinity decreases with depth) and γ_s is positive (increased salinity makes water denser). The denominator of Equation (4-28) is made smaller due to the $\gamma_s(S_s - S_{-h})$ term. Making the denominator small would make dh/dt larger (faster deepening). The term $\gamma_s E$ appears in the numerator of (4-28) and acts to counter the effect of positive heat input at the surface. This also makes dh/dt larger. The term $\gamma_s E$ also appears in Equation (4-31) and similarly counters the effect of positive heat input into

the mixed layer, making a deeper mixed layer depth in the heat-dominated regime. Thus, in the case where evaporation exceeds precipitation and there is a decrease of salinity away from the surface, salt may be thought of as being added to the mixed layer. Salt makes the mixed layer denser, which would tend to aid overturning of the mixed layer. When turbulence redistributes the accumulated salt from the surface uniformly throughout the mixed layer and thus lowers the center of mass of the salt, a source of potential energy is tapped. This source of salt potential energy conversion will add to the wind turbulent energy to make a deeper mixed layer. A deeper mixed layer results in a decreased mixed layer temperature since deepening causes colder water to be entrained into the mixed layer. Thus, the effect of salt in the subtropics is to increase the mixed layer depth and decrease the mixed layer temperature.

4.3 The Importance of Salt on Mixed Layer Dynamics

In the previous section an energy model for the mixed layer was developed with the influence of salt taken into account. With typical data from N we shall now use this model to determine the effect of salt on the mixed layer depth at N. First we will investigate the consequence of salt on the wind regime.

In the equation for deepening of the mixed layer (4-28), the salt is in the term

$$\frac{1}{\rho_0 c_p}\left[\alpha_T F+\alpha_T R(1+e^{-\gamma h})\right]+\alpha_S E$$

Here, $\alpha_T = -2.6 \times 10^{-4}$ $(°C^{-1})$ and $\alpha_S = 7.6 \times 10^{-4}$ $(‰^{-1})$.

Evaluating the term with S = 35.0%, He = +20.0 cal/hr, then

$$\alpha_S E = \frac{HeS}{L} \simeq 1.4 \times 10^{-5}$$

Evaluating the term $\frac{1}{\rho_0 c_p}\left[\alpha_T F+\alpha_T R(1+e^{-\gamma h})\right]$ with

F = -12.5 cal/hr and R = 20.0 cal/hr, then

$$\frac{1}{\rho_0 c_p}\left[\alpha_T F+\alpha_T R(1+e^{-\gamma h})\right] \simeq 1.4 \times 10^{-3}$$

In the case of night, R = 0 and

$$\frac{1}{\rho_0 c_p}\left[\alpha_T F+\alpha_T R(1+e^{-\gamma h})\right] = \alpha_T F \approx 3 \times 10^{-3}$$

Except for a few moments of the day when $F \cong R(1+e^{-h})$

$$\left[\alpha_S E\right]+\frac{1}{\rho_0 c_p}\left[\alpha_T F+\alpha_T R(1+e^{-\gamma h})\right]$$

$$\cong \frac{1}{\rho_0 c_p}\left[\alpha_T F+\alpha_T R(1+e^{-\gamma h})\right]$$

The other term involving salt is

$$\left[\alpha_T(T_s - T_{-h}) + \alpha_S(S_s - S_{-h})\right]$$

For deepening mixed layers

$$T_s - T_{-h} \sim .03\ ^\circ C/\text{meter}$$

$$S_s - S_{-h} \sim .004\ ‰\ /\text{meter}$$

So

$$[\alpha_T(T_s - T_{-h}) + \alpha_S(S_s - S_{-h})] \approx [\alpha_T(T_s - T_{-h})]$$

Thus, the equation shows that in the wind regime the role of salt on the mixed layer dynamics of N is negligible. Actually, the salt gradient in the sub-mixed layers that have been entrained in the mixed layer is orders of magnitude less than the temperature gradients, further reducing the effect of salt.

Next let us consider what salt does to the heat regime (Equation 4-31). The salt effect appears in the term

$$\frac{1}{\rho_0 c_p}[\alpha_T F + \alpha_T R(1+e^{-\gamma h})] + \alpha_S E\ .$$

This is exactly the same term as in the wind regime. It has already been shown in the discussion of the wind regime that the salt effect is insignificant. Therefore, the role of salt on the mixed layer dynamics is also negligible during the heat regime.

In an earlier section we asked the question whether salinity has a significant effect on mixed layer dynamics at N. We have demonstrated that the work of salt on the mixed layer dynamics is of no

consequence. In fact, when the "E" factors are left out of the salt mixed layer model, Equations (4-28) to (4-33) simplify to Equations (4-1) to (4-6); that is, Denman's model. We can say positively now that the model of Denman can be used for data at N without that data being drastically affected by salinity.

5. TESTING OF DENMAN'S MODEL

In the last chapter we demonstrated that it is possible to use the Denman model as is on the data from N. We are now ready to test Denman's model, using information from N, to see whether the model can in fact accurately forecast mixed layer changes. Data from N for the months of December 1970 and May 1969 are utilized to test Denman's model.

5.1 Application to a Case in May 1969

First we shall test Denman's model in the case of a decreasing, then slowly increasing mixed layer at N. We shall select a time sequence from 3 May to 20 May 1969 because data are available for this period and the ship was on station at the time.

Fluxes

To begin, we must compute fluxes since they drive the model. The hourly meteorological observations from N, which were produced as time series, are used to compute the surface fluxes. These time series are for cloud cover, wind speed, air temperature, wet bulb temperature and sea temperature (see Figure 5.1).

Also employed in the computation of fluxes is incoming solar radiation. The incoming solar radiation is calculated from the

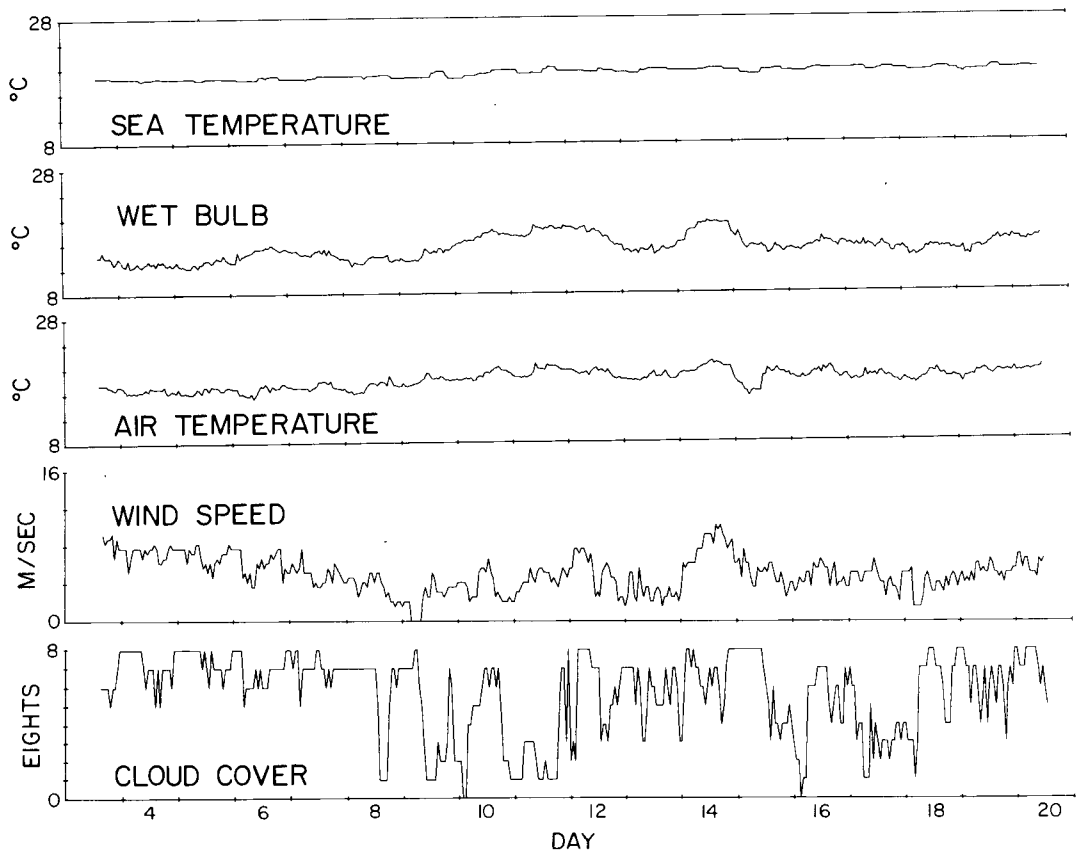

Figure 5.1. Time series of hourly meteorological observations for the period of 3 May to 20 May 1969.

empirical formula used in the descriptive section. The incoming clear sky solar radiation was 742 calories a day.

The computation of the hourly surface fluxes is done with the same formulas as earlier discussed in the descriptive section. The exception is that energy available for turbulent mixing from the wind is determined according to a partition of energy which is

$$E = \rho_0 C_D m u_{10}^3$$

where m is the partition of wind energy available for turbulent mixing. Here $m = 1.2 \times 10^{-3}$ and $C_D = 1.3 \times 10^{-3}$, the values Denman found to best fit Ocean Station P data.

The results of the flux formulas can be seen in the form of time series for wind energy, surface heat flux (sensible, latent, and back radiation) and solar radiation as seen in Figure 5.2.

In the model large scale downwelling due to the curl of the wind stress is set to zero here. This is because of the computations of Wickett and Thomson (1971), who show that the vertical motion at N due to the curl of the wind stress is of the order of a meter per month and therefore negligible.

The initial submixed layer water temperatures in the model decreased linearly with depth. The actual submixed layer temperatures were an average estimated from BT data.

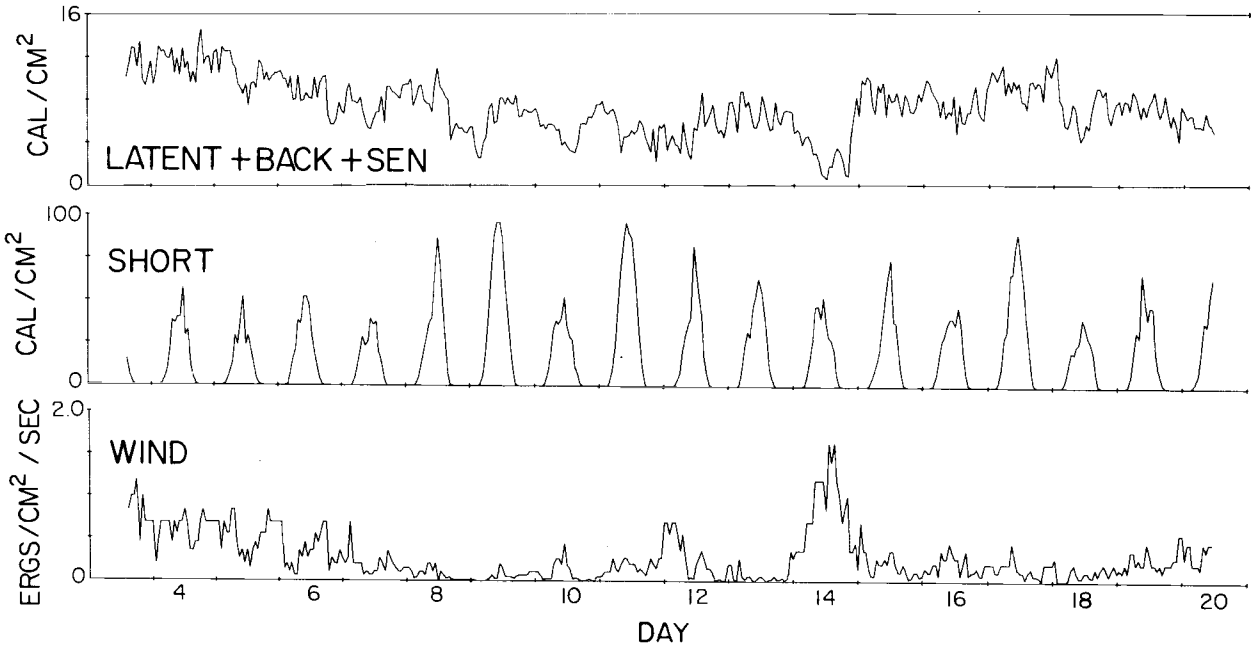

Figure 5.2. Surface fluxes for May 1969 computed from the hourly meteorological observations in Figure 5.1. The upper graph is the heat loss from the surface. The middle graph is the incoming solar radiation. The lowest graph is the wind energy available for turbulent mixing of the mixed layer.

Advection

The next thing we must do is to estimate the effects of advection at N. This is necessary to determine which portions of changes are due to local effects. We are going to consider advection on temperature and mixed layer depth change. It was already pointed out in the descriptive chapter that the advected mixed layer depth change is not significant. Neither is the advected surface temperature. The estimated advected surface temperature change is in the range of -.5°C to +.3°C for 17 days (the length of the model run). Since the total change at N between 3 and 20 May is +2.0°C, we can assume that the major portion of the mixed layer temperature change is due to local effects.

The Synoptic Situation

From the 3rd to the 7th of May 1969, N was under the influence of a high to the northeast. By the 8th and 9th, a weak front was located to the northwest and weak lows to the east of N, resulting in a weak, disorganized pressure and wind field. From the 10th to the 15th, another weak front approached N from the northwest, crossed N on the 15th, and moved slowly to the southeast. From the 18th to the 20th of May, N was again under the influence of a high that established itself to the northeast and moved slowly to the east. In

summary, the May synoptic picture is irregular with periods of weak and varying wind direction.

Variation of the Extinction Length

We shall now turn to examination of the response of the model. It should be recalled that the average extinction length of light is a floating constant in the model. Let us see what the variation of γ^{-1}, the extinction length of solar radiation, does to affect the results of the model when driven by the May data. Shown in Figure 5.3 is the 3 to 20 May case of the maximum mixed layer depth for each day. The curves are for $\gamma^{-1} = 5, 10, 15$ meters. For comparison, the mixed depth as calculated from mechanical BTs is also shown. The best-fitting extinction length appears to be $\gamma^{-1} = 5$ meters, which according to Denman (1972) and Kraus and Rooth (1961) should be typical of much higher latitudes.

The surface temperatures of the model with the variation of γ^{-1} (corresponding to Figure 5.3) are shown in Figure 5.4. In this case, the minimum and the maximum for each day, which occur in the early morning and the afternoon respectively, are shown. Again, the $\gamma^{-1} = 5$ meters appears to be the best fit.

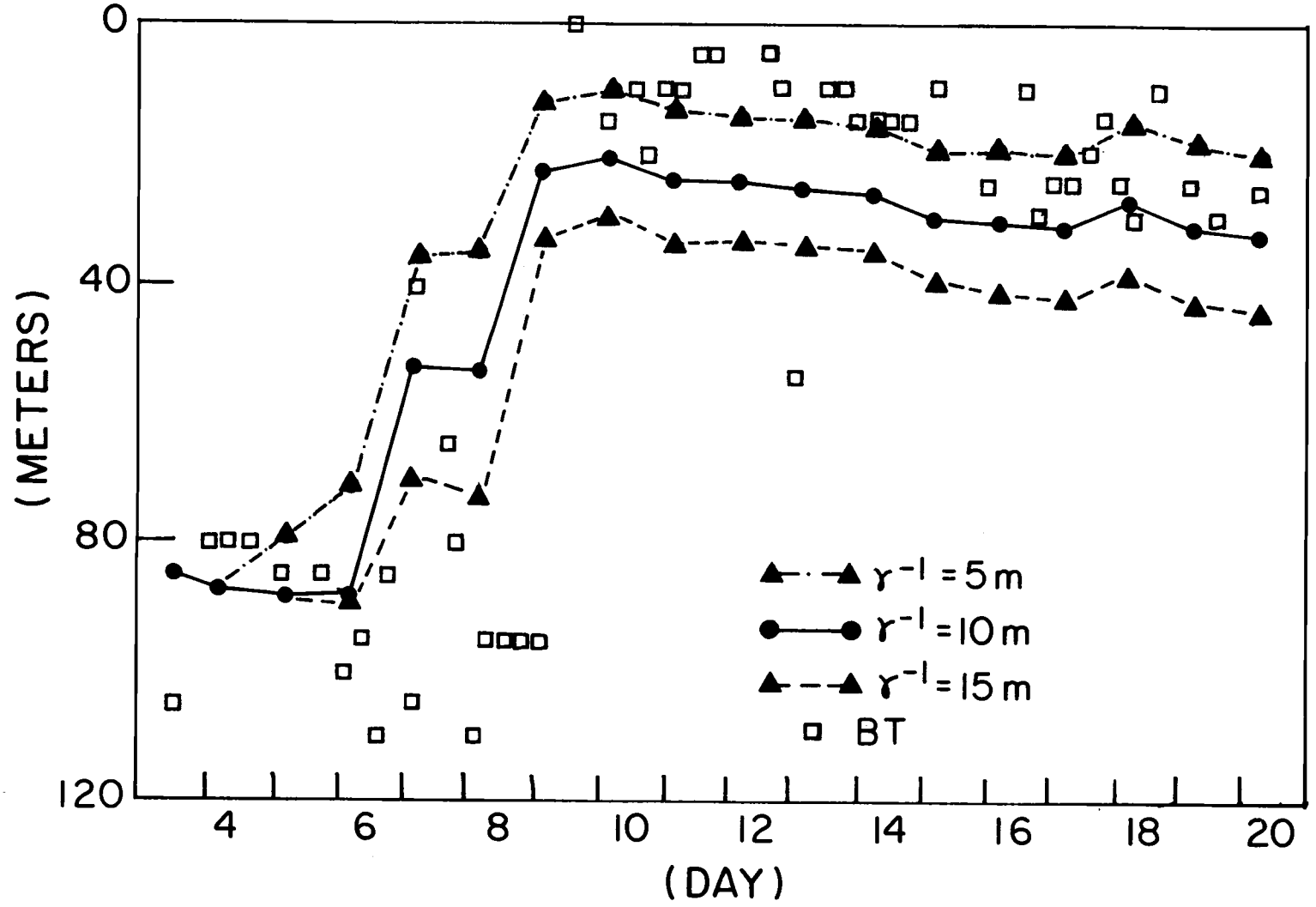

Figure 5.3. Model mixed layer depth with different extinction lengths for May 1969. Only the maximum value for each day is plotted. BT mixed layer depths are shown for comparison.

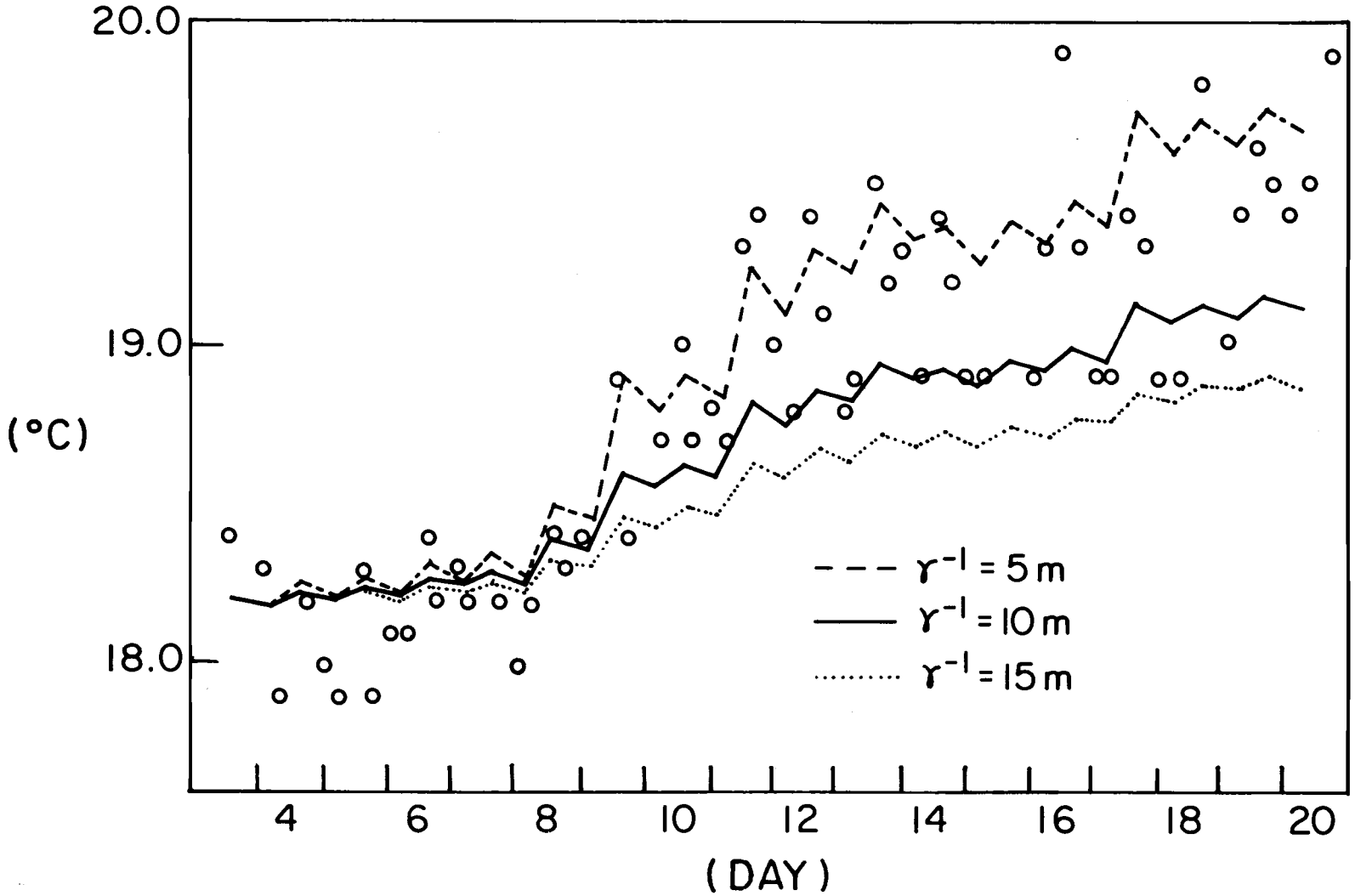

Figure 5.4. Model mixed layer temperature with different extinction lengths for May 1969. The maximum and minimum for each day is shown. BT mixed layer temperatures are shown for comparison.

Limitation of the Mixed Layer Extinction Length

The average vertical-extinction length for sunlight is limited to a narrower range of values than previously believed possible. Denman (1972) examined the effect of the variation of γ^{-1} on the mixed layer depth and selected a value of $\gamma^{-1} = 5$ meters as a best fit of Ocean Station P data. Kraus and Rooth (1961) used a value of $\gamma^{-1} = 20$ meters when modeling a subtropical oceanic case.

Jerlov (1968) shows that the extinction coefficient for a single wavelength decreases from the more opaque water at higher latitudes (such as Ocean Station Vessel P) to that in the subtropics (the least opaque). Here we are not referring to a single wavelength in the model, but the total sunlight spectrum. It is also shown in Jerlov (1968) that the solar radiation spectrum changes drastically as it passes through sea water. The green or central wave bands of the solar spectrum are the most transmitted, while the shorter and longer wavelengths are absorbed very quickly. The result is that after passing a few meters of water, only the green light of the original sunlight is left in significant quantity and so the average extinction length per unit value of water goes up. Thus, since the mixed layer is usually at least 5 meters thick, a relatively small average extinction length should be used (say 5 meters). Below the mixed layer, mostly only green light is left and a much longer absorption length should be

used (such as 15 or 20 meters).

A Double Extinction Length

Suppose that we set up a crude model with two extinction lengths: one for the mixed layer and one for the submixed layer waters. Figure 5.5 shows the mixed layer temperatures for three combinations of $\gamma_u^{-1}/\gamma_\ell^{-1}$. The upper curve is simply

$$\gamma_u^{-1} = 5m/\gamma_\ell^{-1} = 5m \quad \text{for comparison.}$$

The second is $\gamma_u^{-1} = 5m/\gamma_\ell^{-1} = 15m$ and the lower curve is $\gamma_u^{-1} = 5m/\gamma_\ell^{-1} = 20m$. The latter two have an insignificant difference (.03°C) accumulated even after 18 days. The final temperature difference between the first two curves is larger--about .17°C after 18 days. It should be noted in the last example that the differences between the single and multiple extinction lengths are not notable until after 7 days and when the mixed layer has appreciably shallowed.

It is as expected that the longer the submixed layer extinction length, the less the calculated submixed layer temperature change since there is less retention of solar energy below the mixed layer during the daylight hours. When the mixed layer descends at night, it recovers by entrainment some of the solar energy stored in the submixed layers. The longer the submixed layer extinction length,

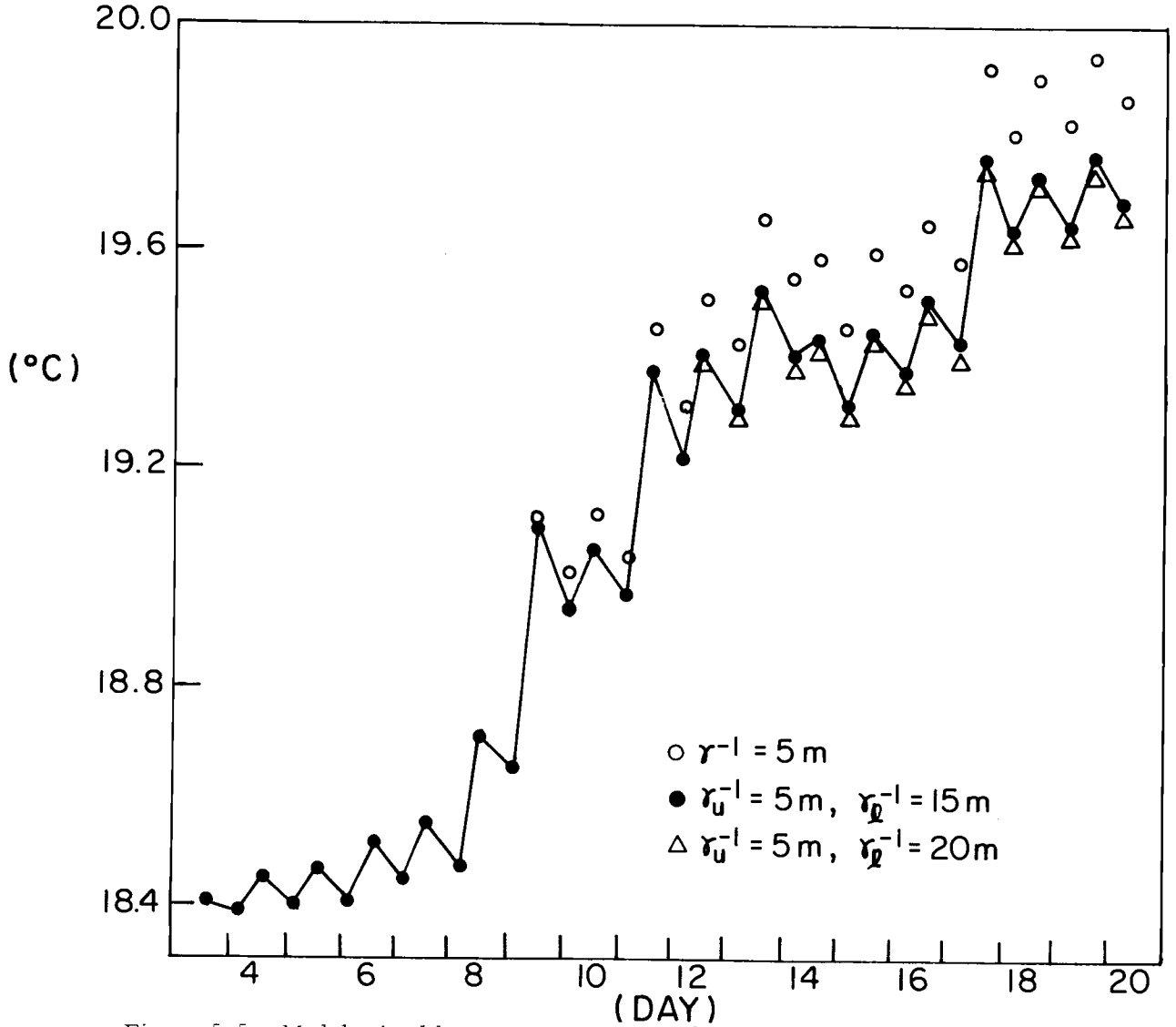

Figure 5.5. Model mixed layer temperature with split extinction lengths for May 1969 data. The maximum and minimum is shown for each day.

the less solar radiation will be stored per meter in the waters just below the mixed layer and can be later recovered by entrainment into the mixed layer.

When the mixed layer is much deeper than $2\gamma^{-1}$, the submixed layer extinction length does not make a great difference to the mixed layer depth. This is because the amount of solar energy that escapes the mixed layer depends on $e^{-\gamma h}$. When the mixed layer is deep, little significant solar radiation leaks out of the bottom of the mixed layer. So, to the total system, the submixed layer extinction length is unimportant when the mixed layer depth is large.

Variation of Fluxes

Besides the extinction length, another major uncertainty is involved in the surface fluxes. These uncertainties in the flux calculations are due to measurement errors as well as to errors of the empirical constants in the flux formulas. The sensitivity of the model results to these deviations of surface fluxes is examined in Figure 5.6. All curves use the extinction lengths of $\gamma_u^{-1} = 5m/\gamma_\ell^{-1} = 15m$. The upper curve, referred to as +20%, is computed by multiplying heat fluxes by .80, the wind energy by .80 and the solar radiation flux by 1.20. The central curve is computed using the standard fluxes. The lower curve, called -20%, is computed by multiplying the heat fluxes by 1.20, the wind energy by 1.20 and the solar radiation by .80.

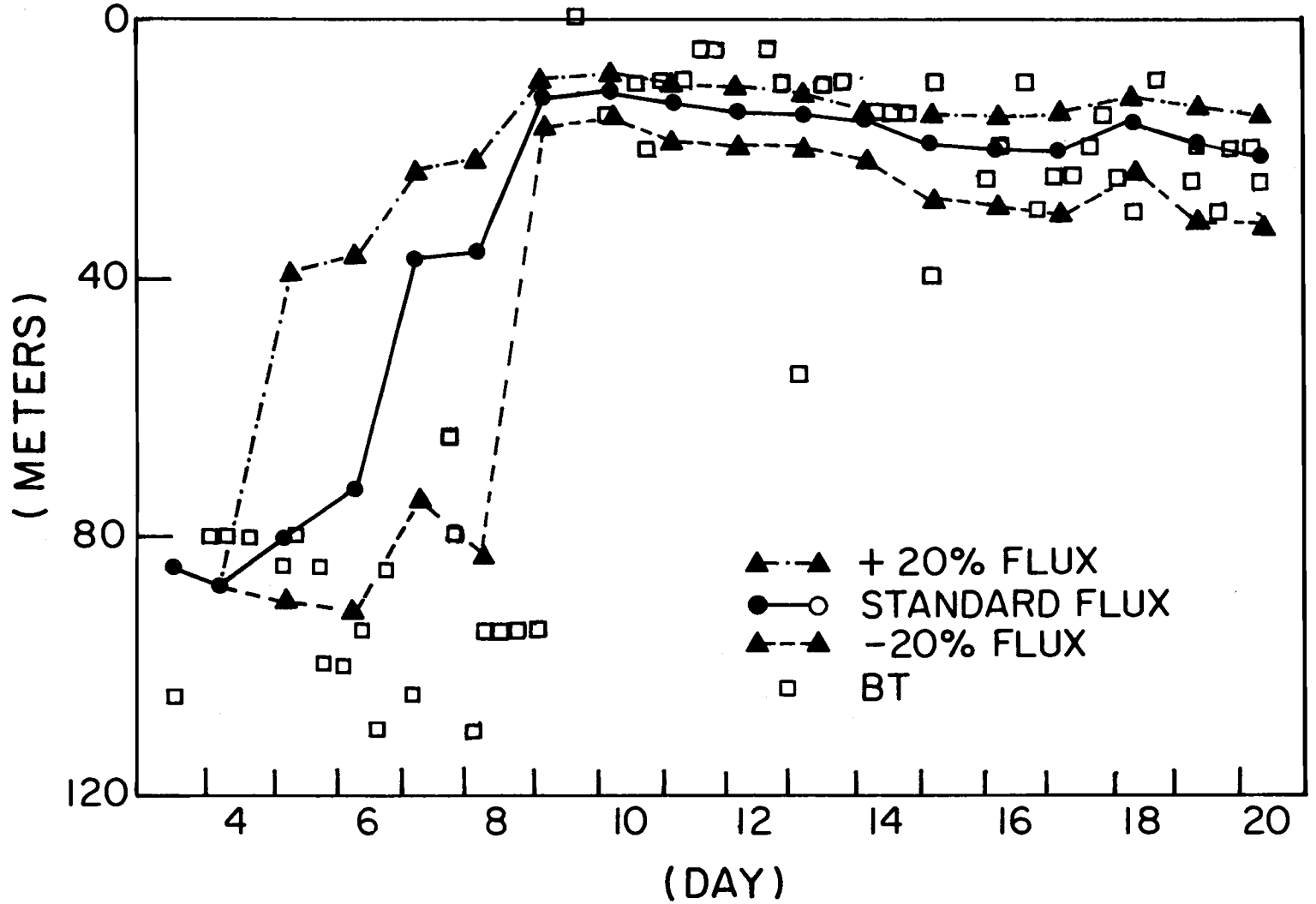

Figure 5.6. Model mixed layer depth with surface flux variation (γ_u^{-1} = 5 m, γ_ℓ^{-1} = 15 m). BT mixed layer depths are shown for comparison.

The result is a curve of the standard fluxes and curves of ±20% of the fluxes so as to decrease or increase the mixed layer depth. These curves give an idea of the range of the effect of flux variation on the model's results.

It is interesting to note how well the features of the mixed layer are reflected by the model. Initially, the model correctly forecasts the maintenance of the same mixed layer depth from the 3rd to the 6th of May as the surface heat loss and wind energy are approximately uniform. As the surface heat loss and wind energy markedly decrease between the 6th and 8th, the model predicts a dramatic decrease in the mixed layer depth which occurs also in the data. After the rapid shallowing of the mixed layer, there is a modest increasing trend in the surface heat loss and the wind energy which causes the model to predict a general slow downward movement of the mixed layer depth from the 10th to the 20th of May. This, too, is reflected by the BT data.

However, the shallowest mixed layer depths, 10m or less, are not as well reflected by the model. This could partly be due to special complexities arising when the mixed layer is less than γ^{-1} and a shorter extinction length would be more realistic. Also, the very shallowest of mixed layers might coincide with the greater horizontal inhomogeneity or "pools" of the surface mixed layer, which would be too much of a violation of basic horizontal homogeneity assumption

in the model.

There is a further conflict between the model's predictions for mixed layer depth between 6 and 8 May and those calculated by BTs. The mixed layer depth is deeper than that given by the model. This could be due to local inhomogeneity in the mixed layer depth or some sort of BT error. The few bottle casts taken during that period indicate that the mixed layer depth is less than 100 meters, as does the model. The data from these casts tends to agree with the model and to disprove the BT calculations.

We will now compare the model's predicted temperatures with the observed temperatures of the mixed layer. The corresponding mixed layer temperatures for the curves of Figure 5.6 are shown in Figure 5.7. Only the maximum and minimum daily temperatures are plotted. We find first that the standard flux curve follows the trend of the surface BTs quite closely. However, if the fluxes are varied by the ±20% fluxes, they deviate from the standard flux curve by more than .3°C after 18 days. This means that only a rather narrow range of variation in the surface fluxes will be tolerated by this model in order for it to reproduce observed conditions of the mixed layer.

The mixed layer depth trends are similar to the temperature trends. Between the 3rd and the 6th, the model mixed layer temperature is about constant as is the surface heat loss and the measured mixed layer depth. When the surface heat loss decreases and the

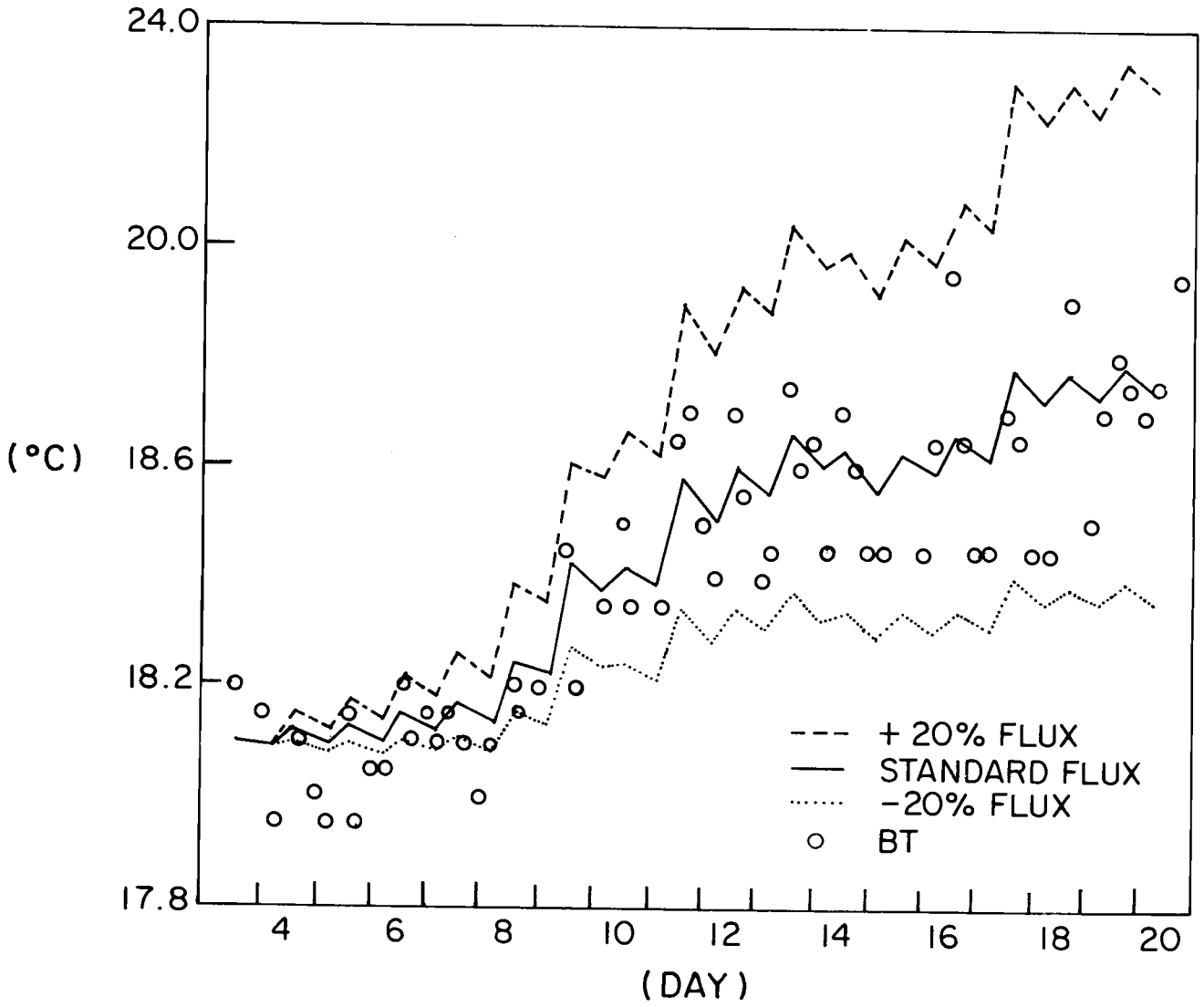

Figure 5.7. Model mixed layer temperature with surface flux variation (correspond to Figure 5.6).

model mixed layer depth dramatically decreases, the model forecasts a jump in the mixed layer temperature, as actually occurred in the BT temperature. From about the 11th on, the net heat gain through the surface is greater than the loss due to the slow entrainment of colder water below, so the model predicts a slow increase in the mixed layer temperature. This is also reflected in the BT data.

Conclusions for the May Case

Denman's mixed layer model was tested on a quickly decreasing, then slowly increasing mixed layer during May 1969. Overall, the model is sensitive to changes in the wind energy and surface heat balance. Except for the shallowest mixed layers, it is found that the model fits the real data reasonably well so long as new assumptions are made about the extinction length. One of the new assumptions is that the extinction length for sunlight in the mixed layer is of the order of 5 meters for any water type in the mixed layer. Another but less significant assumption is that the submixed-layer extinction length is rather long (about 15 meters) as only the green light usually excapes from the mixed layer.

5.2 Application to a Case in December 1970

We are now going to test the case of a descending mixed layer at N. We are choosing a time period from 16 to 31 December 1970

since the ship was on station and data are available.

Fluxes

As in the May case, we must compute the fluxes or driving forces of the model. From the hourly meteorological values, which are shown in Figure 5.8, the hourly fluxes are computed in the same manner as the May case (see Figure 5.9). As in May, the drag coefficient is 1.3×10^{-3} and the wind partition, m, is 1.2×10^{-3}. The incoming clear sky solar radiation is 336 cal/day. The large-scale downwelling is assumed to be zero. The initial submixed-layer temperatures are assumed to decrease linearly with depth and to be estimated from BT data.

Advection

In the descriptive chapter it is shown that the mixed layer depth advection is negligible. However, the mixed layer advected temperature is quite significant for this December case. Estimates of the advected temperature range from -2.1 to -.1°C per 15 days (the time run of the model). It is quite probable that the major portion of the mixed layer temperature change is due to advection since the total temperature change at N in December was 2.4°C for each 15 days. This is in contrast to the May case where the advected temperature is a minor part of the total temperature change.

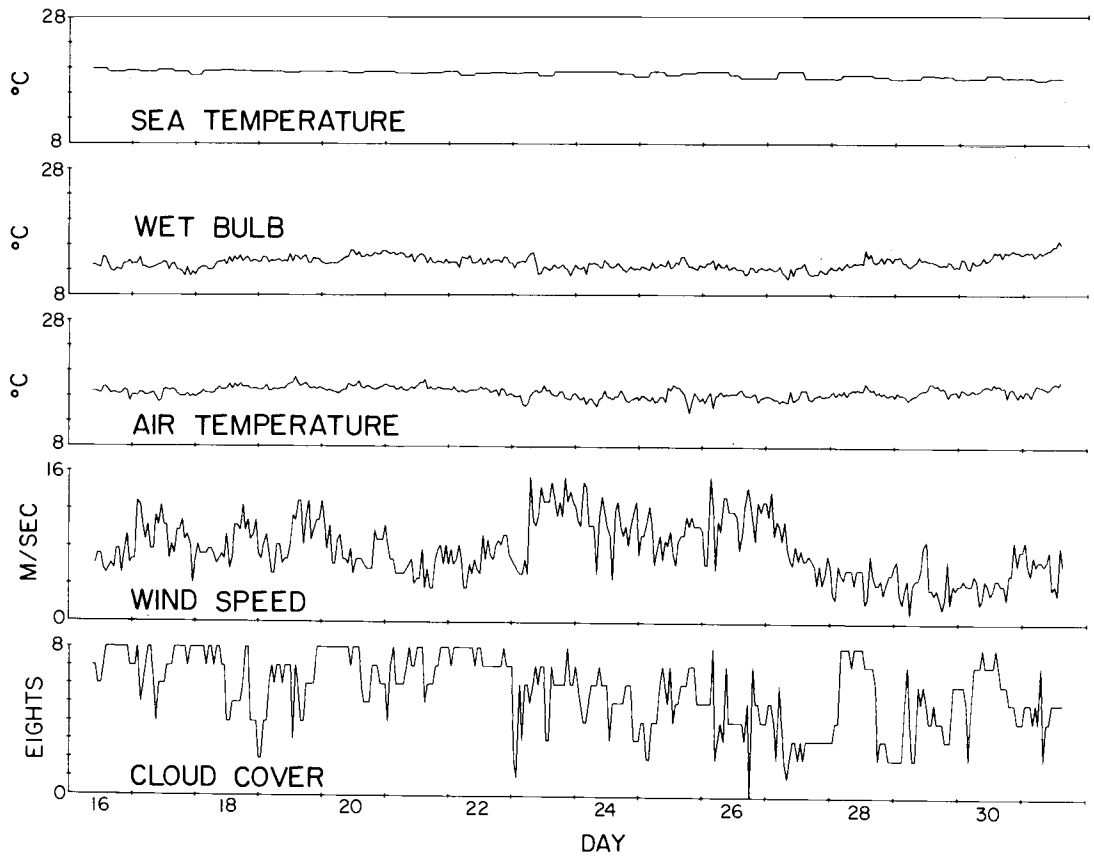

Figure 5.8. Time series of hourly meteorological observations for the period of 16 December to 31 December 1970.

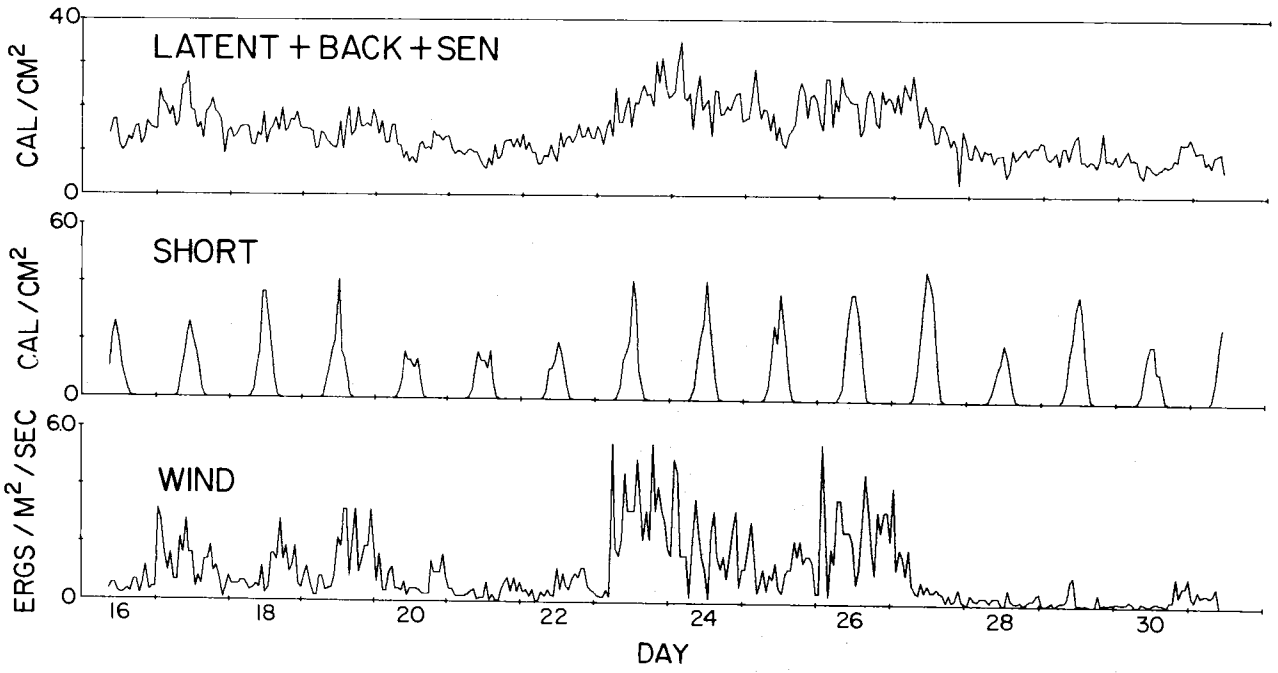

Figure 5.9. Surface fluxes for December 1970 computed from the hourly meteorological observations in Figure 5.8. See Figure 5.2 for explanation.

The Synoptic Situation

Initially, there was a weak front just to the south of N on the 16th of December 1970. From late on the 16th to the 28th, N remained under the influence of a strong high to the Northwest. In addition, from the 24th to the 27th of December, disturbances formed to the East of N which increased the pressure gradient and surface winds of the section of the high that was over N. Between the 29th and 31st, disturbances to the North and East of N weakened the influence of the high that still remained over N. The synoptic picture in December was almost completely dominated by a vigorous high with strong winds from the Northeast. This is in contrast to the disorganized synoptic situation in May 1969.

The Variation of the Extinction Length

We are testing the effect of the variation of the extinction length and the use of the double extinction length on the model using the December data. During this period the daily maximum mixed layer depth was 85 meters or greater. We find that the variations of γ^{-1} do not make a significant difference to the model results. The mixed layer is so deep that the amount of light that penetrates to the bottom of the mixed layer is small so long as any reasonable value is used (less than 15 meters).

Variation of the Fluxes

Shown in Figure 5.10 is the December case with $\gamma^{-1} = 10$ meters, and the ±20% flux variation like that used in the May case. The center graph is a product of the standard fluxes. The mixed layer depth seems to be generally well represented by the model. Due to the large surface heat loss, and high wind speeds, the model has a general increase of the mixed layer from the 16th to the 27th of December which is reflected in the BT data. After the 27th, the wind speed slacks off and the surface heat loss decreases so the standard flux and the -20% flux level off, as does the BT mixed dapth. The +20% flux case ascends after the 27th, which again indicates how close the tolerances are for a change in the surface fluxes. In spite of these agreements, though, the final depth forecasted by the model is 10% too shallow, although this may be statistically insiginficant due to the error of BT measurements.

The trends in the model are similar to those of the BT. Between the 16th and 27th, there is a large heat loss at the surface and a continual entrainment of colder water into the mixed layer. The model shows a mixed layer temperature decrease for the same period as does the BT mixed layer temperature. When there is a decrease in the heat loss and leveling off of the mixed layer depth, as from the 27th to the 31st, the model's temperature levels off for the same

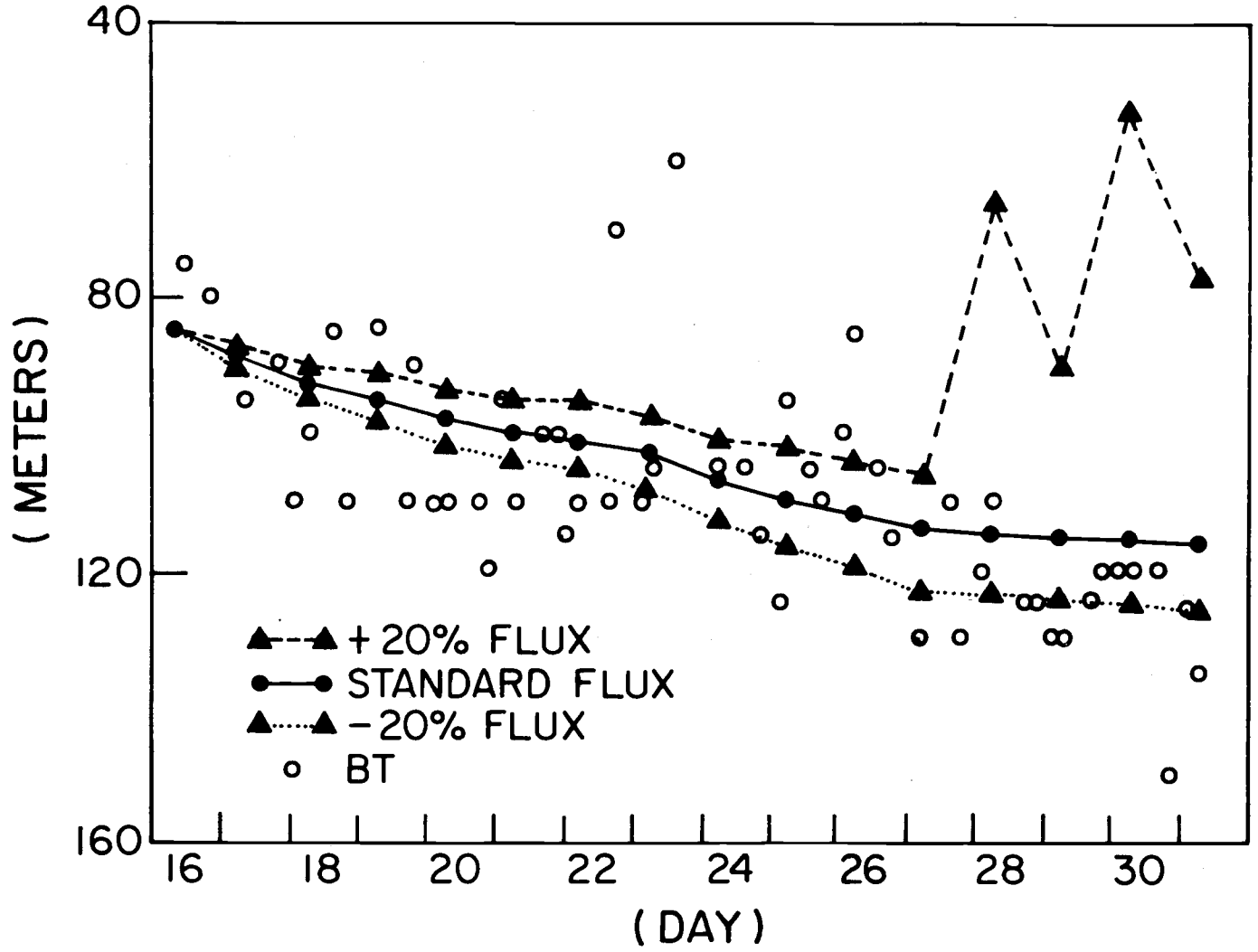

Figure 5.10. Model mixed layer depth with surface flux variation for December 1970 (γ_u^{-1} = 5 m, γ_ℓ^{-1} = 15 m). BT mixed layer depths are shown for comparison.

time, as does the mixed layer actual temperature.

In spite of the agreement of general trends between the model and the BT data, the final temperature of the model is unrealistically small. The final BT mixed layer temperature is a factor of 5 larger than the standard flux curve of the model. It is possible that all of the disagreement between the model and BT temperature is due to advection of temperature. As pointed out in the advection section, the maximum estimated advected temperature for the December case is 2.1°C, or exactly the difference between the model and the BT temperature. Nevertheless, the case can not be adequately resolved until a more precise value for advection can be measured.

Conclusions About the December Case

Denman's model does not completely fit a December 1970 case of an increasing mixed layer depth. The best fit is the mixed layer depth. But the model forecasts a final mixed layer depth that falls short by 10%. Perhaps there was some inertial deepening of the mixed layer which could account for the small discrepancy although it is not very significant. This deepening would also cause a greater local change in the mixed layer temperature because increased deepening causes faster entrainment of colder water which lowers mixed layer temperature.

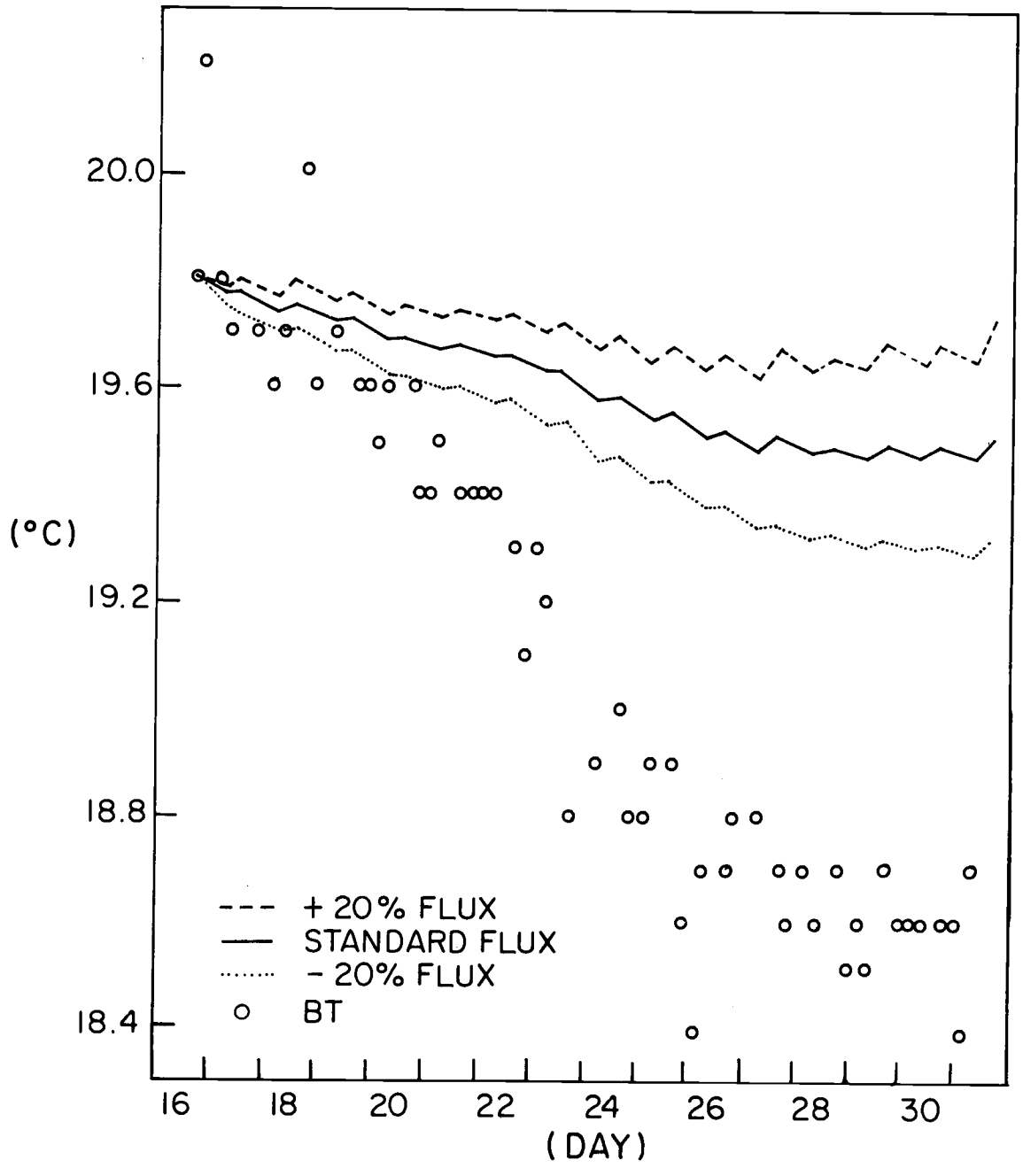

Figure 5.11. Model mixed layer temperature with surface flux variation for December 1970 (corresponds to Figure 5.10).

This may be one reason why the model does not accurately predict mixed layer temperature. The Denman model predicts only a change of the local temperature of -.4 °C/15 days, whereas the actual change was -2.4 °C/15 days. The difference, however, could be made up by the advected temperature change estimates of -2.1 °C/15 days.

Another explanation for the difference between the model and observed data may be that the model is not designed to consider local changes for less than the order of a day. Inertial effects, which are smaller than a day, are left out of the Denman model. But since the December case does include somewhat larger wind stress changes over periods of a few hours, the resulting inertial effects could be important.

There may have been three causes of the mixed layer change at N in December, 1970. The mixed layer temperature change may be a result of (1) advection predominantly; and (2) surface and (3) inertial deepening effects to a lesser degree. The mixed layer depth change could have been caused mostly by surface energetics and some inertial effects. The exact case cannot be resolved here without a reasonable knowledge of the current field of the ocean. Information about this field is not now available.

5.3 Conclusions About the Applied Model

The important conclusion about the Denman model is that it is applicable to forecasting local changes in the mixed layer in the subtropics. In the one case, May, where advective effects could be resolved (because they were relatively minor), the model reasonably predicted the mixed layer depth and temperature changes. In fact, the model was able to successfully anticipate the decreasing and increasing mixed layer depth of the May case.

In the other case, December, where advective effects could not be resolved, we could not determine the successfulness of the model in forecasting mixed depth and temperature changes. For other investigators wishing to apply Denman's model to the subtropics this means that the model can only be used in situations where the advective effects can be determined.

Comparison of the mixed layer at N with the model suggested that the extinction length of the total sunlight spectrum for the mixed layer is only about 5 meters. This is less than that previously believed.

6. CONCLUSION OF THE THESIS

This thesis considers air-sea interaction at Ocean Station Vessel N (30N 140W). As a foundation, the descriptive details of N, which are based upon 20 years of meteorological and 7 years of oceanographic data, are examined. An unexpected result is that the estimated yearly average rainfall is only 23 cm, about half previous estimates. The total cloud cover has only a slight seasonal trend, with the average for the year about 5/8. Low stratiform clouds make up more than 4/8 of the yearly average total cloud cover. The surface salinity has little seasonal variation, indicating that the sea surface density (which has a distinct seasonal trend) is primarily a function of temperature. A surface heat budget balance for the 1951-1960 decade has a distinctly more negative heat budget balance (loss) than the 1961-1970 decade. The difference between the two decades corresponds to a large-scale climatic change in the North Pacific (Namias, 1963). Of the 20-year anomalies for meteorological variables, only the large deviations of pressure appear to correlate with other large scale events in the equatorial Pacific. Diurnal variations of the total cloud cover, wind speed and rainfall estimate are clearly different for each of the four seasons.

Further background material is presented in the form of spectral analysis of the wind, pressure, sea temperature, air temperature and

dew point. All variables have a peak in the spectral density at the annual period. Plots of $f \cdot \phi(f)$ of the wind and pressure have the largest peak at the synoptic periods. Seasonal plots of $f \cdot \phi(f)$ have larger values in the winter than the summer and are peaked in the winter except for the sea temperature. The seasonal sea temperature plot of $f \cdot \phi(f)$ is larger at the diurnal peak in the summer than the winter. The seasonal sea temperature and air temperature $f \cdot \phi(f)$ plots have a dramatic peak at the diurnal period, with the summer larger than the winter. All pressure plots have a sharp peak at the semidiurnal period. An examination of the individual Fourier frequencies (not band averaged) shows that the diurnal spectral densities are larger than the semidiurnal for all variables except pressure, where the opposite is the case.

With these foundations, mixed layer dynamics are investigated. Denman's model of the mixed layer is re-derived with the effect of salinity on density included. It is found that the effect of salinity on mixed layer dynamics in the subtropics is negligible. Therefore, Denman's model, which ignores the salinity role, is theoretically acceptable.

Denman's basic model itself is applied to N data. It is found that Denman's model is appropriate to a subtropical station. It will forecast local mixed layer changes in the subtropics.

This last result should be of interest to modelers and long-range weather forecasters. Large scale models of the atmosphere and ocean need a sensitive model of the mixed layer since the mixed layer is the medium through which properties are exchanged between the atmosphere and the ocean. Denman's model may be used within a large scale model to calculate the local changes in the mixed layer.

The insignificant effect of salinity on local mixed layer dynamics should be of additional concern. It is to be recalled that Pollard et al. (1973) demonstrated that any buoyancy effects, salt included, are unimportant on the inertial scale. It is shown here for N that the effect of salinity on the scale larger than a day is also not important. We also have furthermore pointed out the similarities between N and other Eastern and Central subtropical Pacific stations in the mixed layer discussion. It would seem, then, that the conclusion for N would also be the same for the Eastern and Central subtropical Pacific. In other words, the role of salinity in local mixed layer dynamics in the above-named areas can be ignored. For this reason, smaller-scale modelers and experimentalists do not have to measure the variable of salinity to obtain an estimate of local mixed layer changes in the subtropics.

BIBLIOGRAPHY

Anonymous. 1961. Climatological and Oceanographic Atlas for Mariners. Vol II., North Pacific Ocean, U.S. Navy Hydrographic Office, Washington, D.C.

Ball, F.K. 1960. Control of inversion height by surface heating. Quarterly Journal of the Royal Meteorological Society 86:483-94.

Bathern, K.H. 1972. On the Seasonal Change in the Depth of the Mixed Layer in the North Pacific Ocean. Journal of Geophysical Research 77:7138-7150.

Berlyand, T.G. 1960. Meiodika Klimatologisckeskikh raschetov summarmoi radiatsii (Method of Climatological Calculation of global radiation). Meier. i. Gidrol., 6, 9-12.

Bjerknes, J. 1969. Atmospheric Teleconnections From the Equatorial Pacific. Monthly Weather Review 97:163-172.

Blackman, R.B. and J.W. Tucky. 1958. The Measurement of Power Spectra from the Point of View of Communication Engineering. 190 pp. Dover, New York.

Bryan, Kirk. 1969. Climate and the Ocean Circulation: III. The Ocean Model. Monthly Weather Review 97:806-827.

Budyko, M.I. 1956. The heat balance of the Earth's surface. Gidrometeorologischeshoe Izdatel' stvo, Leningrad (Translated by Office of Technical Services, U.S. Dept. of Commerce, Washington, D.C., 1958, 259 pp).

Busch, N.E., H. Tennekes, and H.A. Panofsky. 1973. Turbulence structure in the planetary boundary layer. Boundary Layer Meteorology 4:211-240.

Byshev, V.I. and Yu. A. Ivanov. 1969. The time spectra of some characteristics of the atmosphere above the ocean. Iz. Atmos. Oceanic Phys. 5:17-28.

Chiu, Wan-Cheng. 1960. The Wind and Temperature Spectra of upper Troposphere and lower Stratosphere over North America. Journal of Meteorology 17:64-77.

Deacon, E.L. 1959. The measurement of turbulent transfer in the lower atmosphere, Advances in Geophysics 6:211-224.

Deacon, E.L. and E.K. Webb. 1962. Interaction of Properties Between Sea and Air, The Sea Vol. I., Editor M.N. Hill, 43-87, New York, Interscience.

Deardorff, James. 1968. Dependence of Air-Sea Transfer Coefficients on Bulk Stability. Journal of Geophysical Research 73:2549-2557.

Denman, K.L. 1972. The Response of the Upper Ocean to Meteorological Forcing. PhD thesis, The University of British Columbia. pp 117.

Ekman, V.W. 1903. On the influence of the earth's rotation on ocean currents. Kongliga Svenska Velenskaps Akademien Arkiv fur Mathematik, Astron ock fysik, 2(11).

Fairbridge, Rhodes W., Joseph L. Reid Jr., Eric Olaussen, and M.N.A. Peterson. 1966. Pacific Ocean, In: The Encyclopedia of Oceanography, Rhodes W. Fairbridge Ed., Reinhold, N.Y., 653-681.

Foster, T.D. 1971. A convective Model for the Diurnal Cycle in the Upper Ocean. Journal of Geophysical Research 76:666-675.

Freeman, J.C. Jr. 1954. Note on a Prediction Equation for the Surface Layer of a Two-Layer Ocean. Transactions, American Geophysical Union 35:585-587.

Gonella, Joseph. 1972. A rotary-component method for analysing meterological and oceanographic vector time series. Deep-Sea Research 19:833-846.

Husby, David M. 1969. Oceanographic Observations North Pacific Ocean Station November 30°00N 140°00W. March 1967-March 1968. U.S. Coast Guard Oceanography Report. No. 26. CG-373-26.

Jacobs, W.C. 1951. The energy exchange between the sea and the atmosphere and some of its consequences. Bull. Scripps. Institute of Oceanography, University of California Vol 6, pp 27-122.

Jerlov, N.G. 1968. Optical Oceanography. London, Elsevier, 199 pp.

Kato, H. and O.M. Phillips. 1965. On the penetration of a turbulent layer into stratified fluid. Journal of Fluid Mechanics 37:643-655.

Kitaigorodsky, S.A. 1961. On possibility of theoretical calculation of vertical temperature profile in upper layer of the Sea. Bull. (izv.), Acad. Sci. U.S.S.R. Geophys. Ser., No. 1-6, 313-318.

Kraus, E.B. 1972. Atmosphere - Ocean Interaction, Oxford. pp. 271.

Kraus, E.B. and J.S. Turner. 1967. A one-dimensional model of the seasonal thermocline. II. The general theory and its consequences. Tellus 19:98-106.

Kraus, E.B. and Claus Rooth. 1961. Temperature and Steady State Vertical Heat Flux in the Ocean Surface Layers. Tellus 13:231-238.

Lee, W.H.K. and C.S. Cox. 1966. Time Variations of Ocean Temperature and its Relation to Internal Waves and Ocean Heat Flow Measurements. Journal of Geophysical Research 71:2101-2111.

Malkus, J.S. 1962. Large-scale interactions, in The Sea Vol 1, 88-294, Interscience, New York.

Manabe, S. 1969. Climate and the Ocean Circulation. Monthly Weather Review 97: Pt I 739-774, Pt II 775-805.

Millard, Jr. P.C. 1971. Wind Measurements from Buoys: A Sampling Scheme. Journal of Geophysical Research 76:5819-5928.

Mooers, C.N.K. 1971. The interaction of an internal tide with the frontal zone of a coastal upwelling region. Appendix III. PhD thesis, Oregon State University.

Munk, W.H. and E.R. Anderson. 1948. Notes on a theory of the thermocline. Journal of Marine Research 7:276-295.

Namias, Jerome. 1959. Recent Seasonal Interaction Between North Pacific Waters and the Overlying Atmospheric Circulation. Journal of Geophysical Research 64:631-646.

_____. 1963. Large Scale Air-Sea Interactions over the North Pacific from Summer 1962 through the Subsequent Winter. Journal of Geophysical Research 68:6171-6886.

_____. 1969. Seasonal Interactions Between the North Pacific Ocean and the Atmosphere During the 1960's. Monthly Weather Review 97:173-192.

Niiler, Pearn P. 1973. Deepening of the Wind-Mixed Layer, Unpublished Manuscript.

Pandolfo, J. P. 1969. Motions with inertial and diurnal periods in a numerical model of the navifacial boundary layer. Journal of Marine Research 27:301-317.

_____. Numerical experiments with alternative boundary layer formulations using BOMEX data. Boundary Layer Meteorology 1:277-289.

_____ and Clifford A. Jacobs. 1973. Numerical Model Studies of Air-Sea Interactions Utilizing Data from Project Bomes. BOMEX Bulletin No. 11.

Pillsbury, D., J. Bottero, Bob Still, and W. E. Gilbert. 1974. A Compilation of Observations from Moored Current Meters: Oregon Coast May-Oct 1972. Unnumbered CUEA Data Report, Oregon State University. In Press.

Pollard, Raymond T., Peter B. Rhines, and Rory O. R. Y. Thompson. 1973. The Deeping of the Wind-Mixed Layer, Geophysical Fluid Dynamics 3:381-404.

Quinn, William H. and Wayne V. Burt. 1970. Predictions of Abnormally Heavy Precipitation over the Equatorial Pacific Dry Zone. Journal of Applied Meteorology 9:20-28.

_____. 1972. Use of the Southern Oscilliation in Weather Prediction. Journal of Applied Meteorology 11:616-628.

Reed, R.K. and William P. Elliott. 1973. Precipitation at Ocean Weather Stations in the North Pacific. Journal of Geophysical Research 78:7087-7091.

Roll, H.U. 1965. Physics of the Marine Atmopshere, Academic Press, New York, pp. 426.

Roden, Gunnar I. 1963. On Sea Level, Temperature, and Salinity Variations in the Central Tropical Pacific and on Pacific Ocean Islands, Journal of Geophysical Research 68:455-472.

Sverdrup, H.V., M.W. Johnson, and R.H. Flemming. 1942. The Oceans Their Chemistry, Physics, and General Biology, Prentice-Hall, New York, pp. 1087.

Tucker, G.B. 1961. Precipitation over the North Atlantic Ocean, Quarterly Journal of Royal Meteorological Society 87:147-158.

Tully, J.P. 1965. Oceanographic regions and processes in the seasonal zone of the North Pacific Ocean. Studies on Oceanography, Edited by Kozo Yoshida, University of Washington.

Tully, J.P. and L.F. Giovando. 1963. Seasonal temperature structure in the eastern subarctic Pacific Ocean. The Royal Society of Canada Special Publication No. 5. (Ed M. J. Dunbar) pp. 10-36.

Turner, J.S. and Kraus, E.B. 1967. A one-dimensional model of the seasonal thermocline. I. A laboratory experiment and its interpretation. Tellus 19:88-97.

Wagner, James A. 1971. Long-Period Variations in Seasonal Pressure over the Northern Hemisphere, Monthly Weather Review 99:49-66.

Wickett, W.P. and J.A. Thomson. 1971. Transport Computations for the North Pacific Ocean. Fisheries Research Board of Canada, Technical Report No. 238.

Wyrtki, Klaus. 1965. The Average Annual Heat Balance of the North Pacific Ocean and its Relation to Ocean Circulation. Journal of Geophysical Research. 70:4547-4559.